

Advanced Plasmonic Nanostructures for Engineering Fluorescence Applications

THÈSE N° 7772 (2017)

PRÉSENTÉE LE 11 MAI 2017

À LA FACULTÉ DES SCIENCES ET TECHNIQUES DE L'INGÉNIEUR
LABORATOIRE DE NANOPHOTONIQUE ET MÉTROLOGIE
PROGRAMME DOCTORAL EN PHOTONIQUE

ÉCOLE POLYTECHNIQUE FÉDÉRALE DE LAUSANNE

POUR L'OBTENTION DU GRADE DE DOCTEUR ÈS SCIENCES

PAR

Xiaolong WANG

acceptée sur proposition du jury:

Prof. J.-E. Moser, président du jury
Prof. O. Martin, directeur de thèse
Prof. G. Colas-des-Francis, rapporteur
Prof. S. Blair, rapporteur
Dr Z. Benes, rapporteur



ÉCOLE POLYTECHNIQUE
FÉDÉRALE DE LAUSANNE

Suisse
2017

Remember where you started
and you will make your journey complete.
— Avatamsaka Sutra

To Mengru and my family...

Acknowledgements

This thesis would not have been possible without so much help from many people. Over the last four years, I have been learning from so many people and now I would like to take the opportunity to appreciate all of you. First I would like to thank Olivier who gave me such precious opportunity to work for my Ph.D. in NAM. Over the past four years, Olivier always supported my research and gave me all the freedom for what I would like to do in my experiments.

I would also like to give my great thanks to the NAM team. To the previous members, Arash, Krishnan, Andrea, Thomas, Banafsheh, Shourya, Mohsen, Volodymyr, and Robert for giving me support from the most basic wafer ordering in a cleanroom to where to buy Chinese food. To Christian for teaching me the focused ion beam, collaborating on the silver project, offering numerous ideas for my fabrication and experiments, and correcting my badly written manuscripts. To Chen and Raziman for always giving a hand on the numerical simulation aspect no matter how basic is my question. To Weihua, Chen, Kuangyu, Hao, Luc, Madasamy, Valentine for giving me the opportunity to do collaboration in the sense of practicing my fabrication skills and different research, such as metasurface, nonlinear optics, electro-photochemistry. To Beatrice, Cathy and David for the help of administration and IT services. To the current new group members, Toralf, Jeremy, Gabriel, Michail, Debdatta, Giorgio, Sebastian, Alessandro and Daniel for sharing your research and culture.

The colleagues from CMI, Zdenek for training me on e-beam, SEM and the discussions of the problems I had during the fabrication. To Joffrey for training the focused ion beam, ion beam etching and wet etchings. To Guy, Philip, Partrick for LAB600 support. To Didier for the support with AFM measurement and giving the silicon tips for free. To Giancarlo and Yvan for the help with dicing machine. To Remy and Cyrille for the help with etching machines. To Georges and Julien for the photolithography training and answering all the basic questions. To Pierre for the x-ray photoelectron measurements. To all the guys, Manhesha, Valentin, Michele, Ioulia, Zuhail, Ryan, Liu, Junqiu I met in the CMI during the machine waiting time.

To the jury members, Prof. Steve Blair, Prof. Gérard Colas-des-Francis, Dr. Zdenek Benes and Prof. Jacques-Edouard Moser for taking the time to study my thesis.

Big thanks to the friends I have met over the last four years in EPFL. To Kuangyu, Chen, Jianlin,

Acknowledgements

Jian, Eric, Thomas, Yixing and those guys from all over the world whose names I cannot remember, for the fun time on the playground during the basketball game. I really appreciate Catherine for offering me a room to stay with all kindnesses making me as comfortable as if I stayed at home. To Delphine for so much patience and encouraging me to finally pass the Swiss driver license test. To Nadia for supporting me to finish the contract with the insurance company which was a big headache for me and explaining me the culture difference between Switzerland and China.

Finally, to my girlfriend Mengru for allowing me to stay in the lab rather than with her so often during the weekend. To my family for their kindness and tolerance to let me do whatever I want to do.

Lausanne, March 6th, 2017

Xiaolong

Abstract

The appeal of plasmonics lies in the unique properties of coinage metal nanoparticles to strongly confine and enhance electromagnetic fields at the subwavelength. A simple 50 nm colloidal plasmonic particle can not only break the classical diffraction limit and produce subwavelength imaging, but it can also absorb light for killing cancer cells. A dipole gap antenna or a nanohole in a thin film can concentrate light below 10 nm, thus opening many perspectives, such as highly enhanced non-linear optics, extremely sensitive biosensors, Raman spectroscopy and single molecule detection.

This thesis is oriented toward the design of new types of positive and negative plasmonic nanostructures can produce homogeneous plasmonic hot spots, where the electromagnetic field is dramatically enhanced.

Electron beam lithography and focused ion beam milling are the two methods used in this thesis to fabricate antennas. I have developed different original procedures to satisfy the specific fabrication requirements for different geometries. For instance, a dose adjustment technique is developed to achieve the effectively designed antenna gap and linewidth. Alignment accuracy is improved by adding one level of markers, which helps reaching the resolution limit of the system. The difficult liftoff problem caused by proximity effect is overcome by using single point exposure. Ion beam etching technique is applied to obtain perfectly symmetric three-dimensional sandwich structures. Small gaps for the negative antennas are obtained by adding a mask layer on top of soft metals.

Most plasmonic nanostructures reported in the literature use gold as metal, although silver is less absorbing and would provide even stronger enhancement factors. Unfortunately, silver deteriorates extremely rapidly. This has motivated me to investigate the deterioration mechanisms of silver. The common wisdom that oxidation and sulfidation cause the fast deterioration of silver antennas is proved questionable. On the contrary, I found that water or high relative humidity plays a crucial role for the deterioration of silver nanostructures. We have developed a dehydration process to remove the physically adsorbed water on the surface of the nanostructures; the silver antennas treated this way were found to be morphological stable with unaltered optical properties for over 14 weeks. The surface roughness of silver films treated in the same way were also significantly improved.

Abstract

These stable silver films and nanostructures were used to fabricate different types of plasmonic antennas, including negative metallic nanohole antennas and sandwich cavity antenna, to study experimentally the interaction between fluorescent molecules and plasmonics nanostructures. The negative antennas exhibit a thickness-dependent fluorescence enhancement because the near-field enhancement becomes larger as the thickness of the antenna increases; the emission directionality is also improved for thick structures. Using surface chemical functionalization, molecules have also been placed directly in the middle of the sandwich cavity, where the near-field enhancement is strongest. Unfortunately, the measured fluorescence enhancement is rather low; possibly caused by the non-uniform near-field enhancement in cavity and the quenching caused by the metal proximity.

The last part of the thesis is dedicated to exploiting plasmonic hot spots with Fano-resonant plasmonic nanostructures. The proposed 4-nanorod silver antennas produce a nearly homogeneous plasmonic hot spot at the Fano resonance, where most of the energy is confined in the near-field. Using a two-step electron beam lithography method combined with selective surface chemical functionalization, it is possible to place the dye molecules right on the plasmonic hot spot, over a $30 \times 30 \text{ nm}^2$ area. Furthermore, this Fano-resonant structure is highly tunable and can be used to investigate different energetic configurations, where the Fano resonances is tuned to the molecule absorption band or to its emission band, or away from both of them. The fluorescence enhancement is strongest when the Fano resonance is tuned to the absorption peak of the molecule as confirmed by numerical calculations which indicate the highest near-field enhancement. The radiative enhancement dominates the overall fluorescence enhancement when the Fano resonance is tuned to the emission peak of the molecule, which leads to a higher quantum yield enhancement and to a faster decay time. The different experiments reported in this thesis are always supported with advanced numerical simulations.

Keywords: Plasmonics, optical nanoantenna, negative antenna, metallic nanohole, sandwich cavity antenna, electron beam lithography, focused ion beam, ion beam etching, deterioration, chemical and thermal stability, root mean square, surface roughness, humidity, ion migration, oxidation, sulfidation, dehydration, hot spot, near-field enhancement, Fano resonance, extraordinary transmission, directionality, dye molecule, fluorescence enhancement, lifetime, surface chemical functionalization

Zusammenfassung

Dank der einzigartigen Eigenschaft, elektromagnetische Felder in subwellenlängen Dimensionen erheblich zu verstärken, wurde der Plasmonik in den letzten Jahrzehnten grosse Aufmerksamkeit zu Teil. Mit ihrer Hilfe werden zahlreiche neue Möglichkeiten, auch im Bereich Licht-Materie Wechselwirkungen, eröffnet. Die Beugung des Lichts an einem Metallteilchen mit einer Grösse im Bereich von 100 nm durchbricht die klassische Beugungsgrenze und kann nicht mehr mit Abbes Gesetz beschrieben werden. Hinzu kommt, dass solche Teilchen auch Licht absorbieren, sich dadurch erhitzen und potenziell auch in Krebstherapien verwendet werden können. Zum Beispiel mit einer zweiarmigen Dipolantenne oder einem Nanoloch kann das elektromagnetische Feld in einem Bereich von unter 10 nm begrenzt werden. Solche räumliche Beschränkungen zusammen mit der grossen Verstärkung eröffnen viele neue Perspektiven in Bereichen wie nichtlinearer Optik, extrem empfindlicher Biosensoren, Ramanspektroskopie, Detektion einzelner Moleküle usw. In dieser Arbeit beschreibe ich die Entwicklung neuartiger, positiver und negativer Antennen, mit denen homogene plasmonische, so genannte, Hotspots erzeugt werden können. Die vorgeschlagenen Strukturen habe ich mit modernsten Maschinen und Technologien hergestellt, charakterisiert und zum Studium der Molekularplasmonik verwendet. Zur Herstellung habe ich unter anderem Technologien wie Elektronenstrahl Lithographie (EBL) und fokussierter Ionenstrahl Sputtering (FIB) eingesetzt und originelle Verfahren, um die spezifischen Anforderungen an die Strukturen zu erfüllen, entwickelt. So habe ich die Strahlenexposition der EBL optimiert, um die gewünschten Antennengössen und Spaltbreiten zu erreichen. Die Ausrichtungsgenauigkeit konnte durch Hinzufügen einer weiteren Ebene von Markern in Strukturnähe erheblich, beinahe bis zur Grenze der Auflösung des Systems, verbessert werden. Auch die Proximity-Effekte wurden durch die Exposition nur einzelner Pixels dramatisch verringert. Perfekt symmetrische Sandwich-Strukturen habe ich mit einem Ionen-Sputtering Prozess hergestellt. Mittels einer zusätzlichen Schicht, die nach dem Sputtering Prozess wieder entfernt wird, habe ich die Schärfe der Strukturen markant verbessert. Dadurch können vor allem bei weichen Materialien, wie z. B. Gold und Silber, die Abstände zwischen zwei Lochstrukturen erheblich verschmälert und viel kleinere negative Antennen hergestellt werden.

Gegenüber von Gold weist Silber viel geringere Verluste aus, was mich dazu motiviert hat, Silber als plasmonisches Material einzusetzen, seine Langzeitstabilität zu untersuchen und zu verbessern. Wie allgemein angenommen wird, sind Oxidation und Sulfidierung nicht die Hauptmechanismen, die zu einem Verschleiss der Nanostrukturen führen. Vielmehr spielt

adsorbiertes Wasser bei hoher Luftfeuchtigkeit eine zentrale Rolle im Zerfallsprozess. Deshalb habe ich einen Trocknungsprozess entwickelt, um adsorbiertes Wasser von der Oberfläche zu entfernen. Eine Verringerung des Wassers führt zu einer Umstrukturierung der Silberoberfläche wodurch die Stabilität der Strukturen massiv, von einigen Tagen bis zu einigen Monaten, erhöht und die Oberflächenrauigkeit des Films erheblich verringert wird. Der Dehydrierungsprozess führt zu einer Kristallisierung wodurch der Film in einen stabileren polykristallinen Zustand übergeht. So habe ich zweiarmsige, negative und Sandwich Antennen nach der Fabrikation mit dem Dehydrationsverfahren stabilisiert, um die Dynamik von Farbstoffmolekülen in plasmonischen Nahfeld damit zu untersuchen. Die lateralen Dimensionen des plasmonischen Nahfelds dieser Strukturen sind ungefähr $100 \times 100 \text{ nm}^2$. Die Fluoreszenz hängt bei negativen Antennen von der Filmdicke ab, da das Nahfeld mit der Dicke des Films zunimmt. Zusätzlich wird die Richtung der Abstrahlung rechtwinklig zum Substrat begünstigt. Bei negativen Antennen können die Farbstoffmoleküle direkt auf den Film aufgetragen werden, da die Moleküle in nächster Nähe des Films nicht fluoreszieren können. Bei zweiarmsigen und Sandwich Antennen müssen die Moleküle mittels Oberflächenfunktionalisation im Hotspot, wo das Nahfeld am stärksten ist, fixiert werden. Die Verstärkung der Fluoreszenz ist bei diesem Antennentyp geringer. Gründe für die kleinere Verstärkung sind das inhomogene Nahfeld und quenching der Fluoreszenz.

Den letzten Teil dieser Arbeit widmete ich der Optimierung des Hotspots, d.h. der Homogenisierung des Nahfeldes. Zu diesem Zweck habe ich eine Struktur, die eine Fano-Resonanz aufweist, ausgewählt. Wird die Struktur in der Fano-Resonanz angeregt, befindet sich der Grossteil der Anregungsenergie im Nahfeld. Mit den Strukturen, hergestellt mit einer zweistufigen EBL und passender Funktionalisation der Oberfläche, konnte ich die Moleküle direkt in den Hotspot mit einer lateralen Ausdehnung von $30 \times 30 \text{ nm}^2$ platzieren. Die leicht durchstimmbare Fano-Resonanz kann wahlweise so positioniert werden, dass eine Überlappung mit dem Absorptions- oder Emissionsmaximum des Moleküls oder mit keinem der beiden entsteht. Messungen bestätigten, dass die Fluoreszenzverstärkung am grössten ist, wenn die Resonanz mit dem Absorptionsmaximum überlappt. Numerische Berechnungen zeigten, dass in dieser Konstellation das grösste Nahfeld auftritt. Die Strahlungsverstärkung dominiert die totale Fluoreszenzverstärkung, wenn die Resonanz mit dem Emissionsmaximum übereinstimmt ist, was sich in einem schnelleren Zerfall und einer höherern Quantenausbeute zeigt.

Stichwörter: Plasmonics, optische Nanoantennen, negative Antennen, metallische Nanolöcher, Sandwich Antennen, Hohlraum-Antennen, Elektronenstrahl Lithography, fokussierter Ionenstrahl, Ionen-Sputtering, chemische und thermische Stabilität, quadratischer Mittelwert, Oberflächenrauigkeit, Feuchtigkeit, Ionenwanderung, Oxidation, Sulfidierung, Dehydratation, Hotspot, Nahfeldverstärkung, Fano-Resonanz, aussergewöhnliche Transmission, Direktionalität, Dyemolekül, Direktionalität, Fluoreszenzverstärkung, Zerfallszeit, chemische Funktionalisierung

Résumé

La plasmonique a attiré une forte attention en raison de la possibilité de générer et contrôler un champ électromagnétique élevé à une échelle inférieure à la longueur d'onde, jusqu' à une échelle atomique résultant en une forte interaction lumière-matière. Une simple nanoparticule métallique colloïdale (de taille ~ 100 nm) peut non seulement briser la limite de diffraction, permettant une imagerie sub-longueur d'onde, mais peut aussi absorber la lumière et ainsi chauffer pour tuer les cellules cancéreuses. Les nanoantennes dipolaires et les nanotrous dans les films métalliques peuvent concentrer la lumière en dessous de 10 nm, ouvrant de nombreuses perspectives nouvelles, telles que la plasmonique nonlinéaire, la fabrication de biocapteurs extrêmement sensibles, la spectroscopie Raman exaltée de surface, la détection de molécules uniques, etc. Cette thèse est orientée vers la conception de nouveaux types de nanoantennes positives et négatives (trous) qui pourrait créer des points chauds plasmoniques homogènes, fabriquer les antennes proposées avec des méthodes à la pointe de la nanofabrication, les caractériser, et les utiliser pour l'étude de la plasmonique moléculaires. La lithographie par faisceau d'électrons et le fraisage par faisceau d'ions focalisés sont les deux méthodes utilisées dans cette thèse pour fabriquer les nanoantennes. Différentes procédures originales ont été mises au point pour répondre aux exigences spécifiques de la fabrication des différentes nanoantennes. Une technique d'ajustement de dose a été développée pour obtenir les nanogaps et les réponses spectrales désirés. La précision de l'alignement a été améliorée en ajoutant un niveau de marqueurs supplémentaires, ce qui contribue à atteindre la limite de précision possible en nanofabrication. Le problème du décollement de la résine rendu difficile par l'effet de proximité est surmonté en utilisant un point unique d'exposition. La technique de gravure par faisceau d'ions est aussi utilisée pour obtenir des nanostructures de type sandwich parfaitement symétriques. Finalement, les petits gaps entre nano-trous sont obtenus en ajoutant une couche additionnelle de résine au-dessus de la couche métallique.

Les faibles pertes intrinsèques dans l'argent en font un matériau plasmonique de premier choix, par rapport à l'or ce qui m'a motivé à étudier les mécanismes de détérioration des nanostructures d'argent. La conclusion communément admise, que l'oxydation et la sulfuration causent une détérioration rapide des nanoantennes d'argent, est montrée être discutable. Au contraire, j'ai découvert que l'eau ou qu'une humidité relative élevée jouent un rôle crucial dans la détérioration des nanoantennes d'argent. Un processus de déshydratation a développé pour éliminer l'eau physiquement adsorbée à la surface des nanoantennes, grâce auquel les nanostructures sont stables, à la fois du point de vue de leurs morphologies et de leurs ré-

ponses optiques, pour des périodes allant jusqu'à 14 semaines. La rugosité de la surface du film d'argent est réduite lorsque le processus de déshydratation est appliqué car la déshydratation change l'état de l'argent, qui devient poly-cristallin (et non plus amorphe). L'argent, optimisé de la sorte pour fabriquer des antennes stables, a été ensuite utilisé pour fabriquer de deux types de nanoantennes, une antenne composée de nanotrous dans un film d'argent et une nanoantenne sandwich pour étudier expérimentalement la dynamique de l'interaction plasmon-molécule dans une zone de $100 \times 100 \text{ nm}^2$. Pour l'antenne composée de trous, l'augmentation de la fluorescence dépend de l'épaisseur du film, parce que l'exaltation du champ proche devient plus élevée lorsque l'épaisseur de l'antenne est augmentée. De plus, la directionnalité est améliorée et l'émission est ainsi plus centrée vers l'avant. Grâce à la fonctionnalisation chimique de la surface des nanostructures, les molécules sont placées directement au milieu d'une cavité sandwich où le champ proche est exalté. Cependant, l'amélioration de la fluorescence n'est pas si élevée. L'exaltation du champ non-uniforme au sein de la cavité et le « quenching » sont deux raisons possibles pouvant expliquer la faible augmentation de la fluorescence.

La dernière partie de cette thèse est consacrée à l'exploitation complète des hot spots avec une méthode de fabrication adaptée de type top-down et des résonances Fano spécialement adaptées. Une nanantenne composée de quatre nano-bâtonnets d'argent est proposée pour produire un point chaud pratiquement homogène à la résonance de Fano, pour laquelle une majeure partie de l'énergie est confinée en champ proche. L'utilisation d'un faisceau d'électrons et d'une lithographie à deux étapes, en combinaison avec une fonctionnalisation chimique sélective de la surface, les molécules sont placées exactement au point de $30 \times 30 \text{ nm}^2$ où le champ est exalté. Avec une résonance Fano facilement accordable, on peut de préférence la placer à la longueur d'onde d'absorption, ou d'émission de la molécule ou encore loin des deux. L'amélioration de la fluorescence est plus élevée lorsque la résonance de Fano est située sur le pic d'absorption de la molécule, comme confirmé par les calculs numériques qui montrent que l'amélioration est la plus élevée pour forte exaltation. L'exaltation de l'aspect radiatif de la fluorescence domine l'exaltation totale lorsque la résonance de Fano est accordée au pic d'émission de la molécule, ce qui est prouvé par un plus haut rendement quantique et une désexcitation plus rapide.

Mots-clefs : Plasmonique, optique nanoantenne, antenne négative, nanohole métallique, sandwich Cavité, lithographie par faisceau d'électrons, faisceau ionique focalisé, gravure par faisceau d'ions, détérioration, La stabilité chimique et thermique, le carré moyen, la rugosité de surface, l'humidité, la migration ionique, Oxydation, sulfuration, déshydratation, point chaud, amélioration de champ proche, résonance de Fano, Transmission, directionnalité, dyémolécule, amélioration et durée de vie de la fluorescence, Fonctionnalisation chimique de surface

Contents

Acknowledgements	i
Abstract (English/Français/Deutsch)	iv
List of figures	xi
List of tables	xiv
1 Introduction and thesis outline	1
2 Advanced plasmonic nanostructures: design, fabrication, and characterization	5
2.1 Numerical simulation tool	5
2.1.1 Surface integral equation method	5
2.2 Electron beam lithography (EBL)	6
2.2.1 Basics	7
2.2.2 Fabrication with PMMA and liftoff	7
2.2.3 Fabrication with negative resist HSQ	9
2.2.4 Wafer vs. chip size substrate	10
2.2.5 CATS vs. Layout BEAMER	10
2.2.6 Dose test, proximity effects, and adhesion	11
2.2.7 Techniques and tricks for improving alignment accuracy	12
2.2.8 Calibration of the Ag etching rate with low energy IBE	14
2.2.9 Fabricated plasmonic nanostructures with EBL	14
2.3 Focused ion beam lithography	20
2.3.1 Basic principles	20
2.3.2 FIB beam expanding problem	20
2.3.3 Sample fabricated with focused ion beam	22
2.4 Characterization tools	23
2.4.1 Scanning electron microscope	23
2.4.2 Atomic force microscope	24
2.4.3 Dark-field single particle scattering spectroscopy	24
2.4.4 Light transmission and reflection spectroscopy	24
2.4.5 Fourier imaging spectroscopy	24
2.4.6 X-ray photoelectron spectroscopy	25
	ix

Contents

2.5	Confocal fluorescence lifetime spectroscopy	25
2.6	Summary	26
3	Plasmonic silver nanostructures and film	29
3.1	Introduction	29
3.2	Deterioration of silver nanostructures over short period of time	32
3.3	Deterioration mechanism of Ag nanostructures and films	33
3.3.1	Oxygen or sulfur	33
3.3.2	Surface adsorbed water	34
3.4	Improvement of long-term, chemical, and thermal stability, and surface roughness	36
3.4.1	Chemically stabilize Ag nanostructures	36
3.4.2	Thermally stabilize Ag nanostructures	36
3.4.3	Improvement of the surface roughness of Ag films	37
3.5	Summary	39
4	Engineering fluorescence with negative and sandwich nanoantennas	41
4.1	Introduction	41
4.2	Engineering fluorescence with negative nanoantenna	43
4.2.1	Fluorescent dye molecules	43
4.2.2	Metallic nanohole design, fabrication and characterization	44
4.2.3	Experimental results	45
4.3	Discussion	47
4.3.1	Near-field enhancement	47
4.3.2	Improvement of emission directionality	47
4.4	Sandwich cavity antenna	48
4.4.1	Fabrication method	49
4.4.2	Optical properties of the fabricated sandwich cavity	50
4.5	Results and discussion	50
4.6	Summary	52
5	Engineering fluorescence with Fano plasmonic systems	55
5.1	Introduction	56
5.2	Fano plasmonic resonant system	57
5.2.1	Fano plasmonic resonant mechanism	57
5.2.2	Immobilizing the molecule in nanogap	59
5.2.3	Engineering the spectral overlap between the Fano resonance and the absorption/emission of the molecules	60
5.3	Fluorescence enhancement and lifetime	61
5.3.1	Experimental data	61
5.3.2	Numerical data	63
5.3.3	Comparison the results between experiment and calculation	64
5.4	Summary	66

6 Conclusion and Outlook	67
A Abbreviations	71
B Tracking the dehydrated Ag antenna for 14 weeks	73
C Numerical modeling of the fluorescence enhancement averaged over the 16 points	75
Bibliography	99
Curriculum Vitae	101

List of Figures

2.1	Comparison of ideal and rounded meshes	6
2.2	Schematic of the PMMA resist EBL combined with metal deposition and liftoff process.	8
2.3	Schematic for the process based on HSQ resist combined with EBL and IBE etching.	10
2.4	Schematic illustration of linewidth broadening.	11
2.5	Schematic of the alignment markers deployment strategy.	13
2.6	Calibration of the etching rate of Ag under low power IBE etching.	14
2.7	Single nanoparticle antennas. (a) Rectangular silver nanobar (scale bar 100 nm). (b) Gold square disk (scale bar 200 nm). (c) Circular aluminium disk (scale bar 200 nm)	15
2.8	Comparison of the antenna linewidth with and without adjustment of the dose.	16
2.9	SEM image of plasmonic gap antenna.	17
2.10	SEM images of complex plasmonic antennas.	17
2.11	Different types of fabricated metasurfaces for different optical effects.	17
2.12	Process flow for two-step e-beam alignment.	18
2.13	Dependence of 4-NRSA fabrication on alignment markers.	19
2.14	Large area small period disk array fabrication.	20
2.15	Comparison between sandwich cavity antennas fabricated by EBL and IBE.	21
2.16	Schematic illustration of FIB/SEM direct milling process.	21
2.17	Dependence of FIB milling on mask.	22
2.18	Different nanohole geometries fabricated with FIB in silver films.	23
2.19	Dark-field confocal fluorescence spectroscopy setup.	26
3.1	Comparison of the permittivity and quality factor for different plasmonic metals.	30
3.2	Deterioration of Ag and Au nanoantennas.	31
3.3	Ag nanostructure degradation over short period of time.	32
3.4	Mechanism of Ag nanostructure degradation.	34
3.5	Degradation of Ag nanostructures due to humidity.	35
3.6	Chemical stabilization of Ag nanostructures with dehydration.	37
3.7	Thermal stabilization of Ag nanostructures with dehydration.	38
3.8	Roughness improvement of Ag film with dehydration.	39

List of Figures

4.1	Flourescence modification using plasmonics.	42
4.2	4-nanohole silver negative antenna (4-NHSNA).	44
4.3	Fluorescence signal and decay histogram for 4-NHSNAs.	45
4.4	Fluorescence signal and decay histogram for 4-NHSNAs.	46
4.5	Near-field intensity enhancement for 4-NHSNAs.	47
4.6	Measured fluorescence emission patterns for 4-NHSNAs.	48
4.7	Schematic for fabrication of a cavity antenna with a molecule functionalized inside the cavity.	49
4.8	SEM image of the fabricated cavity antenna.	50
4.9	Optical properties of the cavity antenna.	51
4.10	Fluorescence image and decay histograms for the cavity antenna.	52
5.1	Fluorescence modification with Fano resonant plasmonic systems.	55
5.2	Mechanisms of Fano resonance for the generation of a nearly homogeneous hot spot in a 4-NRSA system.	58
5.3	Comparison of the near-field enhancement in the hot spots between a 4-NRSA system and a dipole antenna system.	59
5.4	Schematic of the two-step EBL process for the selective surface functionalization of molecules in the gap of the 4-NRSA.	60
5.5	Spectra overlap for the different designed configurations.	61
5.6	Fluorescence images and decay histograms for the different configurations. . .	62
5.7	Numerical modeling of a dipole emitter in the gap of a 4-NRSA.	65
B.1	Temporal tracking of morphology and optical properties of the 4-NRSA.	74
C.1	Schematic of the emitter positions in the gap of the 4-NRSA.	76

List of Tables

4.1	Comparison of the experimental fluorescence enhancement and the modified lifetime for all three types of 4-NHSNAs.	46
5.1	Comparison of the experimental and calculated fluorescence enhancement and the modified lifetime for all three configurations.	64
A.1	Abbreviations for instruments	71
A.2	Abbreviations for chemistry	71
A.3	Abbreviations for physics	72
C.1	Calculations for configuration A	76
C.2	Calculations for configuration B	77
C.3	Calculations for configuration C	77

1 Introduction and thesis outline

Gold (Au), a precious metal, has a long history in human civilization, gold jewelry has been found in the Tomb of Djer, the king of the first Egyptian dynasty (2500 B.C) and little squares of gold has been used as the Chinese money (since 1091 B.C) [1, 2]. Even today, gold is still the reference used in the monetary systems all around the world. Soluble (colloidal) Au nanoparticles were discovered around 4-5 century B.C. They were probably used to make the famous Lycurgus cup which uses colloidal Au nanoparticles to transmit red light while reflecting green light [1–3]. In addition to Au, silver (Ag), copper (Cu) nanoparticles have also given artistic colorful touches to the ancient Chinese porcelain (since 960 A.D) [4], pottery of Deruta (since 1557) [5] and the colorful stained-glass windows in many medieval churches [6]. Scientists tried to uncover the mechanism of these magic color since the 1800s, from Jeremias drinkable Au particle solution to Faraday reversible color experiment [7]. In the 1900s, Mie theory explained that the color of the particle is size dependent [6, 8, 9]. The modern explanation by Richters in 1950s of surface plasmons as the electronic oscillations excited by incident light at a metal-dielectric interface inspired the flourishing field of plasmonics [10]. Localized surface plasmon resonances (LSPR) are coherent oscillation of electrons at the metal-dielectric interface of nanoparticle systems [11–13]. While they are known as propagating surface plasmons when they are excited at the planar metal-dielectric interface [14, 15].

Surface plasmon resonances (SPRs) in general have attracted significant attention ever since the low reflection dip appearing when shining light on a mirror surface with a diffraction grating was observed in 1902 by Wood [10, 16, 17]. A full understanding of the corresponding physics was not possible until Otto, Kretschmann, and Raether excited SPR with the famous Otto-Kretschmann configuration [12, 14, 18, 19], although Lord Rayleigh and Fano had tried to interpret this phenomenon previously [8, 20, 21]. The first kind of applications of SPR is biosensing as the resonance is extremely sensitive to the refractive index change of the surrounding materials [10]. The strongly enhanced near-field confined in subwavelength volumes by plasmonic nanostructures has also been used for numerous applications from photovoltaics, single photon source, single molecule detection, fluorescence imaging [22–31], plasmonic lasing [32–45], to Raman spectroscopy and nonlinear optics [46–58].

Materials have always been a central topic for the plasmonic community as different noble metals exhibit plasmon resonances varying in a broad wavelength range. For instance, the three most popular metals, Aluminum (Al), Ag and Au show favorable resonances (in the sense of relative low losses) in the range from ultraviolet (UV) to visible (VIS) and infrared (IR) [59, 60]. Plasmonics metals are often chosen by considering the loss; for example, Al is very good as a photocatalyst in UV because it has low losses in that region of the spectrum where Au exhibits high losses caused by interband transitions; Au is the metal of choice for plasmonics, thanks to its chemical stability, however, when low loss is required Ag is often the first choice, such as in plasmonic lasing applications, although it is very unstable [39]. From middle IR up to tera-hertz (THz), graphene has been shown to be an excellent plasmonic material [61–63].

Modern nanofabrication technologies open up attractive opportunities to realize plasmonic applications [64, 65]. Plasmonic nanoantennas which show similar function like their counterparts in the microwave have been booming the applications in nanoengineering [66, 67]. Yagi-Uda optical antennas are the most famous examples that open promises for photonic nanocircuit [38]. Optical antennas with different shapes have been designed to show applications in biosensors as the LSPR are very sensitive to their shapes [13, 68–70]. Negative optical antennas (metallic nanoholes) exhibit extraordinary optical transmission and have also led to numerous applications [65, 71–78].

This thesis has been driven by my interest in plasmonic phenomena, their promising applications and the utilization of all the facilities that are needed to design, fabricate and characterize the systems and devices that support them. The central goal of this thesis is to develop plasmonic nanostructures that can be used to study the dynamics of molecular interactions with plasmonic antennas. The thesis starts with the optimization and the development of top-down fabrication methods to obtain well defined gap antennas as well as developing original top-down fabrication processes that enable nanofabrication over large areas. Then, I study the fabrication of perfectly symmetric multilayer (tandem) antennas and I obtain the highest overlay accuracy. The next step is to find a proper plasmonic material with low losses that can be used to fabricate different antennas with the previously mentioned optimized top-down fabrication methods. In this thesis, I choose to work with Ag due to its low losses. The short stability of Ag has motivated me to investigate the mechanisms behind the rapid deterioration of Ag nanostructures and to develop a method that stabilizes Ag nanostructures over long periods of time. The resulting improvement of long-term chemical and thermal stability opens new perspectives for Ag nanostructures applications, since Ag is a lower loss and less expensive plasmonic material than Au. Confining emitters at subwavelength scales is a very interesting topic in nano and quantum optics [79, 80]. Different plasmonic antennas, such as Yagi-Uda, single rod, small gap dipole, and negative antennas, have been proposed to engineer optics at the nanoscale, e.g. for single molecule detection [24–31, 38]. These promising applications, as well as the accompanying nanoengineering challenges, have motivated me to design plasmonics nanostructures that can provide plasmonic hot spots and to develop a method to immobilize emitters at the place where the hot spot lies, in order to enhance spontaneous

emission. I also designed a negative plasmonic antenna to study fluorescence enhancement by exploiting the near-field enhancement and improving the directionality of the fluorescence emission. This is a simple but effective way to confine emitters in plasmonic hot spots with a size of $100 \times 100 \text{ nm}^2$. Plasmonic cavity antennas are another type of nanostructures that can confine molecules in an area of $100 \times 100 \text{ nm}^2$. I have developed a sandwich cavity antenna with the molecules immobilized in the middle of the cavity using a chemical surface functionalization method. To push the limits even further, I have proposed a 4-nanorod Ag antenna (4-NRSA) that has most of the energy confined in the near-field and produces a nearly homogeneous hot spot with size $30 \times 30 \text{ nm}^2$ through the excitation of a Fano resonance. Selective chemical functionalization and two-step e-beam lithography are combined to immobilize the molecules only in the $30 \times 30 \text{ nm}^2$ gap area in order to enhance the fluorescence. Numerical modeling of the molecular-plasmonic system has also been developed to fully understand how the Fano resonance can preferably enhance the fluorescence at the absorption, and emission peaks of the molecule.

This thesis is organized as follows. Chapter 2 gives a general description of the numerical modeling, nanofabrication, and characterization tools used throughout the thesis. The fabrication processes that have been developed for advanced plasmonic nanostructures are the main focus of this chapter. Difficulties associated with the nanofabrication are explained and solutions are provided. Chapter 3 is dedicated to investigating the deterioration mechanisms of silver nanoantennas and films, and to develop a process to chemically and thermally stabilize them. Two different plasmonic nanostructures, metallic nanoholes and sandwich cavity antennas are used to engineer fluorescence within a $100 \times 100 \text{ nm}^2$ area in Chapter 4. Metallic nanoholes offer subwavelength area strong near-field enhancement and can improve the directionality of plasmonic devices. Also, metallic nanoholes screen away from the noise and consequently improve the signal to noise ratio. In sandwich cavity antennas combined with surface chemical functionalization, molecules can be directly placed right in the middle of the sandwich cavity, where the near-field is enhanced within an area of diameter 100 nm. In Chapter 5, a Fano resonant plasmonic nanostructure (4-NRSA) is designed to produce a hot spot in the antenna gap (with size of $30 \times 30 \text{ nm}^2$), where molecules are immobilized using a specifically developed process. How Fano resonances supported by those structures can influence the fluorescence enhancement and modify the fluorescence lifetime is then studied. Chapter 6 summarizes the whole thesis and provides an outlook for future work on molecular plasmonic devices with silver as material of choice.

2 Advanced plasmonic nanostructures: design, fabrication, and characterization

To achieve the results presented in this thesis, a series of tools were necessary for each step. Applying numerical calculations to optimize the design of the nanostructures was the first step. Different fabrication processes have then been developed and utilized to fabricate the most promising nanostructures. These various tools are described in this chapter, starting with the different detailed process flows, while the fabricated structures are grouped together at the end of the chapter. Finally, several metrology tools have been used to characterize the properties of the fabricated structures.

2.1 Numerical simulation tool

2.1.1 Surface integral equation method

In this thesis the surface integral equation method (SIE) is used to numerically characterize the response of plasmonic nanostructures [81–83]. The optical properties, such as the scattering spectrum, transmission spectrum, near-field distribution, surface charge, etc. are obtained with SIE. Furthermore, the molecular-plasmonic system (a molecule in the vicinity of a plasmonic antenna) is also modeled with SIE. SIE uses the Green's tensor to solve Maxwell's equation for each domain that is described as a triangle mesh on the surface of the different nanostructures under study. As it uses surface integral instead of volume integral, it is quite fast. It can deal with ideal nanostructures as well as a realistic mesh extracted from real fabricated nanostructures. For example, the nanoantennas that are fabricated with electron beam lithography usually have round edges as schematically shown in Fig. 2.1(b). The resonance of the spectrum of the rounded structure will shift compared to the ideal sharp-edged one Fig. 2.1(a) [84]. Taking this into account at the design step requires a modification of the geometry in order to compensate that shift. Rounded nanostructures are used throughout the entire thesis.

For computing the scattering cross-section (SCS), the transmission, and the reflection from a plasmonic system, a plane wave illumination is used and a single computation is performed.

Chapter 2. Advanced plasmonic nanostructures: design, fabrication, and characterization

To model a molecular-plasmonic system, the calculation is divided into two steps. First, the structure is illuminated by a plane wave with linear polarization to compute, the near-field enhancement and possibly the charge distribution. Second, a dipole illumination is used to mimic the fluorescence by the molecule. Scattering power and Ohmic losses are hence calculated under dipole illumination.

For the plasmonic materials (Au, Ag, Al), I use the experimental dielectric function from Johnson and Christy [85]; the surrounding refractive index is considered homogeneous with a value of 1.33 to approximate the small substrate-induced frequency shift of the plasmon resonance [86].

In addition to an infinite homogeneous background, the SIE framework can also handle periodic structures [87]. This is useful to compute periodic structures and also makes possible the inclusion of substrates. I have used periodic SIE calculations for the periodic aperture arrays reported in Chapter 4.

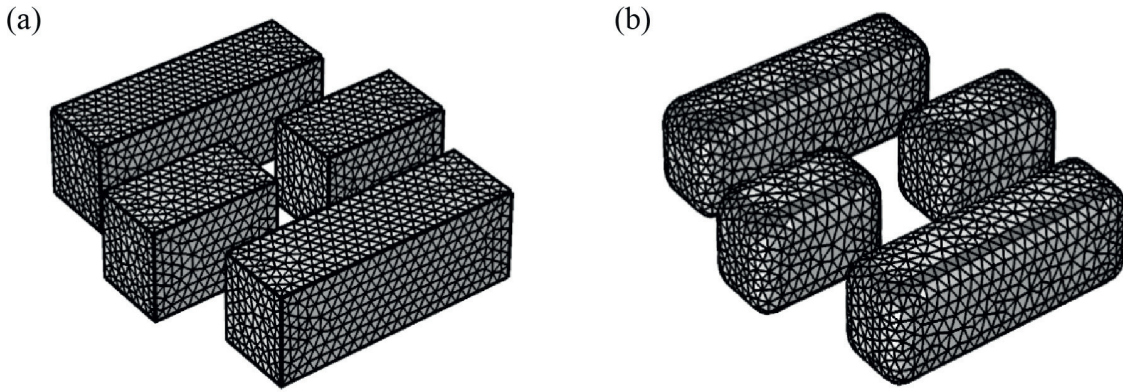


Figure 2.1: Comparing the mesh. (a) Ideal and (b) Rounded 4-nanorod structure.

2.2 Electron beam lithography (EBL)

The different nanofabrication steps performed in this thesis were conducted at the EPFL Micro-Nanotechnology Center (CMI). The fabrication methods for plasmonic nanostructures can be divided into two main families: top-down methods like electron beam lithography (EBL) [88–91], focused ion beam (FIB) [92–95], nano imprinting lithography [96–98]; and bottom-up methods such as chemical synthesis [99–102] or nanosphere/colloidal lithography [103–105]. In this chapter, I focus on introducing FIB direct patterning and EBL combined with liftoff or ion beam etching (IBE), which represent the main fabrication methods used in this thesis. The plasmonic nanostructures fabricated with these two approaches will be exploited in Chapter 3, Chapter 4 and Chapter 5.

2.2.1 Basics

EBL is a well established technique that has been used to realize submicrometer structures since the 1960s and pushed to resolution in the 5-10 nm range since the 1990s [95, 106]. A focused high energy electron beam is used to write the nano pattern. The defined pattern is written in a resist spin coated on the substrate, which solubility is selectively modified by the high energy electrons. The Gaussian Beam Direct Write System Vistec EBPG5000 System used in this thesis operates with a 100 keV thermal field emission gun and supports various pattern frequencies up to 50 MHz, with a minimum pixel size of 1.25 nm and a beam size of 5 nm for the stable temperature $21\text{ }^{\circ}\text{C} \pm 0.1\text{ }^{\circ}\text{C}$ established in the CMI at EPFL [107]. Similar to a photolithography process, EBL fabrication includes manually spin coating the resist, writing the pattern and developing the resist with appropriate chemicals. The specific steps and special techniques developed for the different types of resists will be explained in the following sections. There exist two types of resists for EBL, namely positive resists, such as Poly Methyl Methacrylate (PMMA) [90] or Styrene Methyl Acrylate (ZEP) [108], and negative resists like Hydrogen Silsesquioxane (HSQ) [109] or n-LOF [110]. These different resists are adapted either for liftoff or etching. For instance, PMMA is suitable for liftoff as it can be easily dissolved in a solvent, while ZEP is used for dry etching masks. Similarly, for the negative resists, HSQ is used for etching and n-LOF is a liftoff resist. The utilization of PMMA and HSQ will be discussed in greater details in the following, as they were used in this thesis.

2.2.2 Fabrication with PMMA and liftoff

Using EBL to pattern well-defined geometries combined with thin film evaporation and liftoff process is the routine method to fabricate nanostructures on different types of substrates, including glass and silicon. For this thesis, the substrates are mainly different glasses: thin D263 glass (SCHOTT AG Germany), float glass (Guinchard, optical glass Switzerland) or quartz (SCHOTT AG Germany) since most samples must be characterized optically in the visible spectrum range. This process can be used to fabricate plasmonic nanoantennas with different shapes, including nanodisks, nanorods, and gap antennas, etc. The full process flow is schematically shown in Fig. 2.2.

A prior cleaning step for the substrate is necessary before resist coating. There are two cleaning options, one is to use oxygen plasma (500 W Tepla 300) for 1 minute to clean the dust from substrate and activate the surface. The other way is to use acetone followed by isopropyl alcohol (IPA) to clean the substrate for two minutes (each solvent) and then dry with nitrogen (N_2) gas. Both methods have been working fine and I have not been adhesion problem with PMMA on glass substrates. The oxygen plasma method is especially well suited for full-wafer processes (the CMI uses standardized 4-inch wafers), while the solvent approach is used for chip size substrates ($20\text{ mm} \times 20\text{ mm}$). A dehydration process at $180\text{ }^{\circ}\text{C}$ for 5 minutes, pre- and post-baking should be applied for each layer of PMMA coating. The temperature of $180\text{ }^{\circ}\text{C}$ is optimized not only to remove the solvent from the resists but also let the resist solution

Chapter 2. Advanced plasmonic nanostructures: design, fabrication, and characterization

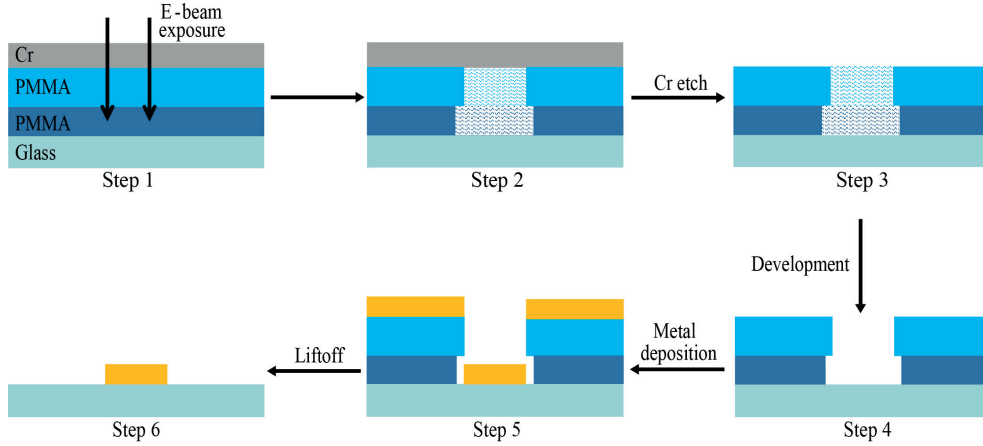


Figure 2.2: Schematic of the PMMA resist EBL combined with metal deposition and liftoff process.

re-flow on the substrate to obtain a homogeneous thickness of the resist layer. The thickness of the combined two PMMA layers (PMMA, from Microresist Technology GmbH) should be at least twice the thickness of the targeted metal film thickness for the nanostructures. We have optimized the first PMMA 495 kDa layer coated with 6000 rpm which gives a thickness of 120 nm and the second PMMA 950 kDa layer coated with 6000 rpm which gives a thickness of 60 nm. The combined thickness is 180 nm that is a very good thickness for liftoff of a 40 nm metal layer (Au, Ag or Al). For thicker metals, for instance, 200 nm platinum (Pt) or Au as alignment markers, a total resist thickness of 600 nm was found to be appropriate for a good liftoff. As the high energy electron beam is focused on the surface of the resist during the exposure, charge accumulation occurs since both resist and substrate are non-conductive. Therefore a conductive layer (e.g. chromium) is needed to dissipate the charge [111–113]. Thus, before the e-beam exposure, a 20 nm thick layer of chromium (Cr) is evaporated with a thermal evaporator (Leybold Optics LAB600H) on top of the resist.

The next step is to expose the defined nanostructure pattern. L-Edit (Tanner) and CleWin (PhoeniX) softwares have been used to design the pattern of the nanostructures. The pattern is converted to e-beam readable .gpf file using the conversion software CATS (Synopsis) or Layout BEAMER (GenISys) and converted into a job file readable by the e-beam writer. When running the job, the high energy electrons hit the resist and break the bonds of the polymer. PMMA 495 kDa is more sensitive than PMMA 950 kDa, and consequently results into an undercut of the structure in the bottom layer [107, 114] as shown in Fig. 2.2 (Step 2). The 20 nm Cr layer deposited as conducting layer has to be etched with fresh acid (mixed Ceric ammonium nitrate - CAN and Perchloric acid - PCA) for 30 s in the case of a chip size substrate and up to 1 minute for wafers. The sample is showered three times in deionized (DI) water and dried with N₂ gas. Subsequently, it is developed with PMMA developer 1 : 3 methyl isobutyl ketone : isopropanol (MIBK : IPA) for 1 minute for chip size samples and 90 s for wafers. Then the sample is showered again with pure IPA for 1 minute to remove all the residual solvent and

finally dried with N₂ gas. Cr etching and development should be done as quick as possible (no later than 4 hours) after the sample has been exposed with EBL because the exposed resist diffuses into the non-exposed resist when the waiting time between the exposure and development is too long. This will essentially make the liftoff difficult or at all possible. The advantage of the double layer PMMA is shown in the metal deposition and liftoff process. The side wall of the bottom layer resist are not be covered or much less covered compared to a single layer resist, such that acetone can attack the bottom layer resist easily and make the liftoff easier (Step 5 and Step 6 in Fig. 2.2). The metal deposition is performed with a long distance target to substrate configuration to avoid resist over heating and minimize deposition on the resist side walls; the sample holder is also lifted so that the target is perpendicular to the substrate. A soft oxygen plasma is necessary to remove residues of the resist and activate the surface right before the metal deposition. This step will make sure that the patterned area is clean and ensures better adhesion for the metal. Consequently, the nanostructure defects caused by the resist residues will be reduced. The liftoff with acetone and sometimes with the help of ultrasonic bath (TPC-40 Allendale Ultrasonics UK, for 30 s at 60°C) is performed after the metal deposition for one entire day. Finally, the sample is showered with IPA and dried with N₂ gas.

2.2.3 Fabrication with negative resist HSQ

The negative resist HSQ (XR 1541 006 Dow Corning) is inverse to the positive PMMA resist in the sense that the resist areas exposed with electrons remain during the development (with solvent tetramethylammonium hydroxide for 30 s) and form an etching mask to transfer the pattern to the materials underneath. HSQ becomes silicon dioxide after e-beam exposure [115, 116], which can be used as a good mask for etching. HSQ not only offers better resolution [109, 117] but also enables the realization of good sandwich layered structures with straight edges, which are not possible with PMMA combined with a liftoff process since the PMMA masks is clogged up by metal during the deposition. Examples of layered structures fabricated with liftoff and etching will be compared in Fig. 2.15. However, it is difficult to remove HSQ after it has been exposed by e-beam and developed. Thus a thin sacrificial layer of silicon (Si) can be used on top of the metal to remove HSQ at the end of the whole process. Also, the adhesion of HSQ is better on silicon than on metals [118] and the thin Si sacrificial layer makes the fabrication better. The full process flow is schematically shown in Fig. 2.3. The metals (Au, Ag, and Al) should be first deposited before coating HSQ resist, which is in contrast to the PMMA process where metal is deposited after e-beam exposure and development (compare Figs. 2.2 and 2.3). For a thickness of 40 nm metal, 80 ~ 120 nm HSQ is sufficient as hard mask for ion beam etching (IBE). For the IBE process (Step 5 in Fig. 2.3), the etching rate of different metals (Au, Ag and Al) must be estimated. In this thesis, this process was extensively used for Ag and the corresponding etching rate with low power ion beam has been investigated in detail in Sec. 2.2.8. The last step is to etch the Si layer away and simultaneously remove the remaining HSQ, which is done in a potassium hydroxide (KOH 40 %) bath for 40 s. Finally, the sample is washed with DI water and dried with N₂ gas.

Chapter 2. Advanced plasmonic nanostructures: design, fabrication, and characterization

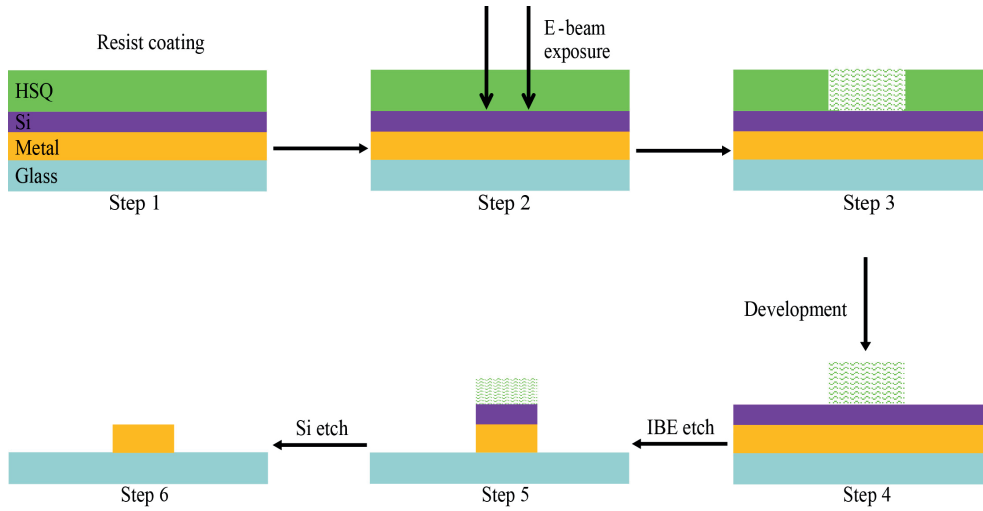


Figure 2.3: Schematic for the process based on HSQ resist combined with EBL and IBE etching.

2.2.4 Wafer vs. chip size substrate

The entire CMI facility has been designed to work with 4-inch wafers, which is not always optimal when fabricating plasmonic nanostructures. I have therefore used both full wafers or chips as substrates for the nanofabrication and I discuss here the different corresponding issues. The first issue comes from the thickness of the substrate. Depending on the glass, there are two thicknesses: $150\text{ }\mu\text{m}$ for D263 borosilicate and $550\text{ }\mu\text{m}$ for float or quartz glasses. Take the thinner 4-inch wafer as an example: the wafer is not flat when it is heated on the hot plate at $180\text{ }^{\circ}\text{C}$, e.g. for resist baking. Consequently, the resist that is coated on the wafer is not homogenous and the thickness in the center of the wafer is normally larger. This means that for the EBL the dose should be adjusted, otherwise the nanostructures on a different part of the substrate will not be uniform when a constant dose is used. Thus, for thin substrates I recommend to dice the wafer into small chips, for example with the size of $20\text{ mm} \times 20\text{ mm}$. This is less problematic for the thick wafer as no obvious bending happens on the wafer during the high-temperature baking process. However, chip size substrates are a little bit more complicated to process than a wafer scale substrate because the holder for mounting the chip substrates is difficult to handle and it is tricky to have all the different chips exactly at the same height. Indeed, the e-beam resolution strongly depends on how good the focus is, which depends in turn on how flat the substrate is. Ideally, a super flat substrate should be used in order to produce uniform results; otherwise, the resolution can be ruined.

2.2.5 CATS vs. Layout BEAMER

There are two file conversion software that are used at the CMI in EPFL, namely CATS and Layout BEAMER. The CATS software has basic functionalities, which convert the designed nanostructure pattern from .gds to .gpf files. Layout BEAMER however provides more freedom for optimization, for example, using different doses at different places of the nanostructure,

which produces better fabrication results. One of the most useful functionality is to apply different doses between the edges, corners and body parts of the antennas in order to achieve the required linewidth for the different nanorods, the correct diameter for circular nanodisks or the right gap between two adjacent nanorods. The problem essentially comes from the overlapping of the focused electron beam (smallest beam size around 5 nm with a current of 200 pA) while pixel lateral length is 1.25 nm. Consequently, the discretized pixel will be over exposed by the beam, resulting in a broadening of the designed size. For instance, a designed linewidth of 40 nm could end up with a 60 nm linewidth if no dose adjustment is used. Similarly, a decreased gap from the designed 40 nm to 20 nm could also happen. The fabricated samples will be compared in Sec. 2.2.9. A schematic of this phenomenon is shown in Fig. 2.4.

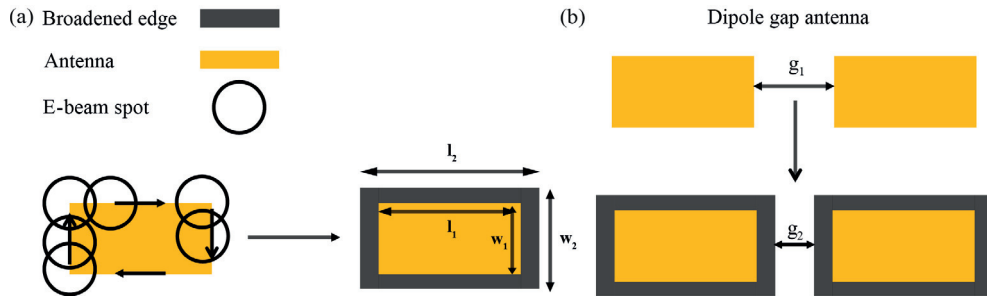


Figure 2.4: Schematic illustration of linewidth broadening.

As shown in Fig. 2.4 a typical antenna structure is discretized into many pixels during the e-beam exposure and each pixel is scanned by the e-beam with a spot size around 10 nm. Since the beam size is larger than the pixel size, the pixel will be over exposed by several beams and the predefined structure will also be extended outside its designed boundary. Thus, the real size of the exposed area will be larger than the designed area. As shown in Fig. 2.4(a), the length of a single rod antenna is increased from l_1 to l_2 and the width is increased from w_1 to w_2 . The gap of a dipole gap antenna is decreased from g_1 to g_2 as shown in Fig. 2.4(b). There are two ways to overcome this linewidth broadening issue. The first one is to shrink the linewidth in the design by about 10 to 20 nm. The other way is to take the advantage of Layout BEAMER and use a lower dose (typically half the dose) at the edge of the antenna compared to the body part, such that the exposed area will be smaller.

2.2.6 Dose test, proximity effects, and adhesion

The time to expose a specific area depends on the dose and the beam current; the relation between the dose, the current and the exposed area is defined by Eq. (2.1) [119]:

$$D = \frac{t \cdot I}{A}, \quad (2.1)$$

where D is the dose with units $\mu\text{C}/\text{cm}^2$, t is the time to expose the area A . For most of the nanostructures that I have fabricated with two layers of PMMA as resist, a $900 \mu\text{C}/\text{cm}^2$ dose

Chapter 2. Advanced plasmonic nanostructures: design, fabrication, and characterization

gives decent nanoantennas for a beam current of 200 pA. A too low dose does not expose the area sufficiently, while a too high dose broadens the exposed area significantly. Using HSQ as an etching mask, for a 200 pA current a $6000 \mu\text{C}/\text{cm}^2$ dose gives decent nanostructures.

A small current gives in principle a small beam size; unfortunately, we see from Eq. (2.1) that the exposure time will be dramatically increased for a fixed dose when such a small current is used to expose a large area (typically mm^2). Another problem associated with using a small beam when exposing large and dense nanostructure areas is that the proximity effect can cross-link the resist and the liftoff is not possible anymore [120–124]. To overcome this problem, I have used single point exposure with a large beam current 200 nA to produce large arrays of simple disks, as shown in Fig. 2.14. This not only solves the over exposure issue but also dramatically decreases the exposure time compared to using a small current beam. For example, using a high current of 200 nA with a beam diameter of 102 nm [107], a single exposure is sufficient to produce a circular disk with a 100 nm diameter.

Poor adhesion between resist and substrate or between the deposited metal and the substrate is often an issue in plasmonics. I have not encountered such problems for PMMA on glass substrate when the glass substrate is properly cleaned with oxygen plasma or acetone and IPA. I have observed however that HSQ has a problem for coating on an Ag film, as it cannot spread smoothly over the silver. Since it was reported that the adhesion of HSQ is better on Si than on metals [118], I have added a thin Si layer on top of the metal.

Adhesion problems are common between metals (Au, Ag, and Al) and substrates (especially on a glass substrate for liftoff) [125]. Titanium (Ti), Cr, silane, and thiol molecules improve the bonding between the metal layer and the glass substrate [126–130]. However, Ti and Cr layers disrupt the plasmonic resonance due to their absorption [131–133]. Silane and thiol molecules have been showing comparable good adhesion for gold in form of non-lossy adhesion [134] and a 1 nm oxidized silver has been proved as an efficient adhesion method for Ag and Al nanostructures [135].

2.2.7 Techniques and tricks for improving alignment accuracy

Alignment of multiple EBL exposure is required for complex structures fabrication; for example if one would like to connect electrodes to a nanoantenna, a second time EBL would be necessary, which would require alignment to position the different structures one with respect to the other. Unfortunately, this alignment is very difficult, for the three following main reasons: beam drifting caused by thermal effect, poor overlay of the e-beam itself [136] and error in measurement of the substrate height [137]. The thermal effect caused beam drifting can be minimized by decreasing the temperature difference between the sample holder chuck and the exposure chamber with at least 1 hour loading prior exposure [136]. The overlay error caused by the e-beam itself (charging in the column, chamber, distortion in the e-beam deflection field) is not easy to get rid of and can be very large depending on the system [136]. The height measurement error can be improved by coating a good layer that acts as a mirror

to help the laser measure the exact height [138]. The overlay accuracy can be improved by placing markers very close to the defined pattern [137]. Alignment markers are created so that the machine first finds them and recognizes the coordinates that the job defines and then exposes. For the second EBL exposure, the machine tries to detect the same markers that have been used the first time and then finds the coordinates where the structures have to be exposed. A standard alignment marker system includes a coarse large pre-alignment array (20×20) and a local small alignment marker array (3×3) with a pitch of $200 \mu\text{m}$, respectively. For good conducting substrates, a wafer scale alignment is reliable but for glass substrates which have the issue of charging effect, a chip size substrate is always preferred for accuracy requirements. Normally, two-level alignment markers as previously described are sufficient. However, to improve the alignment accuracy – especially for glass substrates – third level (close to the pattern) local markers provide significant improvement for the alignment accuracy. A schematic illustration of the multi-level alignment markers is shown in Fig. 2.5. The materials for alignment markers are Au and Pt for positive markers that are $200 \sim 300 \text{ nm}$ thick and $10 \sim 20 \mu\text{m}$ square disk arrays; $1 \sim 3 \mu\text{m}$ depth Si hole array can also be used as negative markers.

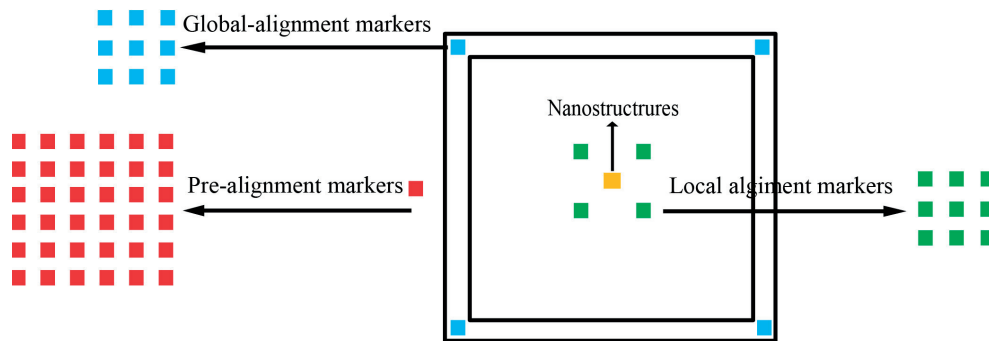


Figure 2.5: Schematic of the alignment markers deployment strategy.

The standard alignment marker system is two levels and represented by the red square array (pre-alignment markers) and the light blue arrays (global alignment marker) in Fig. 2.5. With this two level alignment strategy, reasonably good alignment accuracy can be achieved on Si substrates because negative alignment markers (Si microhole arrays) made with the RIB method exhibit very high contrast thanks to their sharp edges. However, on glass substrate, positive markers are used. The edges of the markers show less contrast compared to negative markers because the markers made with liftoff have a poor morphology at the edge. A third level of alignment markers, called the local markers and represented in green color in Fig. 2.5, which are placed very close to the nanostructures (yellow color) are required to achieve the best resolution accuracy (10 nm for the Vistec EPBG 5000 e-beam). This approach will be illustrated in Fig. 2.12.

2.2.8 Calibration of the Ag etching rate with low energy IBE

The etching rate for different materials in the process with negative resist HSQ combined with IBE etching is the first issue that one should consider because too short or too long etching time will result in insufficient or too much etching. The Ag etching rate with low power (50 V, 250 W) at -10°C has been calibrated on the Nexus IBE350 system (Veeco) as Ag is the plasmonic material that has been processed by IBE in this thesis. The Nexus IBE 350 dry etching system operating with high energy Ar ions (Ar ion source with RF plasma generator, 1.8MHz, 2kW maximum) purely physically sputters the target material (e.g., Ag) without any chemical precursors. To determine the Ag etching rate, a 200 nm thick Ag film is deposited on a float glass substrate with a chip size of $20\text{ mm} \times 20\text{ mm}$. In total, eight chips are prepared under the same conditions and each of them is etched with a different duration from 10 s up to 150 s. The thickness of the etched Ag film for each period of time is estimated by checking the cross-section of the film with FIB, as shown in Fig. 2.6(a). A Pt layer is deposited to protect the silver films prior to carrying out the FIB cut with a beam current of 10 pA under 30 kV acceleration voltage. The eight thicknesses with different etching times are measured and a linear function fitted to these experimental data, as shown in Fig. 2.6(b). The resulting etching rate of Ag for low power (50 V, 250 W) IBE process is 1.6 nm/s.

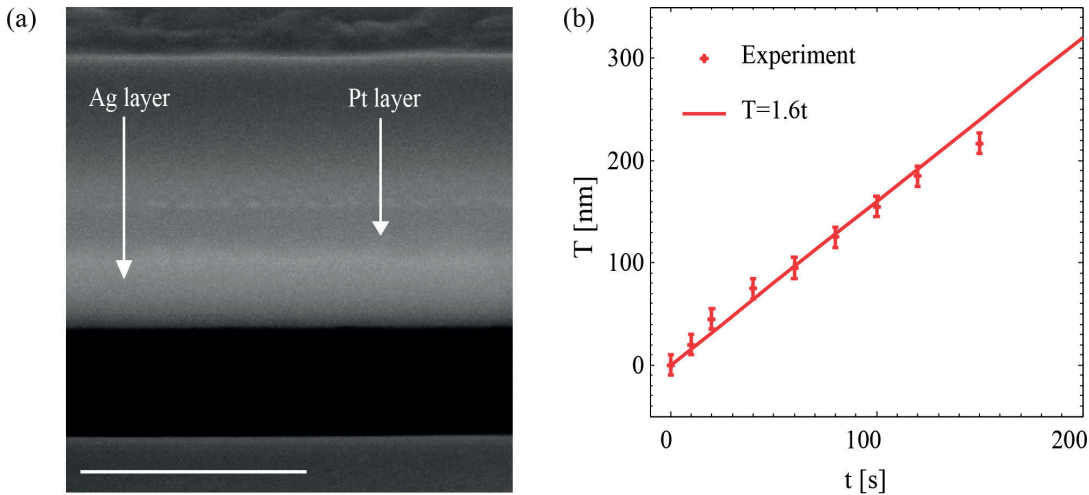


Figure 2.6: Calibration for the etching rate of Ag under low power IBE etching. (a) SEM image of the cross section for a typical etched film; the scale bar is 500 nm. (b) Etching rate of Ag under low IBE: the data shows the etched thickness T as a function of time t , together with a linear fit of the experimental data.

2.2.9 Fabricated plasmonic nanostructures with EBL

This section illustrates some of the structures that has been fabricated using the previously described techniques.

Single nanoparticle antenna

Fabricated plasmonic nanostructures using the EBL combined with thermal evaporation of a metal film and liftoff process are presented in this section. To start with, single nanoparticle antennas made of Ag, Au, and Al are presented; they include different well defined shapes, such as rectangular nanorod, a square particle and a circular nanodisk as shown in Fig. 2.7(a), 2.7(b) and 2.7(c), respectively. All the three types of nanostructures are fabricated with the two layers positive resist PMMA and liftoff process described in section 2.2.2. The difference comes from the adhesion layers for different metals: for Au a 2 nm Cr layer is used as adhesion and for Ag and Al a 1 nm silver oxide layer is used. Individual nanoantennas with well-controlled shapes are the building blocks for more complex plasmonic nanostructures.

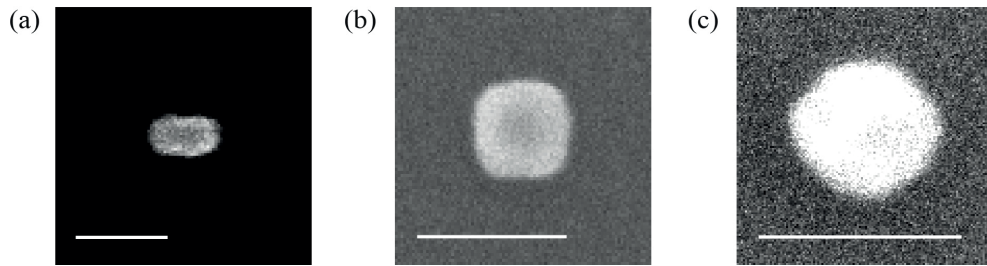


Figure 2.7: Single nanoparticle antennas. (a) Rectangular silver nanobar (scale bar 100 nm). (b) Gold square disk (scale bar 200 nm). (c) Circular aluminium disk (scale bar 200 nm) .

Linewidth correction

As previously mentioned, the direct e-beam exposure without dose adjustment broadens the linewidth of the nanoantennas because the beam size is larger than the pixel size. To demonstrate the broadening effect and its correction with Layout BEAMER, four nanorod silver nanoantennas (4-NRSAs) are fabricated on thin glass substrates and compared in Fig. 2.8. The 4-NRSAs shown in Fig. 2.8(a) are originally designed with a linewidth of 40 nm and a gap of 40 nm but the fabricated structure shows a linewidth of 60 nm and a gap of 20 nm, see the zoom in the right side of Fig. 2.8(a). However, with the adjustment of the dose for the edge and the body parts of the individual nanorod by Layout BEAMER, the fabricated 4-NRSAs in Fig. 2.8(b) exhibit well-defined geometry that corresponds to the designed parameters.

Well defined gap antennas

Plasmonic gap antennas represent a very popular type of nanoantennas, where the electromagnetic field in the nanogap can be strongly enhanced to form a hot spots for many applications, such as Raman spectroscopy, plasmonic trapping, sensing, fluorescence enhancement, and single photon sources [86, 127, 139–142]. The designed dipole antenna with a gap of 15 nm made of Au and the 4-NRSA with a gap of 35 nm made of Ag on thin glass substrates are presented in Fig. 2.9 as an illustration. More complicated plasmonic nanostructures can exhibit

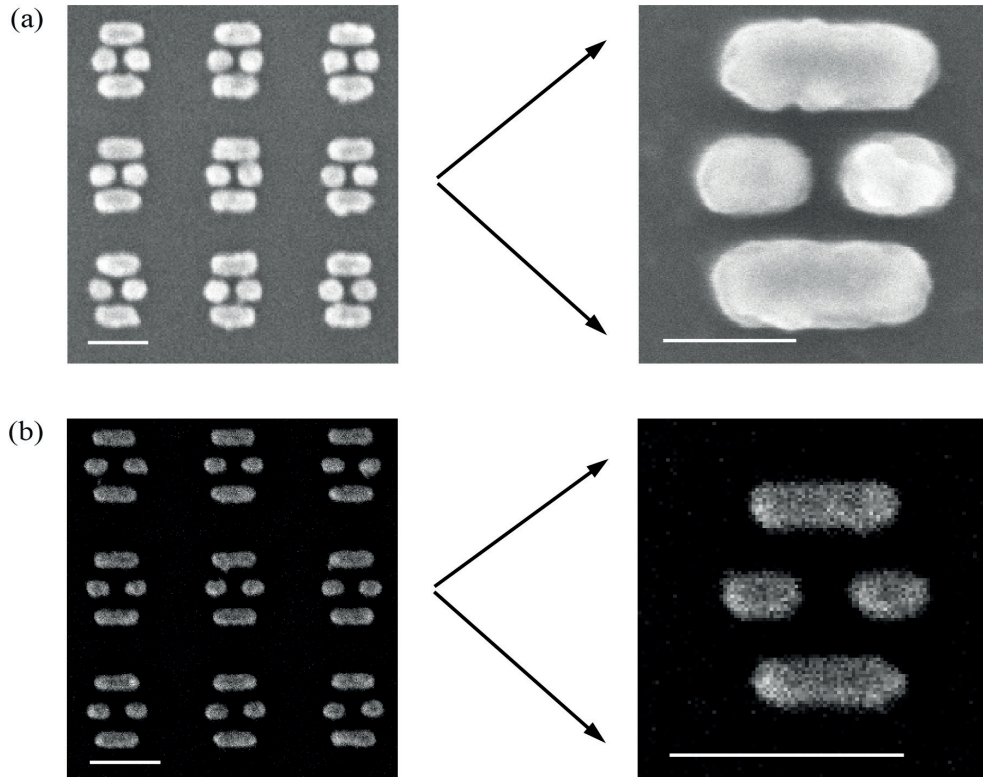


Figure 2.8: Comparison of the antenna linewidth with and without adjustment of the dose. (a) The fabricated 4-NRSAs without dose adjustment. Scale bars are 200 nm and 100 nm in the left and the right panels, respectively. (b) Fabricated 4-NRSAs with dose adjustment. Scale bars are 200 nm for both panels.

interesting optical responses, as illustrated in Fig. 2.10, which shows show a T-shape antenna made of Ag on a thick glass substrate that exhibits chirality, Fig. 2.10(a) [143], a loop antenna made of Ag on a thin glass substrate that supports a magnetic dipole mode, Fig. 2.10(b) [144], and a hepatmer made of Au on a quartz substrate to study second harmonic generation, Fig. 2.10(c) [145].

Metasurfaces

Metasurfaces are 2D metamaterials that can gradually change the amplitude, phase or polarization of incoming light along the optical path; they show very promising applications [146–153]. The challenge in the nanofabrication of metasurfaces is however the large area required to have exploitable devices. Examples of different metasurfaces are shown in Fig. 2.11; they include second-harmonic enhancement (structures made of Ag on quartz substrate [154]), optical vortex beam generation (structures made of Au on float glass substrate [155]) and optical flat (structures made of Au on float glass substrate [156]).

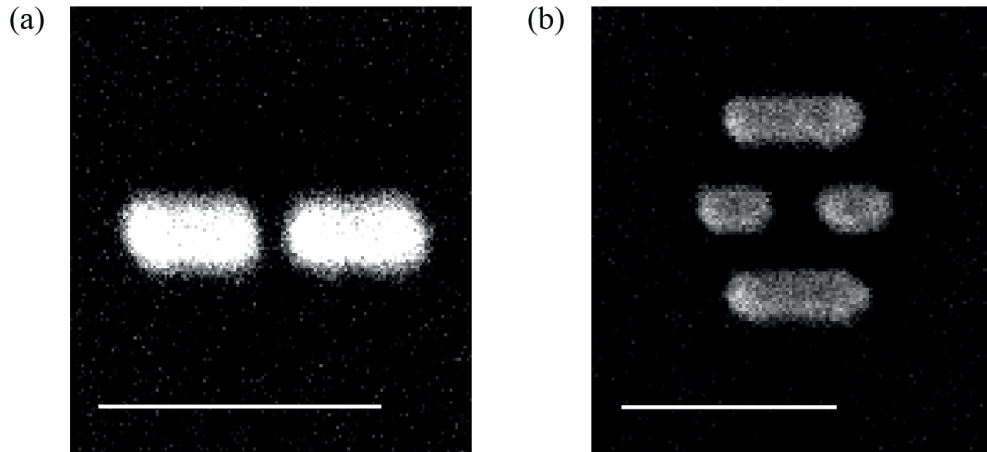


Figure 2.9: Plasmonic gap antenna. (a) Dipole gap antenna made of Au. (b) 4-nanorod gap antenna made of Ag. The scale bars are 200 nm.

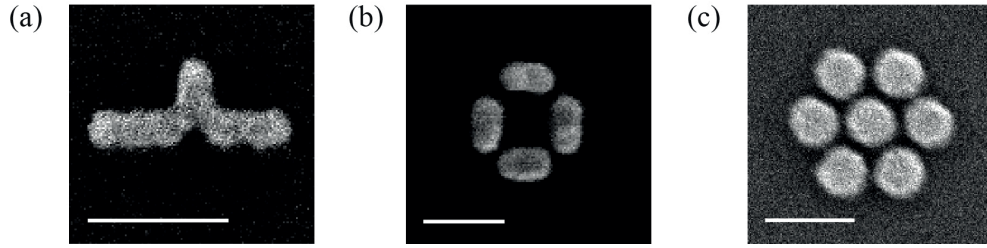


Figure 2.10: Complex plasmonic antennas. (a) T-shape antenna. (b) 4-bar loop antenna. (c) Heptamer antenna. The scale bars are 200 nm, 100 nm and 200 nm, respectively.

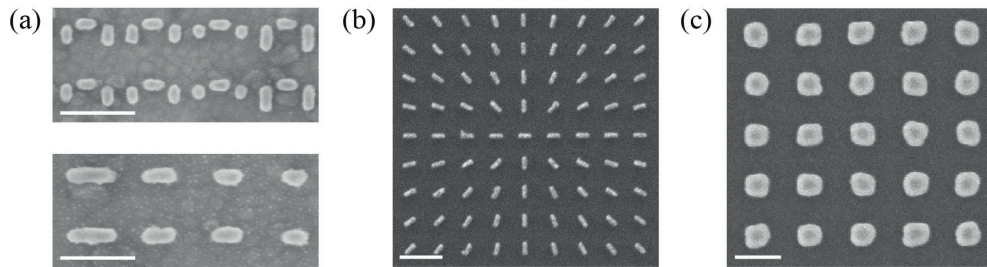


Figure 2.11: Different types of fabricated metasurfaces for different optical effects: (a) second harmonic enhancement (top panel: dolmen nanostructures and bottom panel: nanorods; scale bars 200 nm), (b) vortex beam (scale bar 300 nm) and (c) Au metasurface composed of a nanodisk array (scale bar 200 nm).

Alignment accuracy improvement

The process flow for a double EBL combined liftoff alignment process is shown in Fig. 2.12. Before the process starts, two-level and three-level positive alignment markers made of 200 nm thick Pt are patterned on a thin glass substrate. To demonstrate the alignment accuracy improvement, 4-NRSAs are fabricated with EBL combined with liftoff (Steps 1-4) using two-

Chapter 2. Advanced plasmonic nanostructures: design, fabrication, and characterization

level and three-level alignment markers (see section 2.2.7), respectively. During the second EBL combined with liftoff process (Steps 5-9), a nanoparticle (highlighted in yellow) is produced and positioned exactly in the gap of the 4-NRSA.

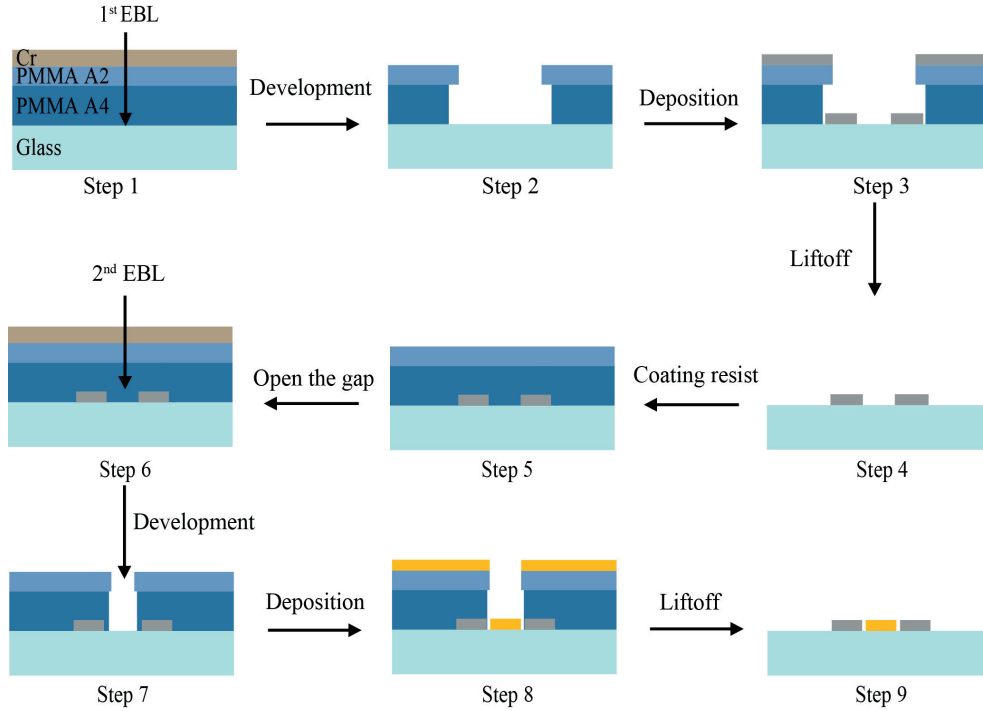


Figure 2.12: Process flow for two-step e-beam alignment.

The comparison of the fabricated antennas is shown Fig. 2.13. Fig. 2.13(a) is the result fabricated with standard two-level alignment markers. The nanoparticle (in the green square box) is supposed to be placed in the nanogap of 4-NRSA, but we observe in the resulting structure that it is misplaced by about 100 nm. This offset seems to be constant over the different nanostructures, as is visible for the neighboring nanostructure in the right of that panel. On the other, with a three-level alignment marker strategy, the additional particle is placed exactly in the middle of the 4-NRSAs gap, Fig. 2.13(b). The samples fabricated using the three-level alignment markers will be used in Chapter 5.

Large area antenna arrays

Al plasmonics has recently emerged as an interesting field of study, with applications in nonlinear optics and photocatalysis [60, 157–159]. Unfortunately, Al is difficult to fabricate using liftoff; although recent progress in our laboratory have demonstrated original processes that improve the nanofabricated structures [135]. Here I show the fabrication of large area ($3 \sim 7 \text{ mm}^2$) periodic Al circular disk antenna array with a period of 200 nm on a quartz substrate using two different e-beam exposure techniques combined with a liftoff process. Fig. 2.14(a) is the fabricated antenna array that is exposed with small beam current (200 pA) by rastering

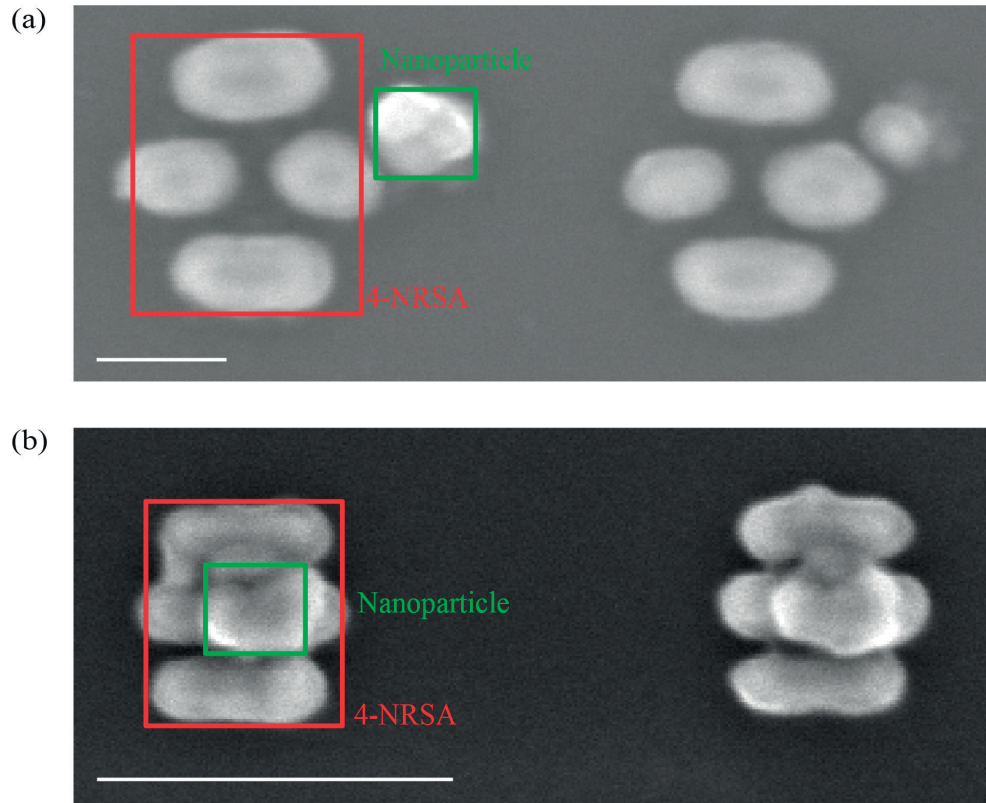


Figure 2.13: (a) 4-NRSAs fabricated with global alignment markers (two-level strategy, scale bar 100 nm). (b) 4-NRSAs fabricated with local alignment markers (three-level strategy, scale bar 300 nm).

each antenna into small pixels as described in Sec. 2.2.6. Proximity problems clearly influences the final liftoff, which is imperfect with a large portion of the metal remaining on the substrate. On the other hand, with single point exposure using a large current 200 nA and defocusing the beam to the corresponding size of the designed feature, e.g., 100 nm in diameter, perfect liftoff results are obtained, Fig. 2.14(b). Furthermore, this single point exposure approach is about 15 times faster than the rastering approach.

Sandwich antenna

Metal-insulator-metal nanosandwich antennas are good candidates for nanoengineering since their near-field enhancement is confined between the layers and they also exhibit emission directionality like a very primitive Yagi-Uda antenna [160–165]. Here I show two different approaches for the fabrication of such multilayered nanostructures. First, the fabrication of an asymmetric sandwich cavity antenna (Ag-SiO₂-Ag) with conventional EBL and liftoff process, that will be used in Chapter 4 for fluorescence studies, Fig. 2.15(a). The liftoff fabrication produces an asymmetric structure since the resist mask used for the metal evaporation gradually closes up, leading to slanted sides for the metal, as is visible in the tilted view in the right panel

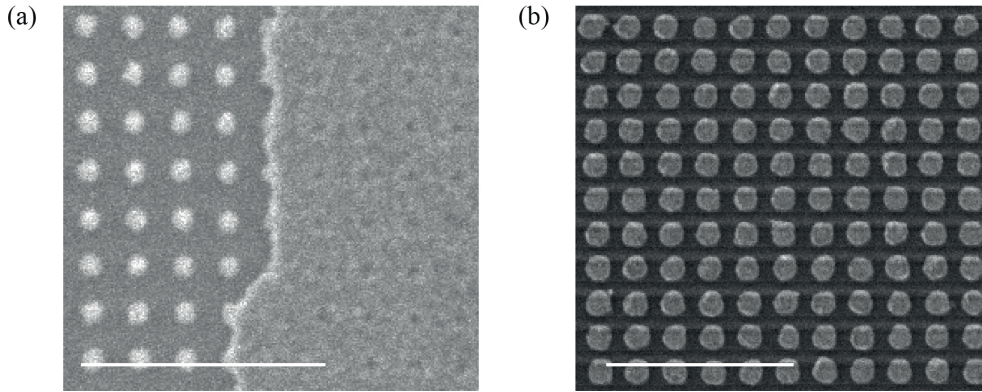


Figure 2.14: Large area small period disk array fabrication. (a) Imperfect liftoff associated with over-exposure of the resist caused by rastering each disk (scale bar 1000 nm). (b) Perfect liftoff over a large area antenna array achieved through single point exposure (scale bar 500 nm).

in Fig. 2.15(a). These slanted sides make the overall structure asymmetric. Second, when the structure ($\text{Ag-Al}_2\text{O}_3\text{-Ag}$) is fabricated with the IBE described in Sec. 2.2.3 using HSQ as a hard mask, it exhibits a very good shape with well defined sides, Fig. 2.15(b).

2.3 Focused ion beam lithography

2.3.1 Basic principles

Focused ion beam (FIB) is a direct milling technique based on high energy Ga^+ ions bombardment, which physically removes the target atoms [166, 167]. The FIB used in this thesis is Nova 600 NanoLab dual-beam (SEM/FIB) from FEI with an achievable resolution of 5 nm. FIB milling is an alternative way for fabricating nanostructures instead of the liftoff process. The process flow for FIB direct milling of metallic nanohole patterns is shown in Fig. 2.16. In general metallic hole fabrication includes three steps: the target material (Au, Ag or Al) is deposited on a glass substrate with evaporation or sputtering machines, as shown in Fig. 2.16 (Step 1). The sample is tilted at 52° during the milling process such that the high energy Ga^+ beam is aligned perpendicular to the surface of the sample, as seen at Step 2 in Fig. 2.16; while the SEM beam is at 52° toward the sample. The metallic nanohole structures are then revealed as the material is removed in the defined areas. The FIB operates at a voltage of 30 kV and a current of 10 pA during the milling process.

2.3.2 FIB beam expanding problem

The problem that one can encounter during the dual-beam (SEM/FIB) milling process is that the high energy Ga^+ can easily remove material from relatively soft metallic materials, such as Au, Ag, and Al. Furthermore, the beam size of the ion beam is current dependent: for 1

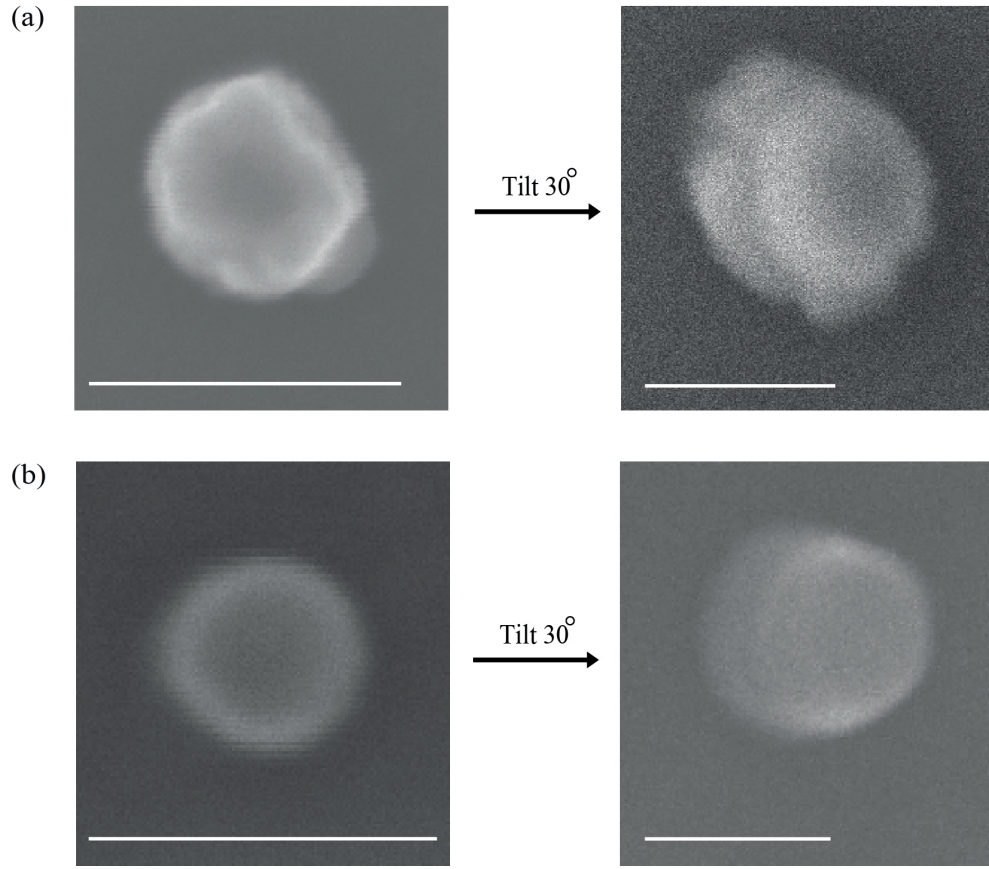


Figure 2.15: Comparison between sandwich cavity antennas fabricated (a) by standard EBL combined with liftoff, leading to an asymmetric structure with slanted sidewalls (scale bar 200 nm); and (b) by IBE etching producing a symmetric structure with well vertical sidewalls (scale bar 100 nm).

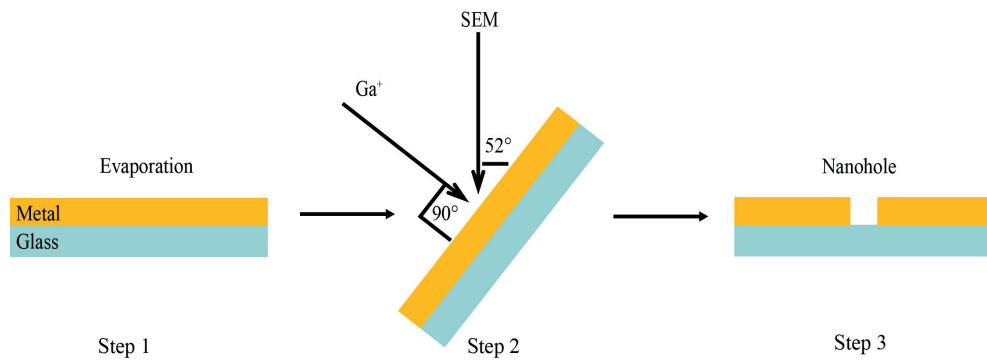


Figure 2.16: Schematic illustration of FIB/SEM direct milling process.

pA the beam diameter is about 7 nm, while for 10 pA the beam size is about 12 nm [168]. Unfortunately, a 1 pA beam is very difficult to adjust during milling, since the signal is very low leading to a poor contrast. This makes the realization of extremely small gaps very difficult

Chapter 2. Advanced plasmonic nanostructures: design, fabrication, and characterization

in metallic materials. A hard mask layer (silicon dioxide SiO_2 or aluminum oxide Al_2O_3) can however overcome this effect. For example, 4-nanoholes structures FIB milled in a 200 nm thick Ag film on a thin glass substrate without and with a SiO_2 hard masklayer (thickness 20 nm) are schematically shown in Fig. 2.17(a) and 2.17(b). This structure represents the complementary structure of the 4-nanorod antenna shown for example in Fig. 2.9(b). Note that the effective gaps are extended from their designed dimension g_1 to g_2 without a hard mask layer, Fig. 2.17(a). On the other hand, the designed gaps keep correct size when there is a mask layer because the expansion effect eventually happens in the mask, Fig. 2.17(b). In Fig. 2.17(c) we observe that without hard mask the 40 nm gaps rarely survive the milling process, while they survive well thanks to the hard mask protection, Fig. 2.17(d).

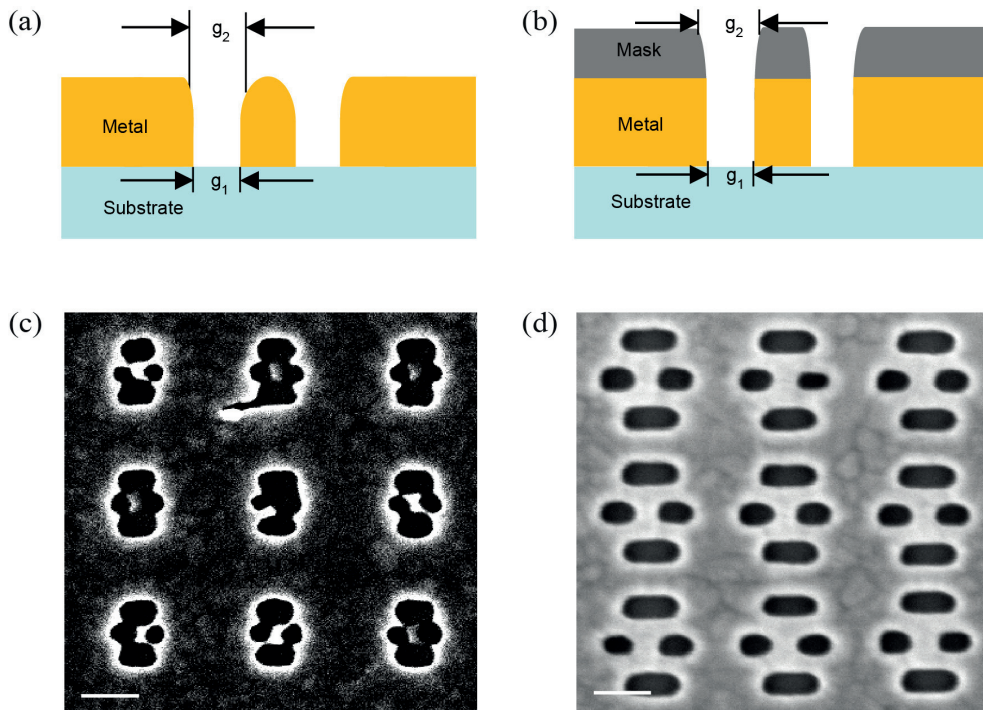


Figure 2.17: Schematic illustration of FIB milling (a) without mask and with mask (b). Comparison of FIB milling nanoholes (c) without mask (scale bar 200 nm) and with mask (d) (scale bar 150 nm).

2.3.3 Sample fabricated with focused ion beam

Metallic nanoholes – often called zero-mode waveguides or negative plasmonic antennas – exhibit extraordinary transmission effects [71], and have been used to detect a single molecule, to enhance fluorescence, second harmonic generation or Raman scattering (SERS), for biosensing or plasmon lasing [65, 72–78, 169–173]. Here I show that FIB can directly mill in Ag different shapes, produce different gaps within regularly arranged nanoholes, Fig. 2.18(a)–(c), or random quasi-crystal nanoholes, Fig. 2.18(d). Of particular interest is the complementary 4-nanohole structure in Fig. 2.18(c) that will be used to study fluorescence enhancement in Chapter 4.

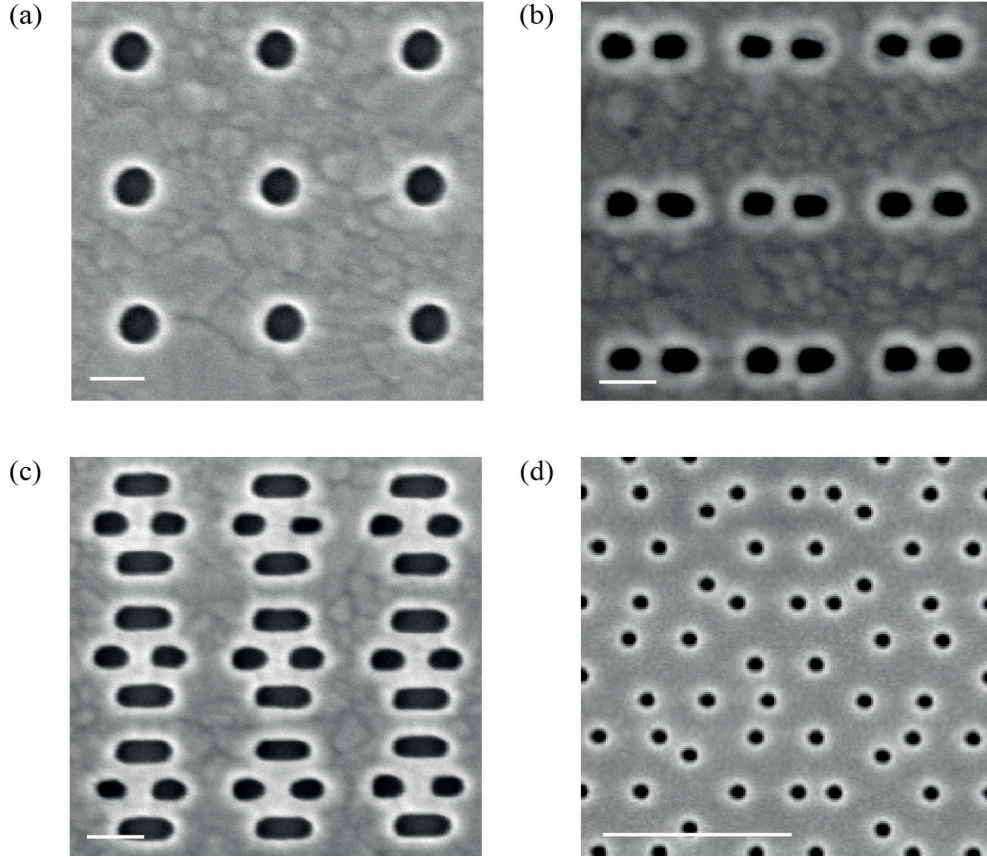


Figure 2.18: Different nanohole geometries fabricated with FIB in silver films: (a) Single circular nanohole array with 400 nm center to center spacing (scale bar 100 nm), (b) dipole hole pairs with a 30 nm gap (scale bar 100 nm), (c) nanohole structure complementary to 4-NRSAs, also called negative antennas (scale bar 100 nm), (d) quasi-crystal nanohole pattern with 80 nm diameter (scale bar 5 μm).

2.4 Characterization tools

The fabricated antennas are characterized according to the properties that are needed to be investigated. In general, a scanning electron microscope (SEM) image is a direct way to check the morphology of the antennas and the resist pattern made by EBL. Atomic force microscope (AFM) is used to estimate the surface roughness of the metal films. The optical properties of the fabricated antennas are characterized using visible range dark and bright field spectroscopies. X-ray photoelectron spectroscopy is used to determine the atomic concentration of different elements including Ag, carbon (C), sulfur (S), Si, and so on.

2.4.1 Scanning electron microscope

The size and shape of the fabricated antennas are the first parameters that should be checked. In general, this can be done with SEM. The field emission Zeiss MERLIN SEM (acceleration

Chapter 2. Advanced plasmonic nanostructures: design, fabrication, and characterization

voltage from 0.02 to 30 kV) in CMI EPFL is used to characterize the fabricated antennas in this thesis.

2.4.2 Atomic force microscope

The atomic force microscope (AFM) (FastScan Bruker GmbH) in tapping mode with a Si tip under ambient conditions is used to measure the root mean square (RMS) roughness of the Ag film.

2.4.3 Dark-field single particle scattering spectroscopy

The scattering spectra are measured with a homemade white light (halogen lamp) illumination and dark-field microscope (Olympus IX-71 with a PLAPON 60x oil immersion 1.45 NA objective). A polarizer (LPVIS050-MP, Thorlabs) is used to set the required polarization. The scattered light is measured with a spectrometer (Shamrock SR-303i, Andor) connected to a CCD camera (iDUS 401BRDD, Andor) for more details please check [174, 175]. The final scattering spectra of the fabricated antennas are obtained using the raw spectra subtracting the background noise and then normalizing to the spectrum of the light source measured for a simple reflection mirror (Thorlabs PF 10-03-P01).

2.4.4 Light transmission and reflection spectroscopy

The spectra (reflection and transmission) of the metallic nanoholes are characterized with a visible white light illumination spectroscopy system based on an inverted optical microscope (Olympus IX-71) coupled to a spectrometer (Jobin Yvon Horiba Triax 550). A halogen white light source is focused onto the sample using an objective (20x, NA = 0.4). The reflected light is collected through the same objective and recorded using a spectrometer. The reflected intensity is normalized by the spectrum of the lamp obtained by reflection measurements with a silver mirror (Thorlabs PF 10-03-P01). The transmission spectra are measured with the same objective. The transmitted light through the nanodisk array was normalized by the transmitted light through a reference glass substrate. A polarizer (LPVIS050-MP, Thorlabs) is used to set linearly polarized light illumination for both reflection and transmission measurements.

2.4.5 Fourier imaging spectroscopy

The emission pattern for different samples is characterized using a Fourier imaging setup that is built from a commercial inverted microscope (Olympus IX73). A supercontinuum light source (Fianium FemtoPower 1060) combined with an 8-channel acousto-optical tunable filter (AOTF) is used to define the illumination conditions and the wavelength of interest. The objective has a high numerical aperture (NA = 1.49, Olympus UAPO N 100x oil immersion). Additional details for this setup are described elsewhere [143, 144].

2.4.6 X-ray photonelectron spectroscopy

The X-ray photoelectron spectroscopy (XPS) measurements for the determination of atomic concentrations for different elements have been performed using a PHI VersaProbe II model from Physical Instruments AG, Germany. The elemental analysis of the Ag film has been performed using a monochromatic Al $K\alpha$ X-ray source with 24.1 W power with a beam size of 100 μm and the binding energy is calibrated with C 1s value at 187.85 eV. The depth profile is measured by recording the XPS spectrum of the top surface and subsequent Ar^+ (2keV) ion beam sputtering. The atomic concentrations for Ag, Si, C, O, and S are calculated from the integrated intensity of the Ag 3d, Si 2p, C 1s, O 1s, S 2p peaks for each depth.

2.5 Confocal fluorescence lifetime spectroscopy

The different characterization tools described in the previous section were readily available at the beginning of my PhD. To investigate the interaction between fluorescent molecules and plasmonic nanostructures, I have also built a dark-field confocal setup for fluorescence lifetime spectroscopy as will be used in Chapters 4 and 5, Fig. 2.19. The light source includes a white light source (halogen lamp) and a diode pulsed laser. The white light is used as source for the dark-field microscope to distinguish and position individual antennas. The scattered light from the antenna is collected and imaged by a CCD camera. The antenna pattern (marked in the green box) and the focused laser spot (marked in the red box) are shown on the left side in Fig. 2.19. The diode laser has an emission peak at the wavelength $\lambda = 640 \text{ nm}$, a bandwidth of $\delta\lambda = 2 \text{ nm}$, a pulse duration of 50 ns and a repetition rate of 10 MHz. This laser is used to excite the molecular-plasmonic systems with an optimized power of 1 μW (the fluorescence signal at this power is stable). The fluorescence image measurements are performed through sample scanning using a motorized piezo stage. The sample is mapped by a line scanning first to obtain the fluorescence image (fluorescence collected by a PLAPON 60x oil immersion 1.45 NA objective). Then one individual antenna is selected for the fluorescence decay measurement using the time-correlated single-photon counting (TCSPC) technique (PicoHarp 300, PicoQuant GmbH). The whole system (including the motorized piezo stage, TCSPC counter, laser) is controlled by the software SymphoTime 64. The illumination laser is deflected by the dichroic beam splitter (ZT647rdc) and the fluorescence light is guided through a 50 μm pinhole (Thorlabs P50S - $\varnothing 1$) and focused on the single photon avalanche photodiode (SPAD, MPD). The excitation laser is filtered out with a notch filter (NF03-642E-25). The single photon signal is registered with the TCSPC technique and the decay curve is fitted by deconvoluting with the SymPhoTime 64 software the instrument response function (IRF, which is 0.08 ns, that characterizes the time resolution of the system) to estimate the lifetime of the molecule.

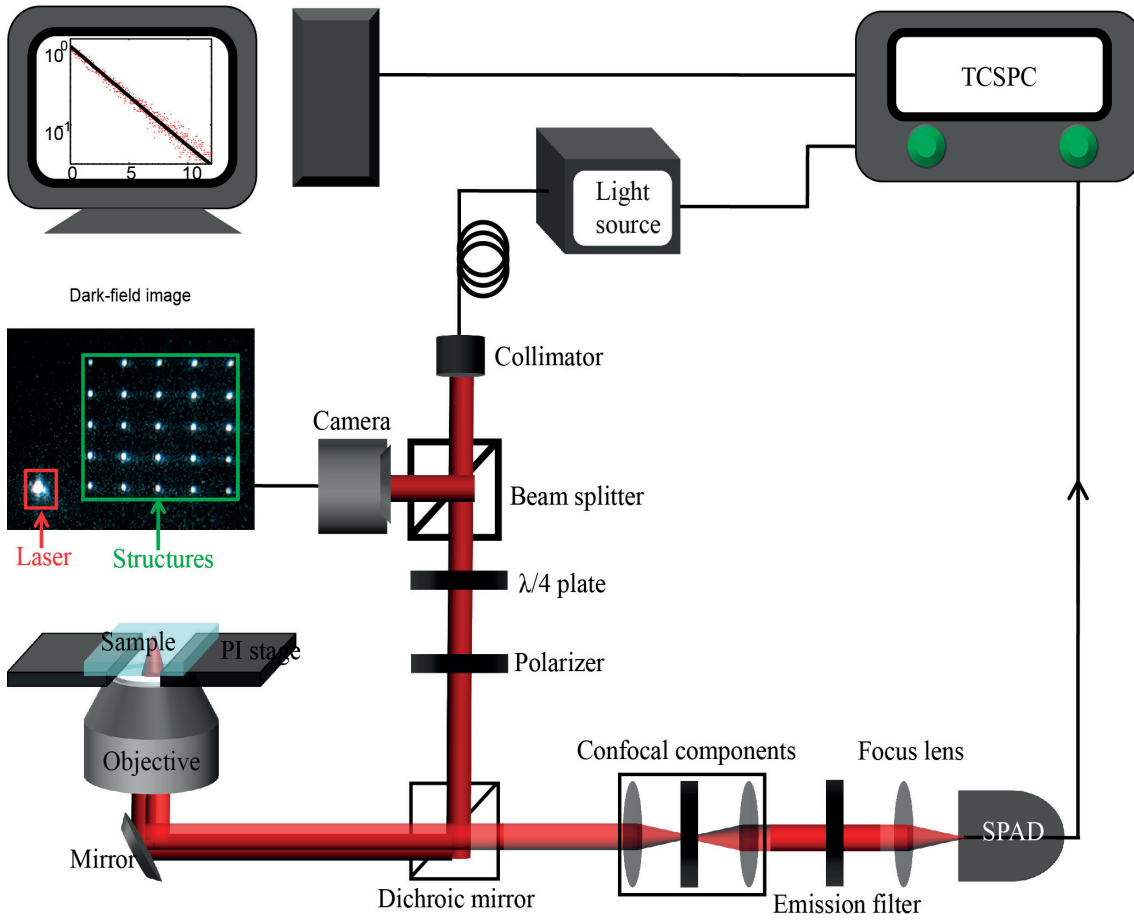


Figure 2.19: Dark-field confocal fluorescence spectroscopy setup.

2.6 Summary

This chapter has described the different techniques used in this thesis, from numerical simulations using the SIE technique to different nanofabrication approaches based either on EBL (with positive or negative resists) or FIB. Beyond the details of each fabrication technique, the main message of this chapter is probably that pushing nanofabrication down to features in the 10 nm range is not a straightforward task and, depending on the geometry of interest, one approach might be better suited than another one and there does not exist one unique process to fabricate the different structures investigated in this thesis. For example, the double-layer positive PMMA resist liftoff process is very well suited to fabricate individual antennas, metasurfaces, and large antenna arrays. IBE etching with HSQ as hard mask is very appropriate to fabricate metal-dielectric-metal nanostructures and produces better results than a liftoff process. There are many parameters that can influence the final result and we have seen that even the dimensions of the substrate need to be adapted to the different technological steps. For example thermal stability of the substrate, leading to uneven surfaces can cause major

disruption to the e-beam writing process. These problems can however be fixed by using small size chips (e.g., 20 mm \times 20 mm). Proximity correction is required to limit linewidth broadening and can be optimized by tuning the dose with the help of Layout BEAMER. Single point exposure with large current 200 nA can overcome proximity problems for the fabrication of large arrays with a small period. I have demonstrated alignment of nanostructures fabricated in successive EBL steps with a positioning accuracy as high as 10 nm, thanks to appropriate multilevel alignment mark strategies, as well as the benefit that proceeds from using a hard mask layer for the fabrication of small features using FIB milling. Finally, the different characterization techniques used throughout this work have been described to some extent. They include optical imaging and spectroscopic techniques, as well as techniques that resort to electron beams. Finally, the dark-field confocal fluorescence setup developed for fluorescence measurement is explained in detail.

3 Plasmonic silver nanostructures and film

In this chapter, I unveil the degradation mechanisms of Ag plasmonic nanostructures and I introduce an original method to overcome these mechanisms and produce Ag nanostructures with a stable morphology for several months. Part of the material presented in this chapter has been submitted for publication [176].

3.1 Introduction

In Chapter 2 I have shown the fabrication of plasmonic antennas with different noble metallic materials, such as Au, Ag, and Al; I will focus on Ag in this chapter. My motivation for studying Ag as a plasmonic material is motivated by two aspects. On the one hand, Ag always shows lower losses than Au for the wavelength range between 400 nm and 2000 nm, as indicated by the imaginary part of the permittivity in Fig. 3.1(b). As a result, the quality factor (Q_{LSPR} and Q_{SPP}) of the plasmonic resonators made of Ag are much better than the ones made of Au or Al, see Fig. 3.1(c)-(d). On the other hand, although Ag is a very good plasmonic material, it has unfortunately no long-term stability, which is observed in the evolution of the morphologies between fresh Ag antennas, Fig. 3.2(a), and similar structures after 4 days, Fig. 3.2(b). In comparison, one does not notice any evolution for the morphology of Au antennas, even over a 3 months period, compare Fig. 3.2(c) and (d). This is why Au is a much more popular plasmonic material than Ag, although it has higher losses than Ag. In this chapter, I wish to investigate the deterioration mechanisms for Ag and develop a method to produce stable Ag nanostructures.

Together with lower losses, Ag also provides a stronger field enhancement at the vicinity of plasmonic nanostructures and holds the promise of extending – together with Al – the spectral range where plasmonics can be used for many applications varying from solar cell to color imaging based on plasmonics [60, 177–184]. Au remains, however the most popular plasmonic material due to its superior chemical and thermal stability compared to other materials [185–187]. Indeed, Ag is prone to degradation, which represents a significant drawback for long-term utilization. The deterioration of Ag is a well-known phenomenon that

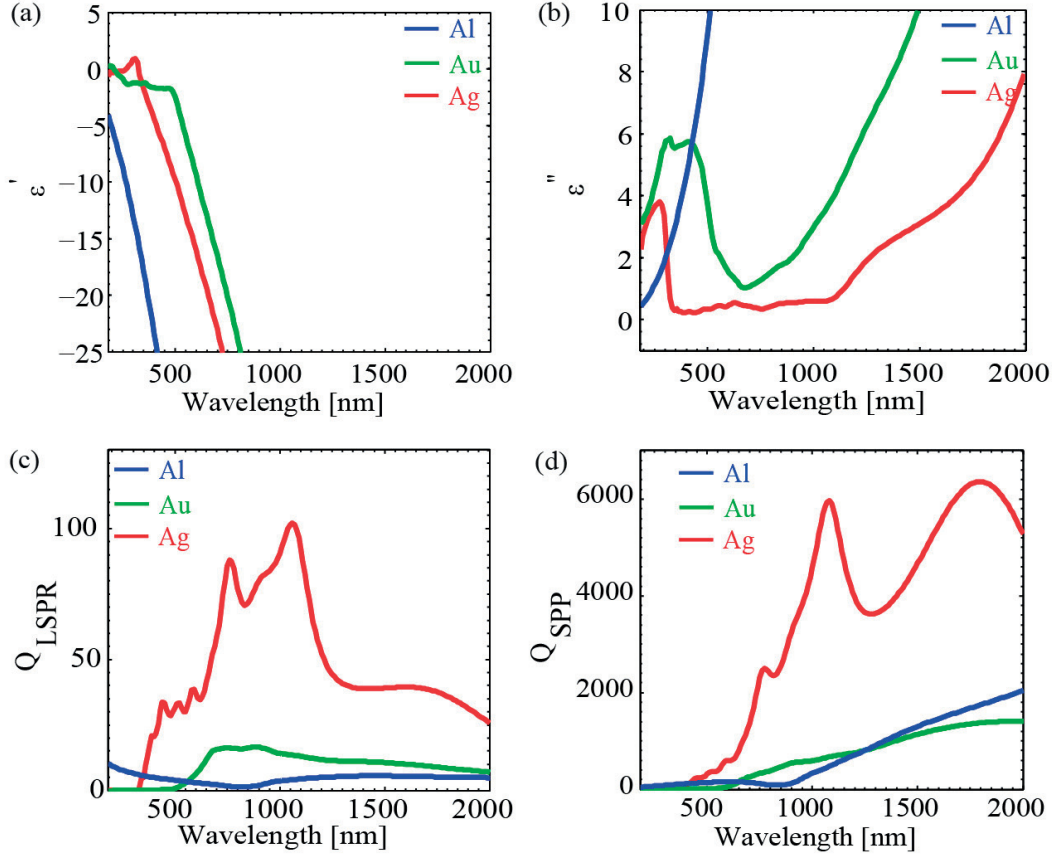


Figure 3.1: Comparison of the permittivity and quality factor for different plasmonic metals (data from [59, 85]). (a) Real part of the permittivity of Al, Ag, and Au. (b) Imaginary part of the permittivity of Al, Ag, and Au. (c) Quality factor for the localized surface plasmon resonance of a spherical particle. (d) Quality factor for propagating the surface plasmon polariton.

was intensively investigated a few decades ago [188–193]. It was shown that Ag nanoparticles (AgNPs) can be rapidly tarnished with a plasmonic resonance shift of 1.8 nm/h due to sulfur (S) contamination (sulfidation) in ambient laboratory air [194–196]. The role played by oxidation instead of sulfidation for Ag nanoparticles deterioration under normal ambient conditions was also evidenced [197–200]. Furthermore, it has been shown that both sulfidation and oxidation require water to take place [201, 202]. To slow down the chemical deterioration of AgNPs, protective coating layers, including graphene, silicon dioxide, and organic thiol molecules were proposed [180, 203–205]. Furthermore, Ag thin films and nanoparticles are thermally unstable at elevated temperatures – even far below the melting point, such as the temperatures used for photoresist baking sequences – and, as a consequence, Ag nanostructures lose their specific plasmonic properties during those processes. The specific environment and substrate also determine this thermal stability [206–210]. Aluminum doping and Ni and Ag(Al) alloying of Ag films also increase the thermal stability of Ag [211, 212]. To improve roughness of an

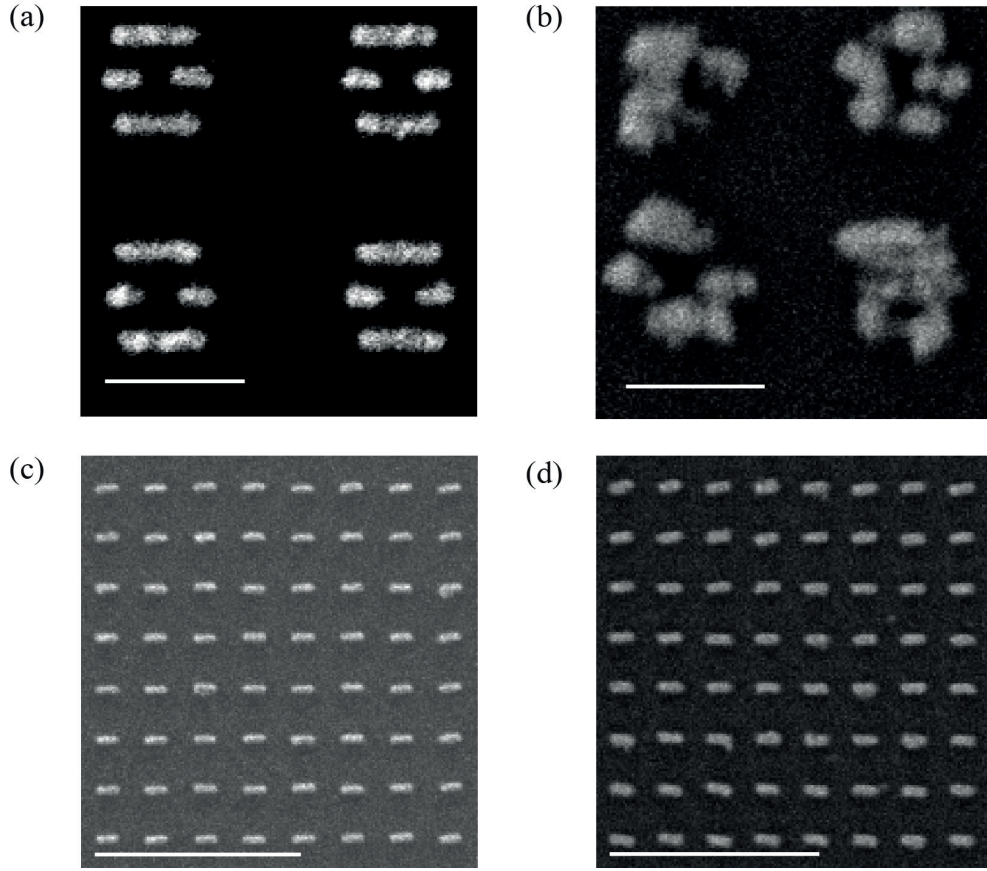


Figure 3.2: (a) Freshly fabricated Ag antenna and (b) the same after 4 days (scale bars 200 nm). (c) Freshly fabricated Au antennas and (d) the same after 3 months (scale bars $1\mu\text{m}$).

Ag film, different seed layers, aluminum doping and template stripping methods have been developed [213–219]. However, adhesion and seed layers increase the damping of a plasmonic system and, consequently, broaden the linewidth of the plasmon resonance [125, 131]. Unfortunately, all these workarounds alter the optical properties of the nanostructures and, consequently, designs have to be adjusted in order to maintain the desired properties. An efficient stabilization scheme that would enable the routine utilization of silver nanostructures is therefore missing.

In this chapter, we demonstrate such a stabilization scheme and first show that oxygen (O_2) only does not deteriorate Ag nanostructures since Ag nanostructures exposed to pure O_2 maintain their optical and morphological properties. Then using x-ray photoelectron spectroscopy (XPS) technique to show that the concentration of sulfur in ambient air is far too low for a significant alteration of Ag nanostructures. we conclude that relative humidity (RH), namely adsorbed water, plays a key role in Ag degradation and we finally develop a dehydration process that dramatically improves the chemical and thermal stability of plasmonic Ag nanostructures and thin films.

3.2 Deterioration of silver nanostructures over short period of time

Figure 3.3 shows fresh 4-nanorod Ag antennas (4-NRSAs) fabricated using EBL with the subsequent thermal evaporation of Ag film and liftoff process described in last chapter. A single 4-NRSA consists of two long rods (length 130 nm) surrounding two short rods (length 68 nm). Width and height are 40 nm for all elements and the gaps between the rods are 30 nm. The Fano resonance dip is located at $\lambda = 640$ nm. The 4-NRSA structure is chosen because of its strong Fano resonance, which is very sensitive to the shape of the nanostructure [220]. A gradual deterioration of the 4-NRSAs upon exposure to ambient conditions is clearly visible in Fig. 3.3. Their morphology, examined using SEM and their optical properties, measured by dark-field scattering spectra (DFSS) are completely changed over that short period of time.

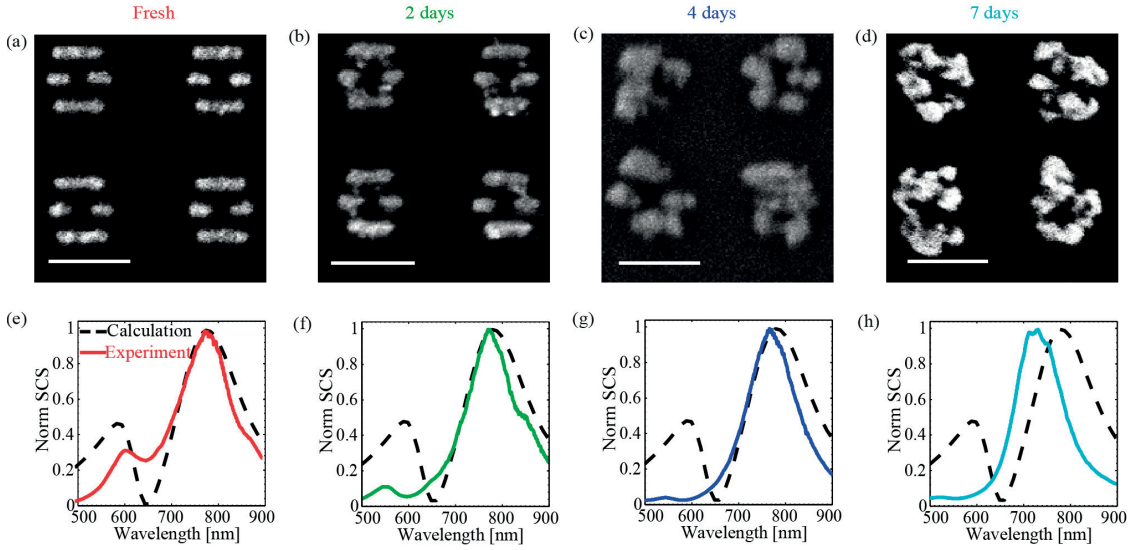


Figure 3.3: Ag nanostructure degradation over short period of time. (a) SEM image of the fabricated fresh 4-NRSAs. SEM images of the fabricated 4-NRSAs under ambient condition after (b) 2 days, (c) 4 days and (d) 7 days. (e) - (h) Scattering spectra measured with dark-field spectroscopy corresponding to the SEM images (a), (b), (c) and (d). The dashed black curve represents the calculated scattering spectrum for the designed 4-NRSA. The scale bars in (a), (b), (c) and (d) are 200 nm.

The fresh 4-NRSAs, as shown in Fig. 3.3(a), have good morphologies and their DFSS (red curve in Fig. 3.3(e)) agrees very well with the calculations (dashed lines in Fig. 3.3(e), 3.3(f), 3.3(g) and 3.3(h)) using the SIE method as described in the last chapter. The spectra exhibit a typical asymmetric Fano lineshape with a dip at the wavelength of $\lambda = 640$ nm (calculations) and $\lambda = 645 \pm 5$ nm (measurements). After exposure to ambient conditions for two days, the corresponding DFSS (green curve in Fig. 3.3(f)) is blue shifted with respect to the original resonance (Fig. 3.3(e) red curve) and the Fano dip becomes less significant but is still clearly visible. After a four days storage period in ambient conditions, the morphology of the 4-NRSAs becomes quite fuzzy (Fig. 3.3(c)) and the spectrum is further blue-shifted (Fig. 3.3(g)). After 7 days, the original nanostructure morphology is completely lost (Fig. 3.3(d)) and the Fano dip

vanishes entirely (Fig. 3.3(h)).

3.3 Deterioration mechanism of Ag nanostructures and films

3.3.1 Oxygen or sulfur

The fact that O₂ causes Ag oxidation and eventually destroys Ag nanostructures is a widespread paradigm that is also supported by the literature [200]. To determine the exact role of O₂ in the deterioration mechanisms of Ag, two samples with 4-NRSAs on a glass substrate were fabricated and stored separately for two weeks in two different environments, O₂ and argon (Ar) – an inert gas in which Ag nanostructures should not be altered. For reasons that will become obvious later, these experiments were performed under almost zero relative humidity. Fig. 3.4(a) and Fig. 3.4(b) show a comparison of the corresponding morphologies of the 4-NRSAs stored under O₂ and Ar environments and Fig. 3.4(d) and Fig. 3.4(e) display the corresponding DFSS. Quite surprisingly, the morphology of the two 4-NRSAs does not show any changes over this relatively long time period, as was the case for the nanostructures exposed to ambient air reported in Fig. 3.3(b). The dip position in the asymmetric Fano lineshape remains at $\lambda = 645 \pm 5$ nm (red and green curves in Fig. 3.4(d) and Fig. 3.4(e)) and is still in good agreement with the calculations (dashed black curve). These observations indicate that O₂ alone does not deteriorate the Ag nanostructures.

It has been proposed that atmospheric sulfur present in the air could produce Ag sulfidation and tarnish Ag nanostructures, leading to a resonance shift of 1.8nm/h [195]. However, even in rural areas, the total concentration of atmospheric sulfur compounds is as low as a few ppb [221]. To clarify the effect of S, I stored a 40 nm thick Ag film under ambient conditions in the laboratory for two months and did not observe any degradation due to sulfidation, Fig. 3.4(c). The subsequent XPS analysis of this film, shown in Fig. 3.4(f), indicates that the atomic concentration of S (blue curve in Fig. 3.4(f)) is extremely low, close zero. I, therefore, conclude that sulfidation is not key to the deterioration of Ag, at least in laboratory conditions.

Since O₂ alone does not seem to deteriorate AgNPs, the influence of other parameters needs to be considered. Actually, it has been shown that both sulfidation and oxidation require water to take place [201, 202]. Ion release from AgNPs in an aqueous environment is also known and has been studied in an ecotoxicological context [215, 222]. Finally, in a previous paper Krishnan, et al have shown that water present during the evaporation significantly deteriorates the quality of nanoantenna made of Al [135]. For these reasons, I address here the role of water in the deterioration of Ag nanostructures and perform experiments under two different relative humidity (RH) conditions under Ar atmosphere. To this end, two 4-NRSAs samples on a glass substrate were stored in recipients with low (almost 0%) and 100% RH for two weeks. For the low and high RH experiments the glass recipients were dehydrated at 200 °C for 1 h and then stored in a dry Ar environment before the samples were introduced and the recipients subsequently sealed. In the high RH experiment, a vial filled with water was

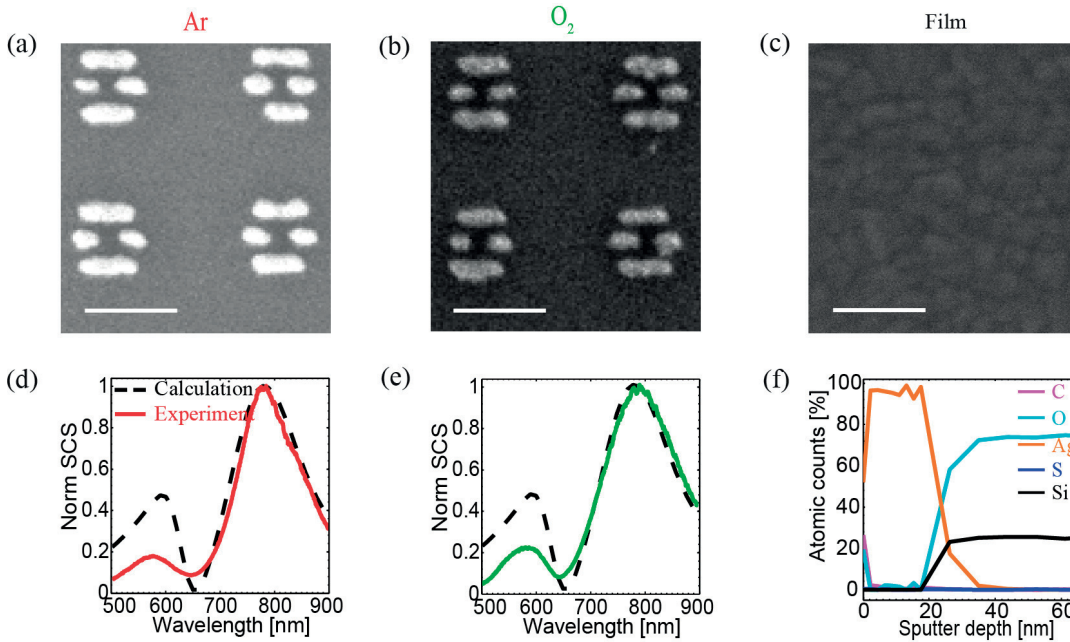


Figure 3.4: Mechanism of Ag nanostructure degradation. Morphology and optical properties of 4-NRSAs exposed to Ar and O₂. (a) SEM of the 4-NRSAs exposed to Ar. (b) SEM of the 4-NRSAs exposed to O₂. (d) - (e) DFSS corresponding to (a) and (b). The dashed black represents the scattering spectrum of 4-NRSA calculated with SIE. (c) SEM of Ag film stored in ambient air for two months. (f) XPS analysis of specific elements in the Ag film shown in (c); the atomic concentration of different elements are represented by the following colors: Ag: orange; O: cyan; Si: black, carbon (C): pink and S: dark blue. The scale bars in (a), (b) and (c) are 200 nm.

additionally introduced into the recipient prior to sealing. The results are shown in Fig. 3.5.

3.3.2 Surface adsorbed water

Figures 3.5(a) and 3.5(b) show the morphologies of the 4-NRSAs exposed to two different RH. Quite surprisingly, the 4-NRSAs survive under low RH while they are completely ruined and lose their shape under 100% RH. The asymmetric Fano lineshape obtained by DFSS maintains its dip at $\lambda = 635 \pm 5$ nm (Fig. 3.5(c)) for low RH, still in good agreement with the calculation (dashed black curve). On the other hand, the DFSS completely loses its asymmetric Fano lineshape when the 4-NRSAs are stored at 100% RH under Ar atmosphere. These results clearly demonstrate that humidity or adsorbed water is absolutely indispensable for the deterioration of Ag nanostructures.

The formation of small nanoparticles scattered around the main body of the 4-NRSA and forming a near circular shape (Fig. 3.5(b)) is caused by the surface migration of ionic Ag in adsorbed water [202, 223]. Keast et al. reported that the small particles arising from the parent particles consist of Ag₂S and are formed by the dominating process of sulfidation [223]. Since in the previous experiment, no S was detected, such a mechanism can be excluded here.

3.3. Deterioration mechanism of Ag nanostructures and films

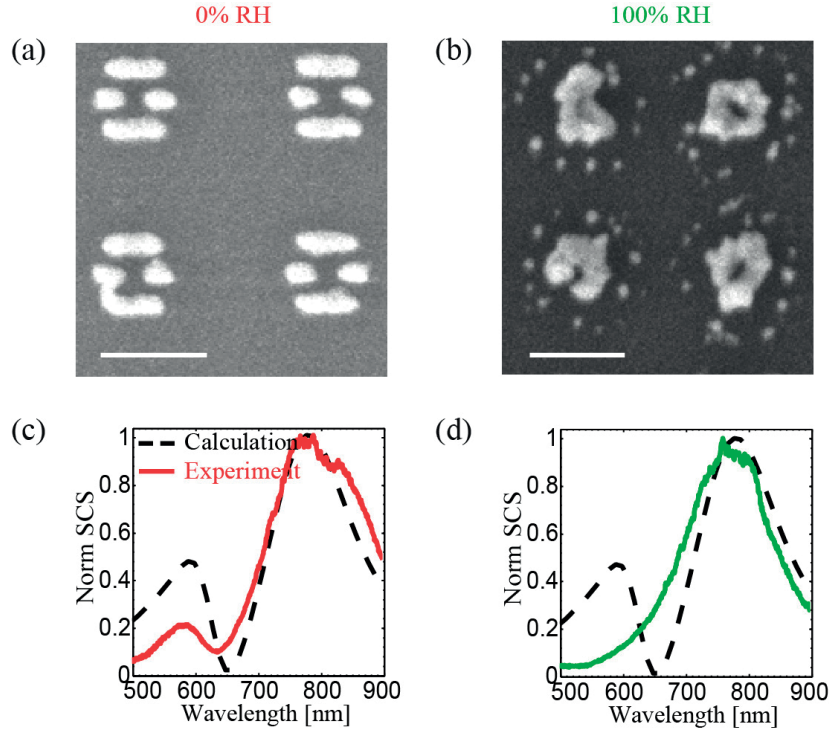
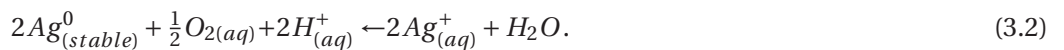


Figure 3.5: Humidity is the reason for Ag nanostructure degradation. Morphology and optical properties of 4-NRSAs exposed for two weeks to (a), (c) 0% (b), (d) 100% RH. (a), (b) SEM images and (c), (d) corresponding DFSS (the dashed black curve represents the scattering spectrum of the 4-NRSA calculated with SIE). The scale bars in (a), (b) are 200 nm.

Measurements of adsorbed water using attenuated total reflection (ATR) infrared spectroscopy have revealed the existence of 3 RH-dependent regimes of adsorbed water [224]. At low, intermediate, respectively high RH, well-ordered ice-like, quasi liquid, respectively liquid configurations are formed. It has been proposed that metallic Ag^0 can be oxidized to Ag^+ in the presence of dissolved O_2 and water according to the following reaction [225]:



Dissolution of metal into ionic Ag enables migration in the adsorbed liquid water layer, which explains the degradation of the Ag nanostructures at high RH and the formation of satellites around its main body, as shown in Fig. 3.5(b). On the other hand, at low RH the reverse reaction of (1), reaction (2) prevails, which reduces ionic Ag into a more stable configuration and suppresses migration efficiently:



Motivated by these observations, I have developed the dehydration process described in the next section to prevent the deterioration of Ag nanostructures.

3.4 Improvement of long-term, chemical, and thermal stability, and surface roughness

3.4.1 Chemically stabilize Ag nanostructures

Since humidity appears to play a major role in the deterioration of Ag nanostructures, I have developed a dehydration process that stabilizes the 4-NRSAs over a long period of time (14 weeks). I again fabricated 4-NRSAs on glass substrate as shown in Fig. 3.6(a). The morphology of fresh 4-NRSAs and the corresponding DFSS are displayed in Fig. 3.6(a) and Fig. 3.6(c). The 4-NRSAs were then stored in a chamber (DRY KEEPER Sato Keiryoki MFG CO. LTD) and continuously purged with dry Ar gas (at 20 ° 1.013 Pa pressure and 5 nL/min for 3 weeks) to remove adsorbed water from the surface of the 4-NRSAs. After that, the sample was removed from the chamber and stored under ambient condition at a RH of $45 \pm 2\%$ (measured with HYGROLOG-HL-NT3 monitor). The morphology and optical properties of the nanostructures were monitored every 2 weeks up to 14 weeks. Fig. 3.6 shows SEM images of 14 weeks with corresponding DFSS (the full information on morphology and optical properties up to 14 weeks is provided in Fig. B.1). From Fig. 3.6(a) and Fig. 3.6(b) it can be seen that, following the dehydration process, the morphology of 4-NRSAs did not change significantly, although the samples were stored under ambient condition. Furthermore, the corresponding DFSS still maintain their asymmetric Fano lineshape as shown in Fig. 3.6(c) and Fig. 3.6(d). These results clearly demonstrate the improved stability for the Ag nanostructures, also under ambient conditions.

3.4.2 Thermally stabilize Ag nanostructures

As demonstrated and in agreement with literature [202, 223] humidity or, better, adsorbed water - induces spontaneous Ag^+ migration and the non-dehydrated Ag nanostructures lose rapidly their original shape at temperatures well below the melting point (see Fig. 3.7(b)), at for example 180 °C, which is the pre and post photoresist baking temperature for standard EBL process. Although the melting point for bulk Ag is 893 °C [226] the non-dehydrated 4-NRSAs already lose their shape after five minutes baking on a hot plate in air at 180 °C, Fig. 3.7(b). Consequently, the asymmetric Fano resonance is also modified by the baking process, as can be seen when comparing Fig. 3.7(d) and Fig. 3.7(e). On the other hand, both the morphology and the DFSS of the dehydrated 4-NRSAs remain good after the baking process, Fig. 3.7(c) and Fig. 3.7(f). I conclude that during the dehydration process the Ag morphology is changed through reactions (1) and (2) from an unstable to a more stable morphology which is also indicated by the AFM measurements in Fig. 3.8. The deposition process leaves the silver in an unstable morphology. From this morphology, under ambient conditions, the silver nanostructures can easily deteriorate. Under a dry Ar environment, adsorbed H_2O is significantly reduced, Ag^+ migration efficiently suppressed and, according to reaction (2), the silver is transformed into a more stable morphology.

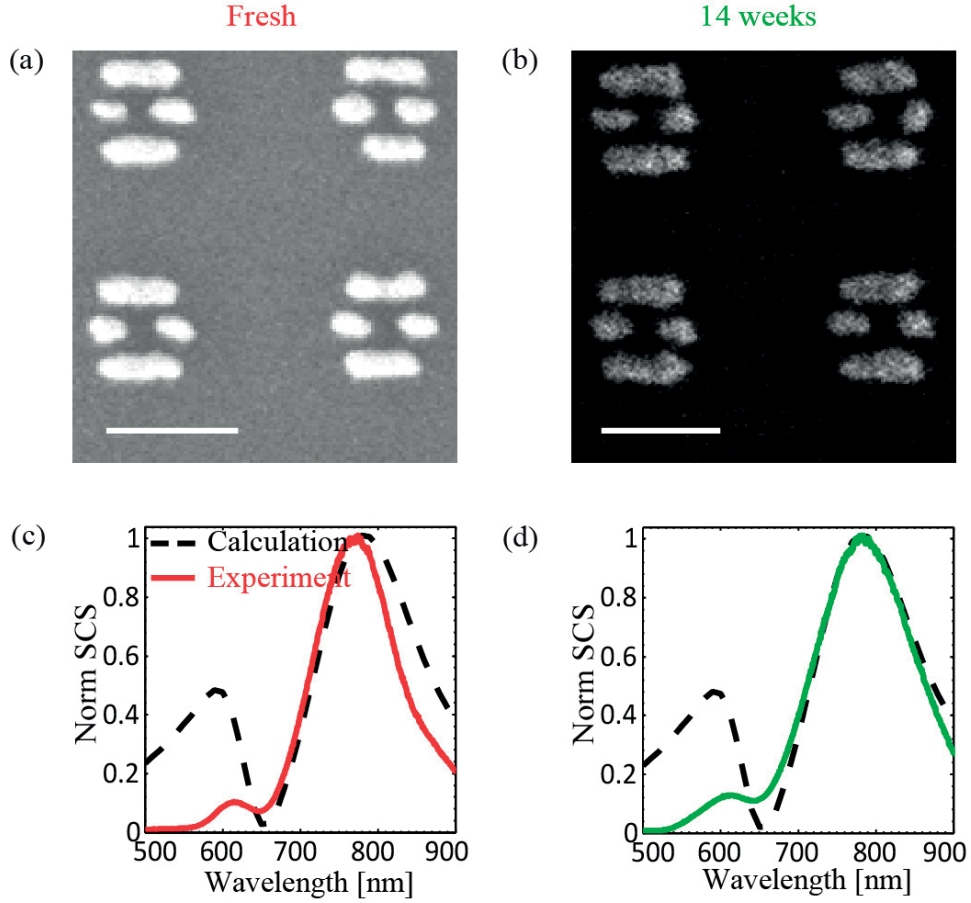


Figure 3.6: Dehydration makes stable Ag nanostructures. Temporal tracking of morphology and optical properties of the 4-NRSA over a long period of time (14 weeks). (a) SEM image of the freshly fabricated 4-NRSA. (b) SEM image of the dehydrated 4-NRSA after 14 weeks stored under ambient condition. (c) - (d) DFSS corresponding to (a) and (b). The dashed black curve corresponds to the scattering spectrum of the 4-NRSA calculated with SIE. The scale bars in (a) and (b) are 200 nm.

3.4.3 Improvement of the surface roughness of Ag films

Like their nanostructure counterparts, thin Ag films have also a poor thermal stability [206–209, 227]. To investigate the thermal stability of Ag films at elevated temperature (180 °C, far below the melting point though), 40 nm thick Ag films were thermally evaporated on glass substrates. Fig. 3.8(a) shows a typical SEM micrograph of such a thin film. The first sample was baked 5 minutes on a hot plate at 180 °C in air. After such a treatment the film became discontinuous and islands were formed (Fig. 3.8(b)). The other sample was first dehydrated as described previously (Fig. 3.8(c)) and then baked 5 minutes on a hot plate at 180 °C in air (Fig. 3.8(d)). Comparing with the non-dehydrated sample reveals a very significant improvement of the film thermal stability (compare Fig. 3.8(b) and 3.8(d)). AFM measurements were performed for these samples and the results are shown in Fig. 3.8(e), 3.8(f), 3.8(d) and 3.8(h). Fig. 3.8(i),

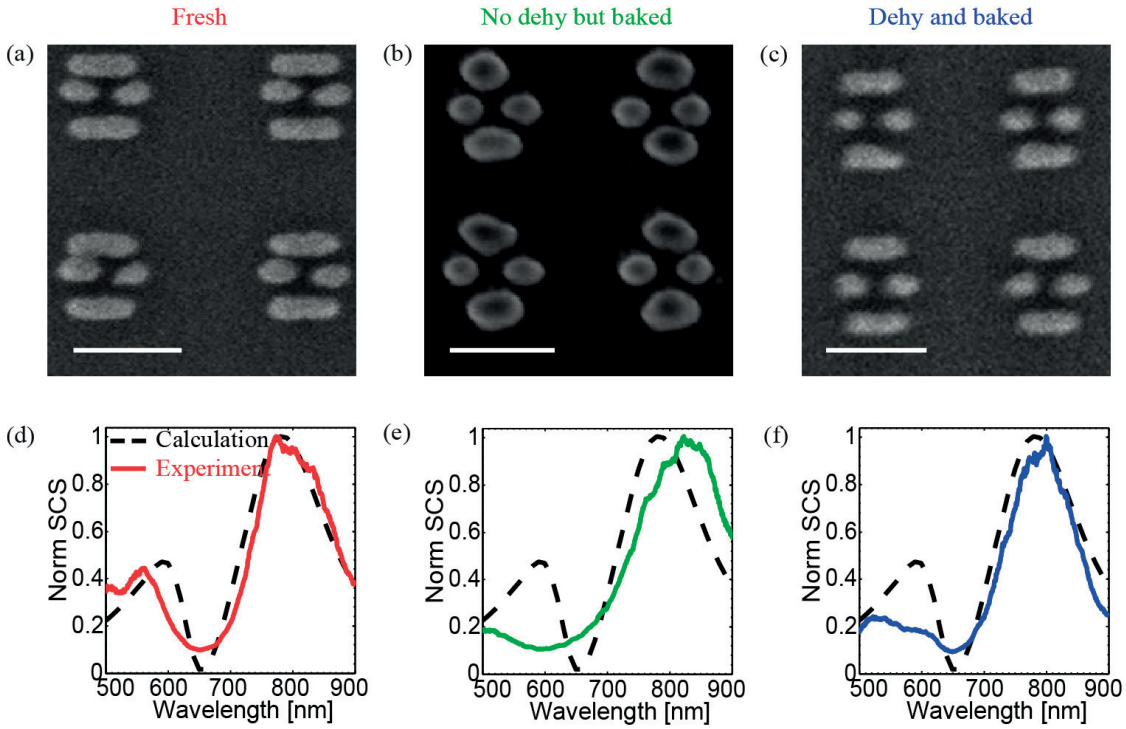


Figure 3.7: Dehydration make thermal stable Ag nanostructures. Morphology and optical properties of baked 4-NRSA with and without previous dehydration process. (a) SEM image of freshly fabricated fresh 4-NRSA. (b) SEM image of 4-NRSA baked without previous dehydration. (c) SEM image of the 4-NRSA baked after dehydration. (d) - (f) DFSS corresponding to (a), (b) and (c). The dashed black curve is the scattering spectrum of the 4-NRSA calculated with SIE. The scale bars in (a), (b) and (c) are 200 nm.

3.8(j), 3.8(k) and 3.8(l) show the peak-to-valley height (PTVH) profile in the center of the films marked by the black line in Fig. 3.8(e), 3.8(f), 3.8(g) and 3.8(h).

The PTVH amplitude for the fresh film is larger than for the dehydrated film, compare Fig. 3.8(i) and Fig. 3.8(k). The PTVH amplitude for the dehydrated then baked film remains smaller than for the fresh one, compare Fig. 3.8(l) and Fig. 3.8(i). Calculating the surface roughness root mean square (RMS) of all the films, I observe that for a non-dehydrated film the RMS is increased from 29.9 nm to 40.4 nm during the baking process (Fig. 3.8(e) and Fig. 3.8(f)). After dehydration, the RMS decreases from 29.9 nm to 2.8 nm (Figure 3.8(e) and 3.8(g)) and then slightly increases to 6.6 nm after baking (Fig. 3.8(h)). This is a further indication that dehydration leads to a reorganization of the thin Ag films according to reactions (1,2) and results in a more stable configuration for thin Ag films.

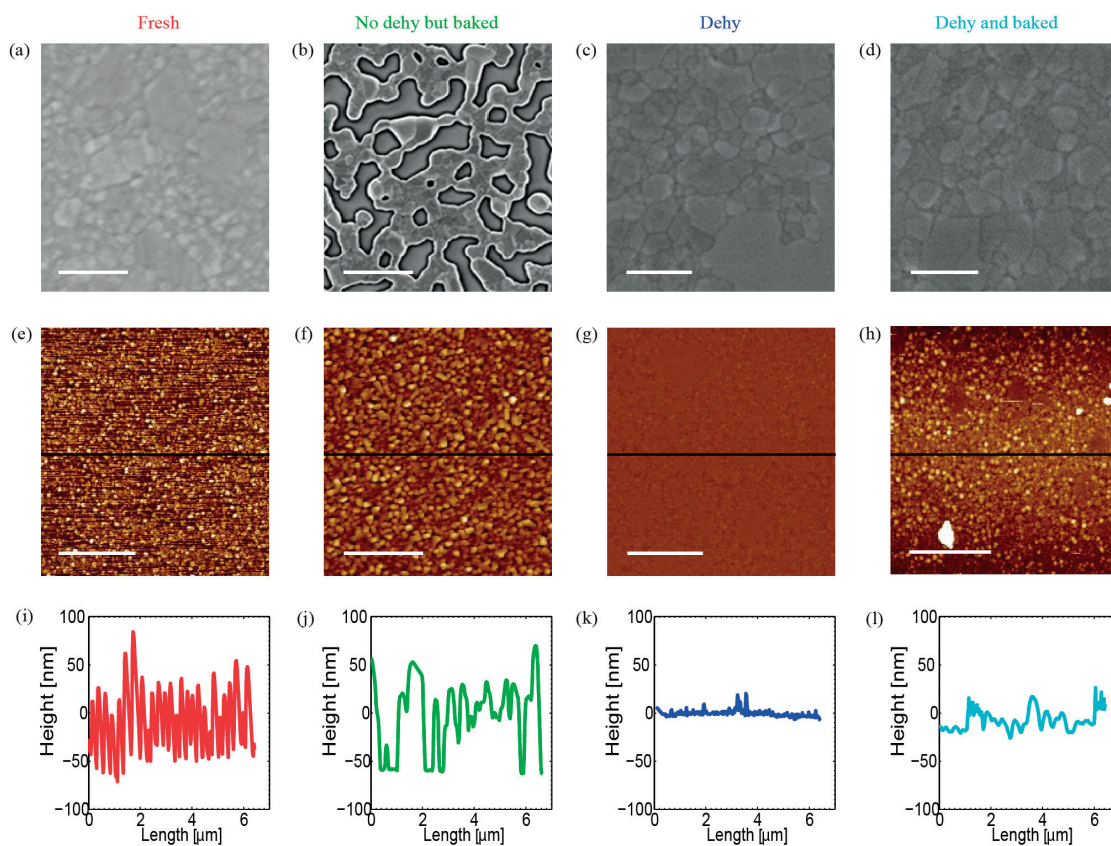


Figure 3.8: Dehydration improves the surface roughness of Ag film. Morphology of baked films with and without dehydration. SEM images of Ag films (a) freshly deposited and (b) after baking, without dehydration. SEM images of Ag film (c) after dehydration and (d) after subsequent baking. (e) - (h) AFM images of the deposited Ag films corresponding to the SEM images (a), (b), (c) and (d). (i) - (l) Corresponding peak-to-valley height profiles along the black lines marked in the AFM images (e), (f), (g) and (h). The scale bars in (a), (b), (c) and (d) are 200 nm and the scale bars in (e), (f), (g) and (h) are 2 μm .

3.5 Summary

In this chapter, it has been evidenced that the deterioration of Ag nanostructures and films is closely linked to the presence of surface-adsorbed water. The chemical and thermal stability of Ag nanostructures and thin films can be strongly enhanced by a dehydration process using a constant Ar flow. This dehydration dramatically reduces the migration process (with water as a catalyst) of ionic Ag, which is essentially responsible for the deterioration of Ag. The dehydrated 4-NRSAs were morphologically and optically stable for 14 weeks. After dehydration, both 4-NRSAs and films survive baking processes at 180 °C. Furthermore, the surface root mean square RMS roughness of Ag film was improved from 29.9 nm to 2.8 nm after dehydration. This study paves the way for the fabrication of Ag nanostructures and thin films that are chemically and thermally stable under ambient conditions for a broad range of applications, including in the short wavelength and near UV ranges of the spectrum.

4 Engineering fluorescence with negative and sandwich nanoantennas

In this chapter, I study fluorescence experimentally using two different types of nanoantennas with dimensions around $100 \times 100 \text{ nm}^2$: negative antennas, as illustrated in Fig. 2.18, and sandwich cavity antennas, as illustrated in Fig. 2.15. The negative antennas made by FIB in a metal film naturally provide a good signal-to-noise ratio since they suppress the incoming light thanks to the screen film. Simultaneously the near-field is enhanced by localized surface plasmon resonances in the apertures. The emitters can be spin coated directly onto the plasmon hot spots rather than requiring a complicated surface functionalization technique. All these properties make negative antennas a good candidate for studying molecular plasmons. In the second part of this chapter, I introduce sandwich cavity antennas with a diameter in the order of 100 nm, to confine molecules right in the middle of the cavity. Surface functionalization is used to immobilize the molecules inside the cavity where the near-field is enhanced.

4.1 Introduction

Molecular plasmons is a very broad topic describing the interaction between molecules and plasmon nanostructures, which results in very interesting fundamental physics [42, 228–232], as well as into potential applications, such as biosensing [233–239], Raman spectroscopy [23, 47, 174, 240–243], fluorescence control [239, 244], as well as nanolasers [76, 245] and single photon sources [139, 246, 247]. The physical description of the interaction between a molecule and a plasmon nanostructures is schematically illustrated in Fig. 4.1(a).

The molecules are distributed in the vicinity of a plasmon nanostructure and the whole system is excited with a focused laser beam, Fig. 4.1(a). The fluorescence is collected with the same objective. By tuning the plasmon resonance to the absorption band or the emission band of the molecules, the emitted fluorescence signal can be modified, Fig. 4.1(b). The transition dynamics of the molecular plasmonic system is described with the Jablonski diagram [248] in Fig. 4.1(c). Both the absorption rate and emission rate of the molecule will be modified by the near-field enhancement and the additional decay channel induced by the plasmonic nanostructure [74, 249, 250]. Essentially, the fluorescence decay modified by

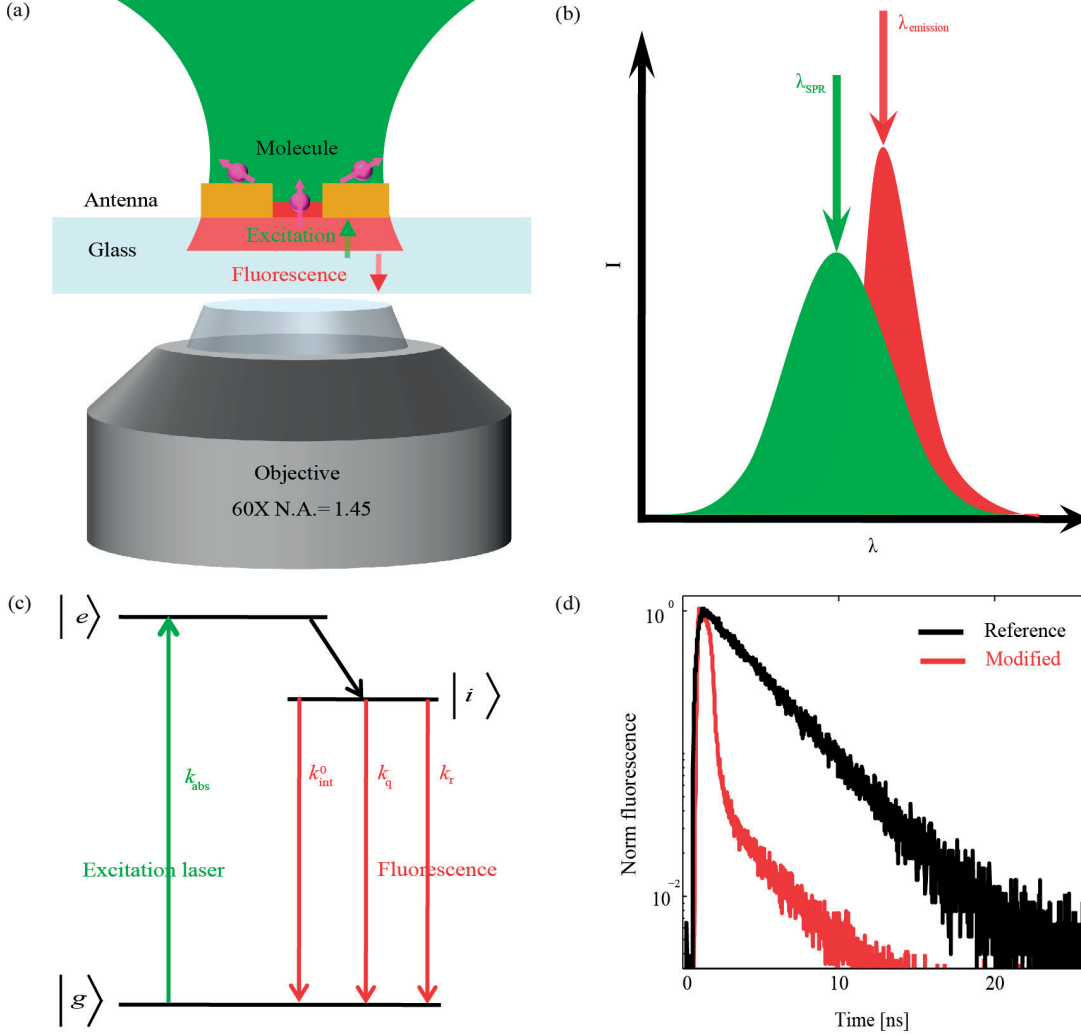


Figure 4.1: (a) Physical configuration used to study molecular plasmons. (b) The plasmon resonance (centered at λ_{SPR}) must overlap with the molecular emission (centered at $\lambda_{\text{emission}}$). (c) Jablonski diagram when the molecule interacts with the antenna [248]. (d) Fluorescence decay histogram with antenna (red curve) and without antenna (black curve).

the plasmonic nanostructure (red curve in Fig. 4.1(d)) will be faster than the reference case without a plasmonic nanostructure (black curve in Fig. 4.1(d)). The fluorescence enhancement (FE) is defined as the excitation enhancement multiplied by the quantum yield enhancement factor [251, 252]:

$$FE = F_{\text{ext}} \frac{\eta}{\eta_0}, \quad (4.1)$$

where $F_{\text{ext}} = \frac{|E_{\text{sc}}|^2}{|E_{\text{in}}|^2}$ is the excitation enhancement factor, which is calculated with the scattered intensity normalized by the incident intensity, η_0 is the initial quantum yield of the

molecule and η is the modified quantum yield of the molecule. The fluorescence lifetime and the quantum yield are defined as $\tau_0 = \frac{1}{k_r^0 + k_{int}^0}$ and $\eta_0 = \frac{k_r^0}{k_r^0 + k_{int}^0}$ when there are no plasmon nanostructures [253]. τ_0 is the initial lifetime, k_r^0 is the radiative decay rate, and k_{int}^0 is the intrinsic non-radiative decay rate. The presence of the plasmon antenna enhances the LDOS, which consequently increase the decay rate according to Fermi golden rule [254, 255]. These enhanced decay channels could be radiative or non-radiative (quenching) due to the intrinsic Ohmic losses of metallic nanostructures [22, 249, 250]. The enhanced radiative decay rate k_r and the quenching k_q result into faster decay, modified quantum yield, and shorter lifetime. The formula of the modified lifetime and enhanced quantum yield are derived as:

$$\tau = \frac{1}{k_{int}^0 + k_r + k_q} \quad (4.2)$$

and

$$\eta = \frac{k_r}{k_{int}^0 + k_r + k_q}. \quad (4.3)$$

In order to observe significant modifications of the fluorescence, molecules should be placed in the area where the near-field is strongly enhanced but not too close to the metal as the molecule might then be quenched [230, 249, 250]. In the following, I present two examples of fluorescence enhancement with negative nanoholes and sandwich cavity antennas.

4.2 Engineering fluorescence with negative nanoantenna

As mentioned in Chapter 2, negative antennas show extraordinary transmission [71] and have been used for many applications [65, 72–78]. In this particular project, the fluorescence enhancement is studied by exploiting the enhanced directional emission and the near-field enhancement depending on the thicknesses of the different holes for a 4-nanohole silver negative antenna (4-NHSNA).

4.2.1 Fluorescent dye molecules

The dye molecule ATTO 647N (ATTO-TEC GmbH) is used as emitter; it has a high photostability, is water soluble and has an initial quantum yield of 65% in water [256]. Its absorption peak is at $\lambda = 640$ nm, the emission peak is at $\lambda = 670$ nm and its lifetime in water is 3.6 ns. Its absorption peak corresponds to the emission wavelength of the excitation laser, which is a diode laser emitting at $\lambda = 640$ nm with a bandwidth of 2 nm and a pulse duration of 50 ns, as described in Sec. 2.5. The stock molecule solution with concentration of 0.1186 mM/L is dissolved in 3 wt% poly vinyl alcohol (PVA) with deionized water as a solvent. The ratio between the molecule solution and the PVA solution is 1:9 and the final concentration of the solution is 0.01186 mM/L. The molecules:PVA solution is spin coated on glass (as control sample) and on three different 4-NHSNAs samples with using of 6000 rpm for 60 s. The thickness of the PVA layer

with molecules is around 200 nm.

4.2.2 Metallic nanohole design, fabrication and characterization

The metallic nanoholes are milled with FIB as explained in Sec. 2.3. The designed 4-NHSNA is schematically shown in Fig. 4.2(a), together with a SEM image in Fig. 4.2(b). This design, which is the Babinet complementary to a structure that has been extensively studied in our laboratory [220], has been chosen for its high tunability.

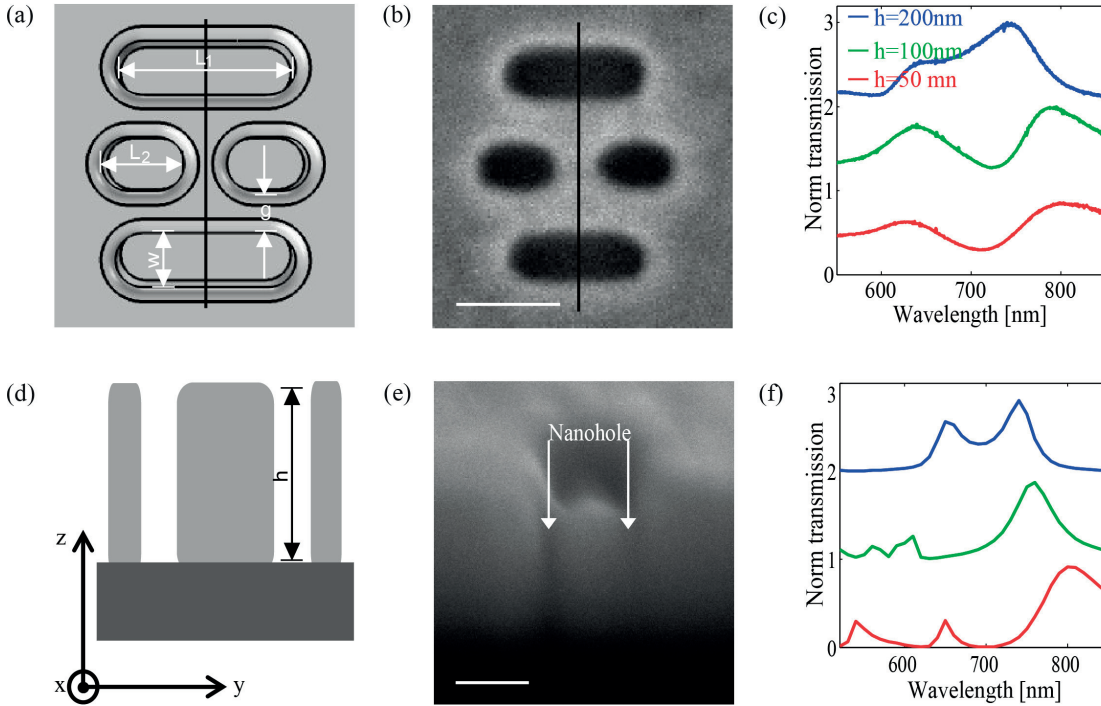


Figure 4.2: 4-nanohole silver negative antenna (4-NHSNA): (a) top view of the designed negative antenna, (b) SEM of the realized structure FIB milled in Ag (scale bar 100 nm), (c) measured and (f) calculated transmission spectra of the fabricated 4-NHSNA for three different metal thicknesses: 50 nm, 100 nm and 200 nm, (d) designed and (e) SEM image of the structure cross-section, indicating that the metal film has been etched through (scale bar 100 nm).

The gaps (g) between the adjacent rectangular individual holes are 40 nm, the width (w) is 40 nm for all the individual holes and the length of the inner hole (L_1) is 60 nm and the outside long ones (L_2) are 130 nm. The thicknesses (h) of the holes are varied for three different values: 50 nm, 100 nm and 200 nm, by adjusting the thickness of the metal film. The measured (with the VIR transmission and reflection spectroscopy described in Sec. 2.4.4), respectively calculated (with the periodic SIE described in Sec. 2.1) transmission spectra for the three different thicknesses are presented in Fig. 4.2(c), respectively Fig. 4.2(f). For the three 4-NHSNAs types, the spectra are asymmetric and particularly a resonant peak is observed at the wavelength $\lambda = 640$ nm, which overlaps with both the absorption peak of the molecule (ATTO

647N) and the excitation laser.

4.2.3 Experimental results

The fluorescence measurement is performed with the dark-field confocal fluorescence setup presented in Sec. 2.5. The fluorescence images for the three different types of 4-NHSNAs, the fluorescence signal over time and the fluorescence decays are presented in Fig. 4.3. Figures 4.3(a), 4.3(b) and 4.3(c) represent the fluorescence images for 4-NHSNAs with thicknesses $h = 50$ nm, $h = 100$ nm and $h = 200$ nm, respectively. The 4-NHSNAs are separated by $4\ \mu\text{m}$ and each of them appears as a bright spot when the molecules in the 4-NHSNAs emit fluorescence photons. For the fluorescence measurements, only one single structure is measured at a time. The fluorescence enhancement for the three different 4-NHSNAs is normalized to the fluorescence signal of the control sample as shown in Fig. 4.3(d).

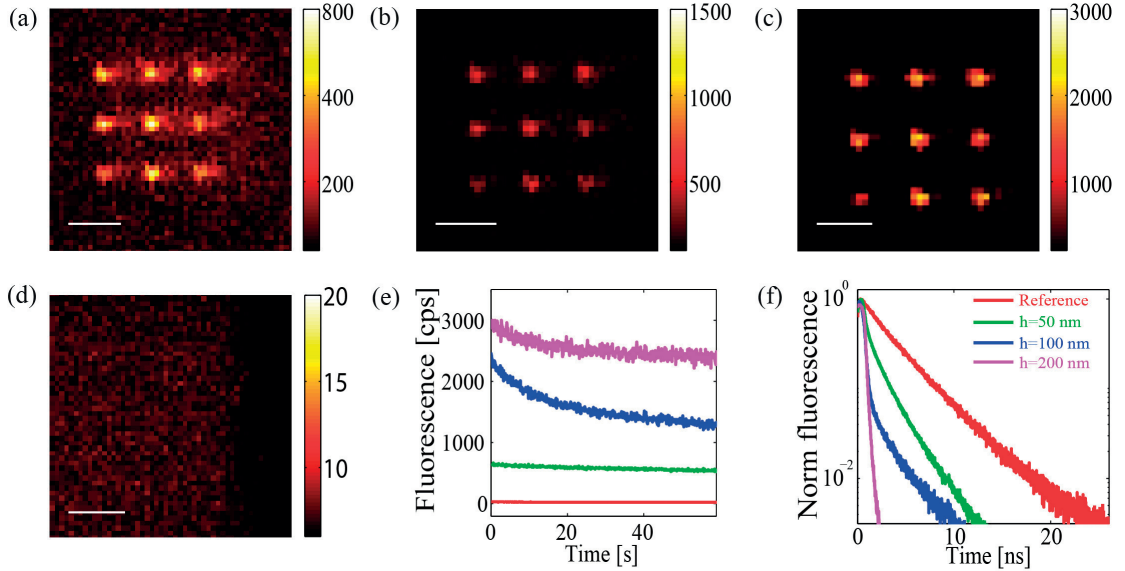


Figure 4.3: Fluorescence signal and decay histogram. Fluorescence image for 4-NHSNAs with thicknesses (a) 50 nm, (b) 100nm, and (c) 200 nm. The negative antennas are positioned $4\ \mu\text{m}$ away from each other and appear as individual bright spots. (d) Fluorescence image of the reference experiment without metal. (e) Fluorescence signal monitored over 60 s for different thicknesses of the negative antennas and for the control sample. (d) Fluorescence decay for the different antennas and the control sample. Scale bars in (a)-(d) are $4\ \mu\text{m}$.

The comparison of the fluorescence enhancement and the modification of lifetime for three different types of 4-NHSNAs are listed in Table 4.1. The enhancement is increased from 23 times for 4-NHSNAs with $h = 50$ nm, to 92.2 times for 4-NHSNAs with $h = 200$ nm as shown in the second column of Table 4.1. The fluorescence lifetime (obtained by numerically fitting the measured decays once they have been deconvoluted with the instrument response function; this operation is performed by the SymPhoTime 64 software (PicoQuant GmbH Germany) that pilots the PicoHarp 300) is also decreased from 3.6 ns to 0.22 ns, 0.45 ns and 1.8 ns for

	FE	η	τ (ns)
Reference		0.65	3.6
h=50 nm	23		1.8
h=100 nm	61.5		0.45, 3.4
h=200 nm	92.2		0.22

Table 4.1: Comparison of the experimental fluorescence enhancement and the modified lifetime for the three types 4-NHSNAs.

4-NHSNAs with $h = 200$ nm, $h = 100$ nm and $h = 50$ nm, respectively. The shortest lifetime is for the molecules that are spin coated on the 4-NHSNAs with $h = 200$ nm, which corresponds to the fastest decay, as confirmed in Fig. 4.3(f) (pink curve). The second lifetime 3.4 ns detected for the 4-NHSNAs with $h = 100$ nm is probably because there are some molecules far away from the metal surface and their radiative decay are not enhanced too much. The red curve is the fluorescence decay of the control sample, while the green, respectively blue curves are the decay of the molecules that are spin coated on 4-NHSNAs with $h = 50$ nm, respectively $h = 100$ nm.

The fluorescence enhancement for the three different 4-NHSNAs can also be normalized to the fluorescence signal of the control sample by taking into account the thickness of the spin coated molecular layer and the results are shown in Fig. 4.4.

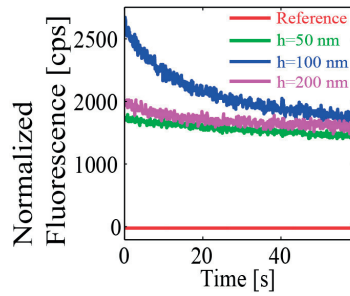


Figure 4.4: Fluorescence signal of 4-NHSNAs with thicknesses 50 nm, 100nm, and 200 nm, monitored over 60 s for different thicknesses of the negative antennas and for the control sample.

With this normalization, the highest fluorescence signal is 61.5 times that of the reference and it is achieved with the 4-NHSNAs of thicknesses 100 nm that is represented by the blue curve in Fig. 4.4.

4.3 Discussion

4.3.1 Near-field enhancement

To understand the reason why the fluorescence enhancement is different for the 4-NHSNAs with different thicknesses, the near-field intensities for the three 4-NHSNAs are calculated as shown in Fig. 4.5(a), 4.5(b) and 4.5(c) for the illumination wavelength $\lambda = 640$ nm. The near-field mapping on the y-z plane as shown in Fig. 4.5(d) and 4.5(e) which is the cross-section along the lines marked in the middle of Fig. 4.5(a) and 4.5(b), respectively. The near-field enhancement is the highest for 4-NHSNAs with $h = 200$ nm. The near-field enhancement can directly influence the absorption transition rate of the molecule, which in turn influences the final fluorescence enhancement according to the Eq. (4.1). The gradually enhanced near-field intensity as the thickness increases clearly confirms the near-field intensity enhancing both the excitation rate and the emission rate [74,230,249,250] as the fluorescence enhancement follows the increasing thickness of the 4-NHSNAs, while the lifetime decreases with the increasing thickness of 4-NHSNAs. The lifetime is decreased when the emission rates (radiative or non-radiative) are increased (Eq. (4.2)).

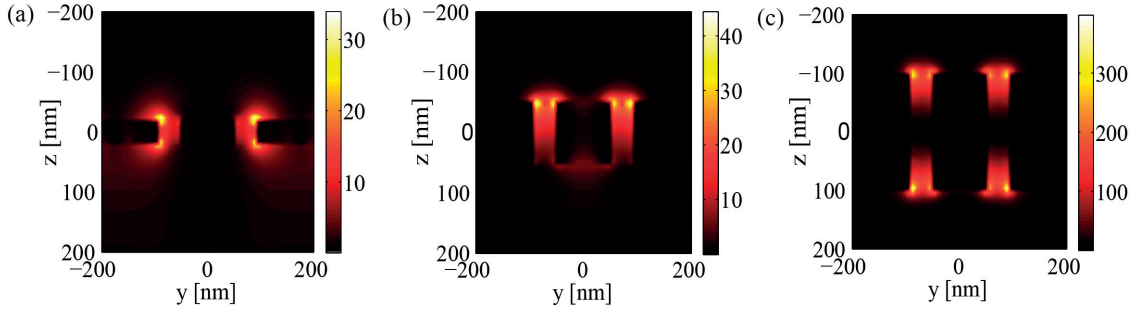


Figure 4.5: Calculated near-field intensity enhancement inside the negative antennas for different thicknesses: (a) $h = 50$ nm, (b) $h = 100$ nm and (c) $h = 200$ nm.

4.3.2 Improvement of emission directionality

The metallic nanoholes that build 4-NHSNAs can also increase the transmission and energy concentration [71, 257]. Here, I study this effect and use these properties to control the fluorescence emission by changing again the thickness of the metallic nanoholes. The measured emission pattern of the 4-NHSNAs for the control sample (the molecules spin coated on a glass substrate without metallic nanoholes) and the three different thicknesses using the Fourier imaging setup described in Sec. 2.4.5 are presented in Fig. 4.6.

The emission patterns for the three different 4-NHSNAs are normalized to the maximum fluorescence emission for the 200 nm thick 4-NHSNA, the latter producing the strongest fluorescence. We observe that the fluorescence emission is increasingly centered around the forward direction as the thickness of the 4-NHSNAs increases. The typical dipole emission

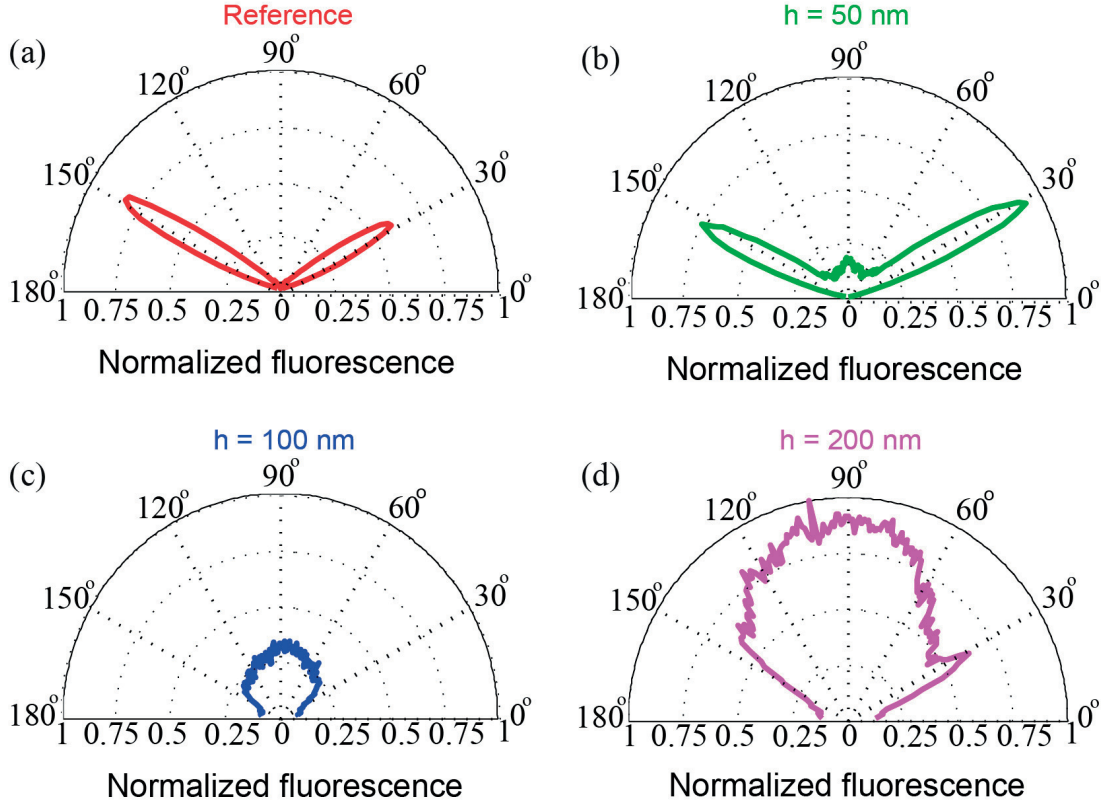


Figure 4.6: Measured fluorescence emission patterns for control sample and 4-NHSNAs with different thicknesses: (a) control sample, (b) $h = 50$ nm, (c) $h = 100$ nm and (d) $h = 200$ nm.

pattern is observed when the molecules are coated on glass (control sample, Fig. 4.6(a)), which is consistent with the literature [258,259]. The emission starts to appear in the forward direction (90° in the polar plot in Fig. 4.6(b)) for the metallic nanohole with thickness $h = 50$ nm, although most of the emission is still concentrated in the two lobes at 30° and 150° . The emission is increasingly concentrated in the forward direction around 90° and the emissions at the two lobes (at 30° and 150°) disappears when the thickness of the metallic nanohole increases to $h = 100$ nm, Fig. 4.6(c). Compared to the emission for the metallic nanohole with $h = 100$ nm, the emissions for the $h = 200$ nm thick metallic nanohole is even stronger, Fig. 4.6(d). The directionally enhances in that case and the forward emission eventually contributes mostly to the overall fluorescence enhancement. This is confirmed by the highest fluorescence enhancement for the 4-NHSNAs with thickness 200 nm (see the second column in Table 4.1).

4.4 Sandwich cavity antenna

Engineering emitters that are confined in small volumes is very interesting for nanophotonics [80,260]. The metal-insulator-metal nanosandwich antenna is a good candidate for this, since

it can have near-field enhancement between the layers and exhibits directional emission [160–165]. In this section, I developed a method to engineer the dye molecules in a sandwich antenna cavity with a diameter of 100 nm and a height of 50 nm.

4.4.1 Fabrication method

The process flow for the fabrication of such a sandwich cavity with dye molecules in the middle of the cavity is shown in Fig. 4.7. It combines the EBL and liftoff processes described in Sec. 2.2 with a surface chemical functionalization method.

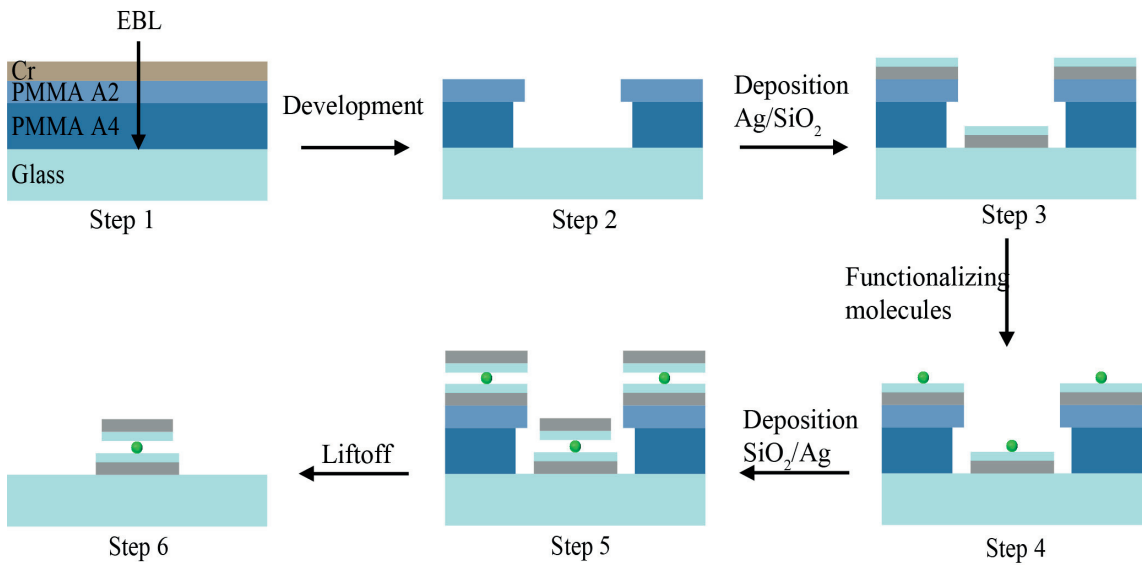


Figure 4.7: Schematic for fabrication of a cavity antenna with a molecule functionalized inside the cavity.

The process begins with normal EBL exposure, development as shown in Step 1 and 2 in Fig. 4.7. To form a sandwich cavity, a 20 nm silver and 5 nm SiO₂ are deposited with LAB 600. In Step 4, a layer of (3-aminopropyl) triethoxysilane (Sigma-Aldrich GmbH) molecule with a linking group of -NH₂⁺ is deposited on the surface of the sample in gas phase. The sample is then immersed for two hours in a solution of ATTO 647 molecules with a concentration of 3.95 mM/L. The ATTO 647 molecule from ATTO-TEC (absorption peak at $\lambda = 640$ nm, emission peak at $\lambda = 670$ nm and lifetime in water 2.4 ns) has a free -COOH group which reacts with the -NH₂⁺ group. The sample is then first washed with dionized water to remove the unbound molecules transferred again into the evaporation chamber of the LAB600 for the deposition of SiO₂ and the second Ag layer. Again 5 nm SiO₂ and 20 nm Ag are evaporated and liftoff in acetone is performed for one day. Finally, the sample is showered with isopropyl alcohol (IPA) and dried with N₂ gas. The finished sample ends up with the ATTO 647 molecules right in the middle of the cavity, as shown at Step 6 in Fig. 4.7.

4.4.2 Optical properties of the fabricated sandwich cavity

The SEM images of the fabricated sandwich cavity is shown in Fig. 4.8(a) (top view) and Fig. 4.8(b) (30 ° tilted view). The sandwich cavity clearly shows the three layers structure.

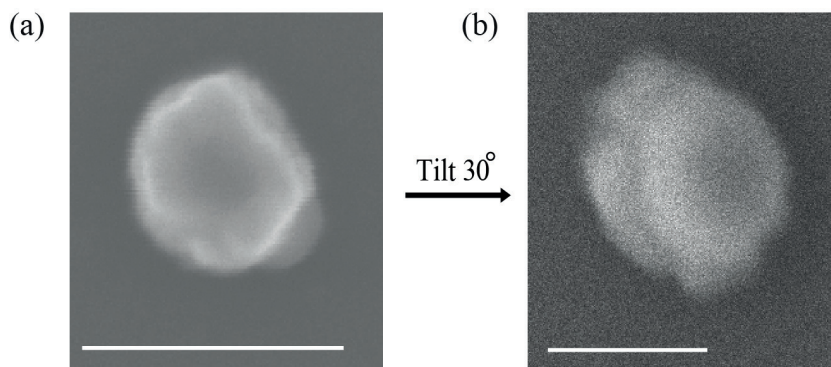


Figure 4.8: SEM of the fabricated cavity antenna: (a) top view (scale bar 200 nm) and (b) 30 ° tilted view (scale bar 100 nm).

The schematic of the sandwich cavity is shown in Fig. 4.8(a) and the measured and calculated scattering cross-sections for the fabricated sandwich cavities are shown in Fig. 4.9(c); both cross sections have been normalized to their peak value. From the SEM images, we obtain the exact dimensions of the fabricated sandwich cavity with a bottom Ag disk with a diameter of 104 nm and a top Ag disk with a diameter of 72 nm. The thicknesses of both Ag disks are 20 nm. The SiO₂ layer has a 10 nm thickness and a diameter around 104 nm. The scattering spectrum for the sandwich cavity is asymmetric and has a dip at the wavelength of $\lambda = 640$ nm. The near-field enhancement at this particular wavelength is calculated both in the x-y plane (Fig. 4.8(b)) and the x-z plane (Fig. 4.9(d)). The typical dipole mode intensity distribution is clearly seen in Fig. 4.9(b) with strong electric intensity enhancement.

4.5 Results and discussion

The fluorescence imaging and decay measurements are performed with the setup described in Sec. 2.5 and the results are shown in Fig. 4.10.

To confirm that the molecules have survived the metal deposition processes (Step 5 in Fig. 4.7) and the liftoff, the fluorescence signals for the cavity antenna and reference sample are chopped (by randomly cutting the laser off for a few seconds) and measured over 60 s (Fig. 4.9(c)). The recovery of the fluorescence signals prove that the molecules are still alive after the metal deposition and the liftoff process, Fig. 4.10(c). The fluorescence enhancement is found to be 7.2 times by normalizing the fluorescence signal from the antennas (Fig. 4.10(b)) to the fluorescence signal of the reference (Fig. 4.10(a)). The lifetime is reduced from 2.4 ns to 0.44 ns. The rather modest value for the fluorescence enhancement is quite disappointing, especially since the near-field enhancement is really high (up to several hundred times) and

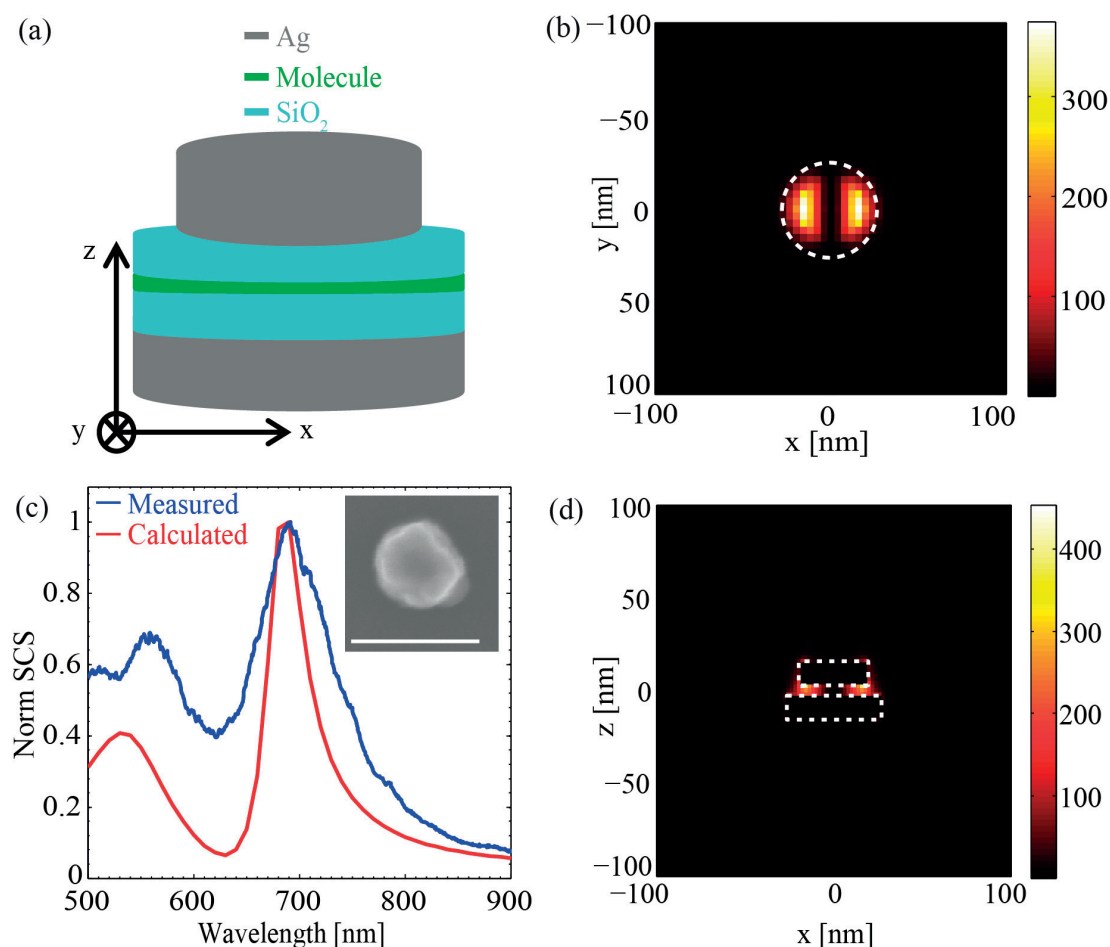


Figure 4.9: (a) Schematic of the cavity antenna. (c) Measured (blue curve) and calculated (red curve) normalized optical scattering spectra for the cavity antenna (the inset shows a SEM image with scale bar 100 nm). Calculated near-field intensity enhancement maps in the (b) x-y and in the (d) x-z plane. The white dashed circle and rectangles indicate the antenna structure.

the lifetime is reduced dramatically (from 2.4 ns to 0.44 ns) indicating an enhanced decay rate. There are two possible reasons for the modest fluorescence enhancement. One is that the near-field enhancement is only high at the edges of the top disk and the central region of the cavity exhibits only very low near-field enhancement, Fig. 4.9(b)-(d). Thus, most of the molecules might not experience the high near-field enhancement. The second reason would be that the molecules are placed too close to the nanodisk with only a 5 nm SiO₂ spacing layer, such that most of the fluorescence photons are absorbed by the nanodisk (so-called quenching) due to the short distance between the molecules and the metal [249, 250].

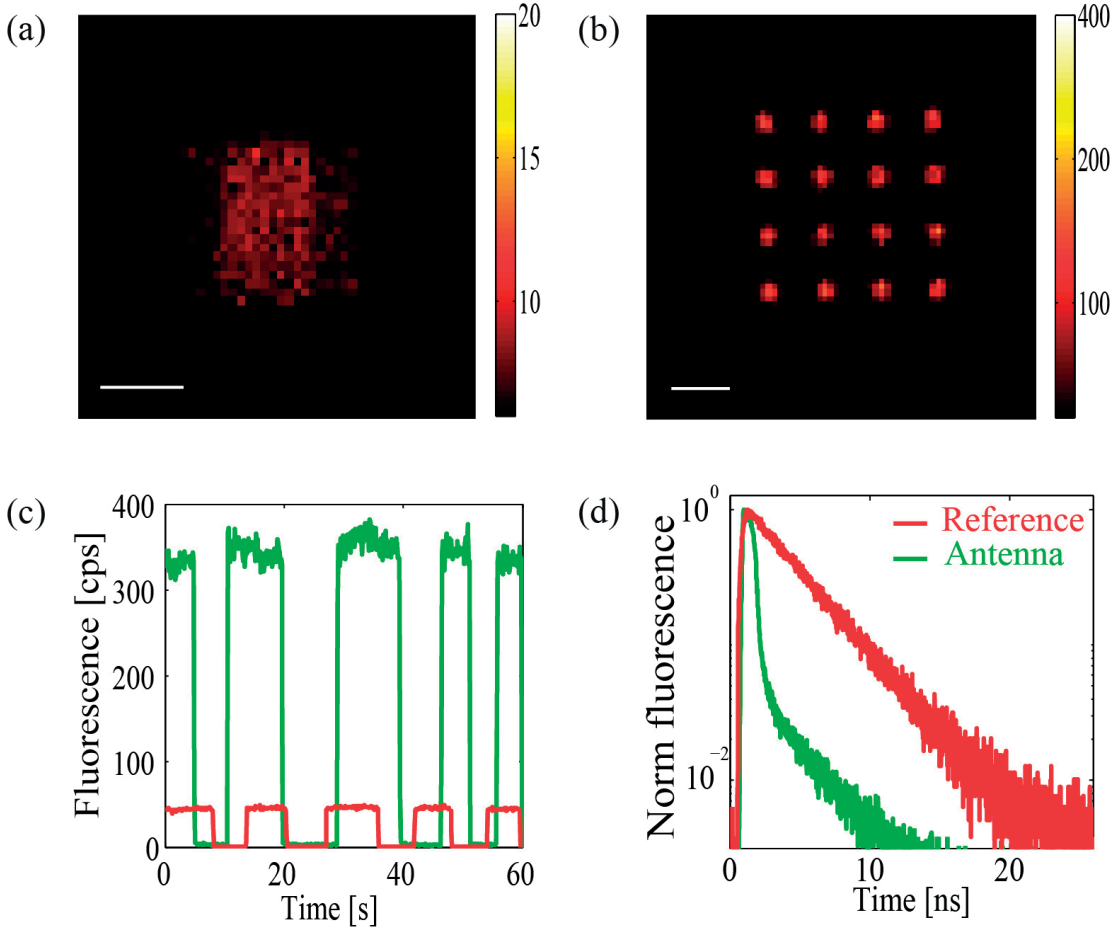


Figure 4.10: Fluorescence image and decay histograms. Fluorescence images for (a) the control sample and (b) the cavity antenna (scale bars $3 \mu\text{m}$). (c) Fluorescence signal over 60 s and (d) fluorescence decay histograms.

4.6 Summary

Two different nanoantennas, 4-NHSNAs and sandwich cavity antennas, have been used to engineer the fluorescence for water soluble dye molecules (ATTO 647N and ATTO 647) positioned at their vicinity, where there exist a strong near-field enhancement.

We see that "open structures", such as the 4-NHSNAs produce both a very significant field enhancement, together with a beaming effect that can be used to direct the fluorescence in a specific direction. Both effects strongly depend on the metal thickness in which the antennas have been milled, which provides an interesting degree of freedom for designing this effect.

For the sandwich cavity antenna a modest fluorescence enhancement has been observed and further investigations are required. Possible reasons for this disappointing performance could be the non-homogeneous near-field enhancement in the cavity and the fluorescence quenching caused by the proximity of the molecules to the metal. However, the merit of

this experiment is to demonstrate that fluorescent molecules can survive the subsequent nanofabrication steps required to sandwich them between metallic nanostructures.

Both approaches pursued in this chapter have promising potential for studying the fluorescence in confined plasmonic geometries, with dimensions in the $100 \times 100 \text{ nm}^2$ range.

5 Engineering fluorescence with Fano plasmonic systems

The previous chapter has investigated experimentally two approaches to engineer the fluorescence using confined plasmonic nanostructures with dimensions in the $100 \times 100 \text{ nm}^2$ range. In this chapter, I design a 4-nanorod silver antenna (4-NRSA) that can generate a nearly homogeneous plasmonic hot spot with strong near-field enhancement by exploiting Fano resonances, Fig. 5.1(a). To fully utilize the hot spots for the near-field interaction of emitters and plasmonic antennas, I have developed an immobilization strategy that combines a two-step EBL with surface chemical functionalization to position the molecules in a $30 \times 30 \text{ nm}^2$ nanogap area. The fluorescence intensity and lifetime are studied for the molecules that are confined in this minute area, where they are excited by the strong near-field associated with the plasmonic Fano resonance. The main issue in this interaction is how to position spectrally the molecule, with respect to the Fano resonance, Fig. 5.1(b). The experiments are supported with numerical modeling using SIE and the two show good agreement.

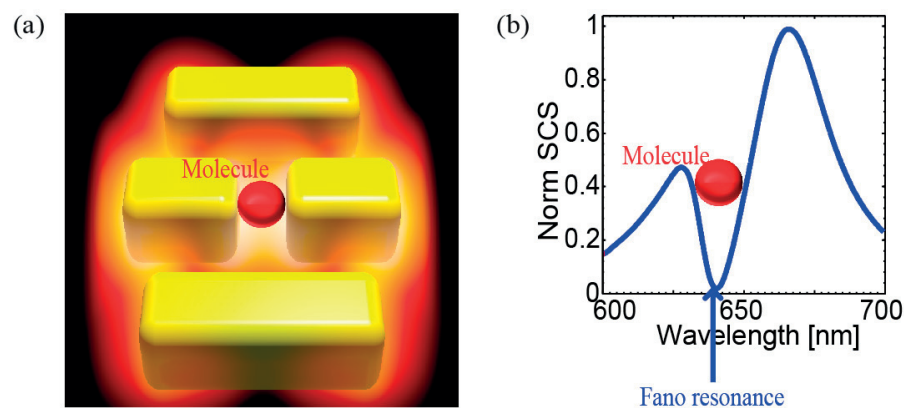


Figure 5.1: (a) Molecule sitting on a plasmonic hot spot in the gap of a 4-NRSA structure. (b) Fano resonance observed in the scattering cross section of the 4-NRSA structure.

5.1 Introduction

The study of the interaction between quantum emitters and plasmonic nanostructures bears both a fundamental physical interest and practical applications. From the Purcell effect to the dynamics of modified transition rates for fluorescence, a quantum emitter coupled to a plasmonic system has been intensively investigated over decades [229, 239, 244, 261–268]. The spontaneous emission rate can be strongly enhanced by the increased local density of states (LDOS) produced by the plasmonic nanostructure. Consequently, the decay rate of a quantum emitter is modified by the enhanced LDOS [254, 255]. Both excitation and emission rates of a quantum emitter can be increased with plasmonic nanostructures [74, 249, 250, 269–275]. The enhanced emission rate of quantum emitters coupled to a plasmonic system can be radiative or non-radiative since plasmonic nanostructures are lossy [22, 249, 250, 252, 276, 277].

The fundamental physics of a quantum emitter coupled to a plasmonic system, combined with modern nanotechnology, has inspired numerous applications including single molecule detection [22, 24–31] and nano-biophotonics [32–45]. Extremely high fluorescence enhancement has been achieved by first quenching the molecule to an extremely low quantum yield and taking then advantage of a large radiative enhancement [278, 279].

Although quantum emitters coupled to a plasmonic system have been extensively studied and different ways of engineering them have been proposed, a robust and easily tunable approach to control this interaction through the choice of the plasmonic nanostructure and the positioning of the fluorescent molecule still represents a difficult task. In particular, the distance between the quantum emitters and the plasmonic nanostructure determines whether radiative emission or quenching dominates. As for the fabrication of plasmonic nanostructures in general, two approaches for this task are possible: top-down and bottom up. Bottom-up techniques such as DNA assembly have been shown to achieve high spontaneous emission enhancement [27, 33]; however, they are not very deterministic and cannot be used to engineer optical nanocircuits. Top-down approaches, on the other hand, can be used to pattern quantum emitters in a plasmonic hot spot and to develop quantum optical circuits [80, 280].

Two key technological challenges are 1) to selectively immobilize quantum emitters at the hot spot of the plasmonic nanostructure and 2) to find a plasmonic nanostructure that can be easily tuned to explore different spectral coupling conditions with the fluorescent molecules.

To address this second challenge, I consider a Fano-resonant plasmonic nanostructure made of Ag. Fano resonances arise in plasmonic nanostructures from the interference between two modes, usually a dark and a bright one that are generated through near-field coupling between components of a plasmonic system [281, 282]. Fano-resonant plasmonic systems have a typical asymmetric lineshape, as illustrated in Fig. 5.1(b), with a narrow dip. They exhibit a stronger near-field enhancement compared to conventional Lorentz type plasmonic structures. Over the last few years, there has been a surge of experiments reported on these systems, with applications including plasmonic rulers, nonlinear optics, SERS and ultrasensitive sensing

[48–58]. The energy is mostly confined in the near-field at the dip of the Fano resonance, which is particularly interesting for studying quantum emitters [44].

Fano resonance can also be obtained from the interference of two bright modes, as is the case for the 4-NRSA structure studied in this chapter [220]. An advantage of this structure is that its Fano resonance can be easily tuned over a significant wavelength range and is quite tolerant to small geometry variations associated with nanofabrication inaccuracies. Thus it is an ideal plasmonic cavity to engineer fluorescence and study the interaction between a quantum emitter and a plasmonic nanostructure.

This chapter addresses three different issues: I use 4-NRSAs to generate a nearly homogeneous strongly enhanced near-field plasmonic hot spot at the Fano resonance; I immobilize relatively high quantum yield molecules (ATTO 647) in the extremely small $30 \times 30 \text{ nm}^2$ area in the gap of the 4-NRSA using a two-step EBL and selective chemical functionalization; I demonstrate that high fluorescence enhancement can be achieved even with relatively high initial quantum yield molecules by tuning the Fano resonance to the excitation and emission peaks of the molecules.

5.2 Fano plasmonic resonant system

5.2.1 Fano plasmonic resonant mechanism

In order to generate a homogeneous plasmonic hot spot, a 4-NRSA as illustrated in Fig. 5.2(a) is used. The red curve in Fig. 5.2(b) shows the normalized far-field scattering cross-section (Norm SCS) for a 4-NRSA calculated with the SIE method described Sec. 2.1. For Ag, a realistic dielectric function is taken (Johnson and Christy) [85] and the surrounding refractive index is set to 1.33 to approximate the small substrate-induced frequency shift of the plasmon resonances [86]. There is a dip in the asymmetric Fano lineshape of the plasmonic resonance in the 4-NRSA system, see Fig. 5.2(b). The near vanishing far-field scattering indicates that the energy of the system is mainly confined in the near-field. The single 4-NRSA consists of two long rods with lengths $L_1 = 130 \text{ nm}$ and two short rods with lengths L_2 (in Fig. 5.2 $L_2 = 68 \text{ nm}$, but this parameter will be varied in our study). The widths and thicknesses are 40 nm for all the individual nanorods and the gaps d between the rods are set to 30 nm . The 4-NRSA produces a plasmonic hot spot with strong near-field enhancement at the Fano resonance due to destructive interference of the two dipole modes supported by each pair of rods. This is illustrated in Fig. 5.2(c), where we see in the surface charge that the dipole mode supported by the outer rods is out of phase by 180° with respect to the dipole mode supported by the inner rods. The near-field enhancement is calculated by taking a cross-section of the antenna in the x - y plane in the middle of the structure at the wavelength $\lambda = 640 \text{ nm}$, revealing the strongest enhancement in the gap, Fig. 5.2(d).

The comparison of the near-field enhancement between the 4-NRSA Fano resonance system and the counterpart dipole resonance antenna (including only both inner rods) is made in

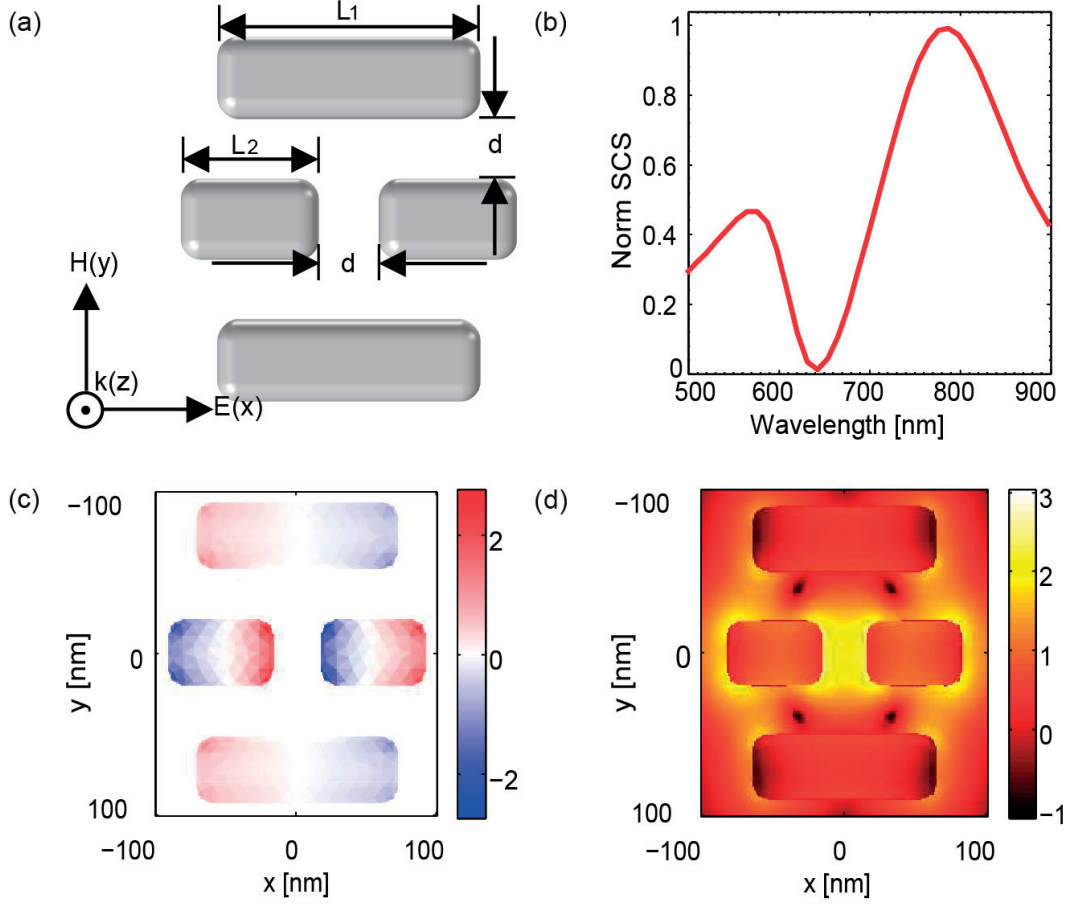


Figure 5.2: Mechanisms of Fano resonance for the generation of a nearly homogeneous hot spot in a 4-NRSA system. (a) Schematic of the 4-NRSA. (b) Corresponding scattering spectrum calculated with the SIE method. (c) Surface charge distribution at the Fano resonance wavelength $\lambda = 640$ nm. (d) Intensity enhancement distribution at the Fano resonance wavelength $\lambda = 640$ nm (logarithmic scale).

Fig. 5.3 to show the advantages provided by a Fano-resonant system. Both the 4-NRSA Fano-resonant system (same dimensions as in Fig. 5.2) and the dipole antenna system (length 74 nm, gap 30 nm, width and thickness 40 nm, such that it is resonant at the same wavelength) produce a hot spot, Figs. 5.3(a) and 5.3(b). To compare the near-field enhancement in those hot spots, 49 locations (exact values given in Appendix C1) are selected to cover the $30 \times 30 \text{ nm}^2$ square area. Due to the reflection symmetry along the x - and y -axes, only 16 points located in the first quadrant are considered for each structure as indicated by the black dots in Figs. 5.3(a) and 5.3(b), where the near-field intensity is measured. The near-field enhancement for the Fano system (red curve) is indeed significantly stronger than that of the dipole antenna (blue curve), Fig. 5.3(e). The field enhancement provided by the Fano-resonant system compared to the dipole system is relatively constant in the region of interest and amounts to 45%, Fig. 5.(f) (note that this enhancement is larger for the Ag structures considered here and only amounts

to 40% for structures made of Au [220]).

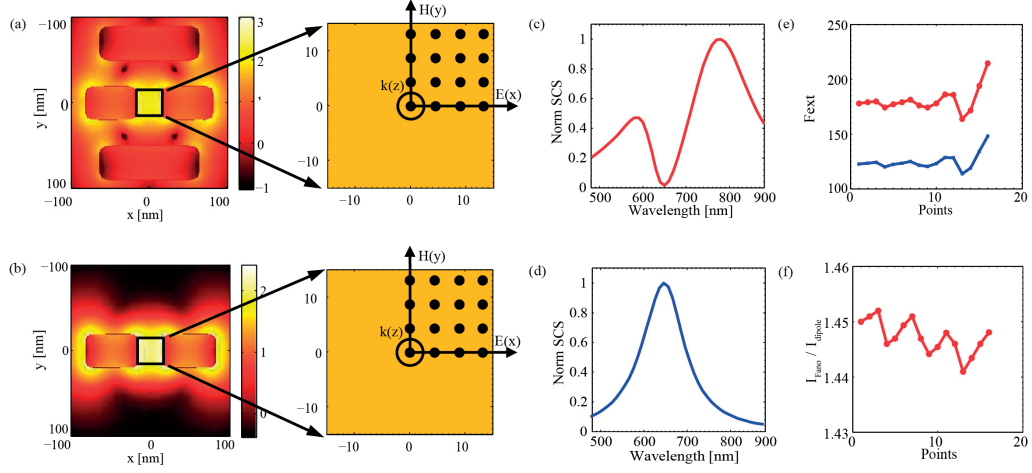


Figure 5.3: Comparison of the near-field enhancement in the hot spots between a 4-NRSA system and a dipole antenna system. (a) Near-field intensity distribution (logarithmic scale) for the 4-NRSA at the Fano resonance wavelength $\lambda = 640$ nm and the 16 points where the near-field is computed. (b) Corresponding dipole antenna, including only both inner rods (a). Normalized scattering cross-sections (c) for the 4-NRSA with a resonance at $\lambda = 640$ nm and (d) for the dipole antenna with a Lorentz resonance also at the wavelength $\lambda = 640$ nm. (e) Near-field intensity enhancement at the 16 points for the 4-NRSA Fano system (red curve) and the dipole antenna (blue curve). (f) Ratio of the near-field intensity enhancement between the Fano system and the dipole antenna at the 16 points at the resonance wavelength $\lambda = 640$ nm.

5.2.2 Immobilizing the molecule in nanogap

For the present work, the dye molecule ATTO 647 (ATTO-TEC GmbH) is chosen. This molecule has high photostability, is water soluble and has an initial quantum yield of 20% in water. Its absorption peak is at $\lambda = 640$ nm and the emission peak is at $\lambda = 670$ nm; the lifetime in water is 2.4 ns. The molecules are immobilized with a two-step EBL followed by chemical functionalization and liftoff process as shown in Fig. 5.4. First, the 4-NRSA is fabricated with a first EBL and liftoff. Then the 4-NRSA is coated again with a double layer resist in order to expose only the gap region, as shown in Step 4, Fig. 5.4. A 20 nm silicon dioxide layer is first deposited in order to immobilize the molecules in the middle position (vertical direction) of the antenna. Then the surface of the sample is functionalized with a layer of (3-aminopropyl) triethoxysilane (Sigma-Aldrich GmbH) molecules in order to provide a linking group $-\text{NH}_2^+$. The sample is then immersed in an ATTO 647 molecule solution with a concentration of 3.95 mM/L for 2 hours. The number of molecules that are immobilized in the nanogap is estimated to be around 42 ± 10 using the formula of $N_m = MVN_A$, where N_m is the number of molecules that are functionalized in the nanogap, M is the Molar concentration, V is the volume of the nanogap and N_A is the Avogadro constant. The ATTO 647 molecule has a free $-\text{COOH}$ group which reacts with $-\text{NH}_2^+$ group. The sample is then washed with deionized water first and is

transferred into acetone base for 10 minutes to remove all the resist. Finally, the sample is showered with isopropyl alcohol and dried with a nitrogen gun. The finished sample ends up with the ATTO 647 molecules in the nanogap only, as shown in Step 6 in Fig. 5.4.

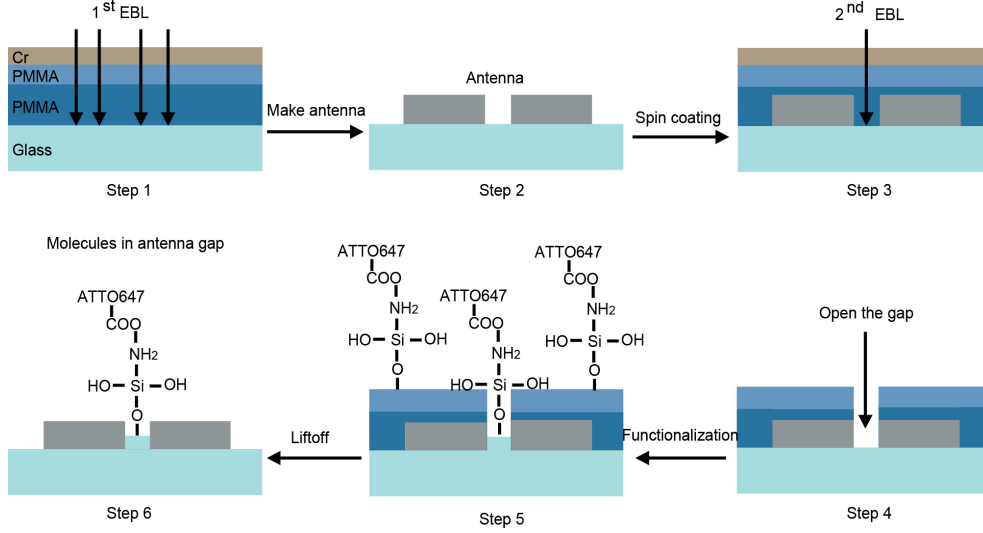


Figure 5.4: Schematic of the two-step EBL process for the selective surface functionalization of molecules in the gap of the 4-NRSA.

5.2.3 Engineering the spectral overlap between the Fano resonance and the absorption/emission of the molecules

It is known that the interaction between a quantum emitter and a plasmonic system strongly depends on the spectral position of the plasmon resonance with respect to the absorption or emission frequencies of the molecule [252]. This holds for conventional plasmonic systems that exhibit a broad Lorentzian response. Here, I will show that a Fano-resonant system, with its narrow spectral dip, provides an interesting system to investigate this interaction. To this end, I have designed three different spectral configurations: (A) the Fano dip overlaps with the excitation peak of the molecule; (B) the Fano dip overlaps with the emission peak of the molecule and (C) the Fano dip is off-resonance, away from the excitation or emission wavelengths of the molecule, to serve as reference experiment. As described in Sec. 2.5, I use again a diode laser emitting at $\lambda = 640$ nm with a bandwidth of 2 nm and a pulse duration of 50 ns as excitation source. The required spectral position for the Fano dip for the three required configurations is easily obtained by tuning the length of the two short inner nanorods from $L_2 = 68$ nm (configuration A, $\lambda = 640$ nm) to $L_2 = 75$ nm (configuration B, $\lambda = 670$ nm) and $L_2 = 82$ nm (configuration C, $\lambda = 700$ nm). Figure 5.5(a) gives the SEM images of a typical fabricated 4-NRSA ($L_2 = 68$ nm and fabrication details see Sec. 2.2.2). The calculated scattering spectra and the measured dark-field scattering spectra for the 4-NRSA agree very well, Fig. 5.5(b)-(c). The resonance position overlapping for the three configurations are shown in Fig. 5.5(d)-(f), in which the black vertical lines indicate the Fano dip positions. Taking configuration A as an

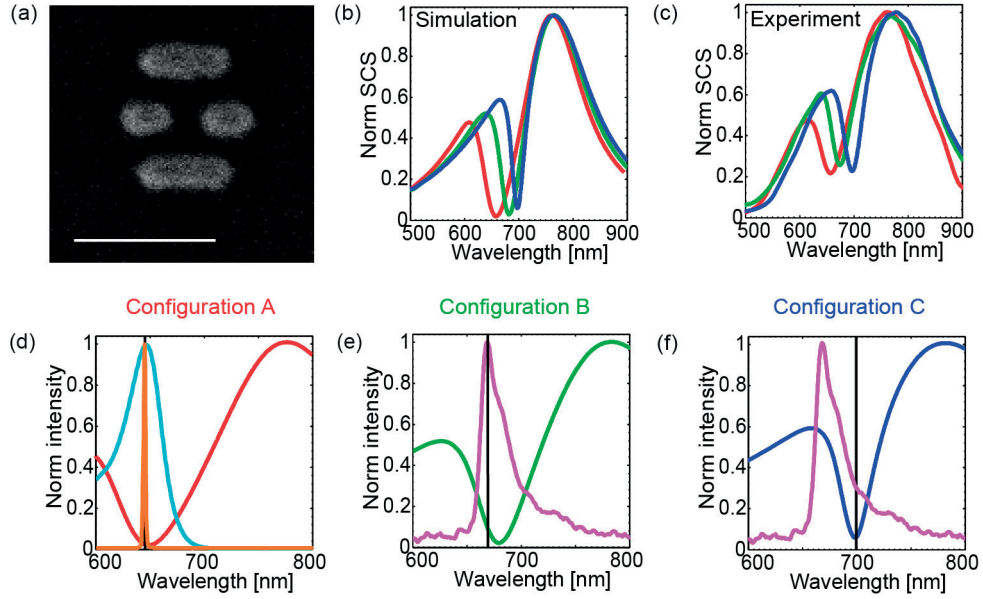


Figure 5.5: Spectra overlap for different configurations. (a) SEM image of a typical fabricated 4-NRSA (scale bar 200 nm). (b) Calculated scattering spectra for three different 4-NRSA structures with three different Fano resonances at $\lambda = 640$ nm ($L_2 = 68$ nm, configuration A), $\lambda = 670$ nm ($L_2 = 75$ nm, configuration B) and $\lambda = 700$ nm ($L_2 = 82$ nm, configuration C). (c) Measured scattering spectra corresponding to the three configurations in (b). (d) Configuration A: the Fano resonance (red curve) overlaps with the excitation laser line (orange curve which overlaps with the absorption peak of the molecule: cyan curve). (e) Configuration B: the Fano resonance (green curve) overlaps with the emission peak of the molecule (purple curve). (f) Configuration C: the Fano resonance (blue curve) is away from absorption and emission peaks (purple curve); the vertical black lines in (d)-(e) mark the Fano resonance dip.

example, the excitation peak represented by the laser excitation line (cyan curve in Fig. 5.5(d)) overlaps with the Fano resonance (red curve in Fig. 5.5(d)) at the wavelength of $\lambda = 640$ nm. Figures 5.5(e)-(f) show the Fano resonances (green curve in Fig. 5.5(e) and blue curve in Fig. 5.5(f)) at their corresponding wavelengths $\lambda = 670$ nm and $\lambda = 700$ nm.

5.3 Fluorescence enhancement and lifetime

5.3.1 Experimental data

The fluorescence measurements (fluorescence image and decay) are performed with a home-made dark-field confocal fluorescence microscope system described in Sec. 2.5. Figure 5.6(d) represents the fluorescence image of the control sample where the molecules are functionalized on a glass substrate in a square area with dimensions $10 \mu\text{m} \times 10 \mu\text{m}$. The fabricated 4-NRSA are grouped in 5×5 arrays with a $4 \mu\text{m}$ period such that in the fluorescence image they are represented by 25 bright spots as shown in Figs. 5.6(a)-(c). To confirm that the molecules

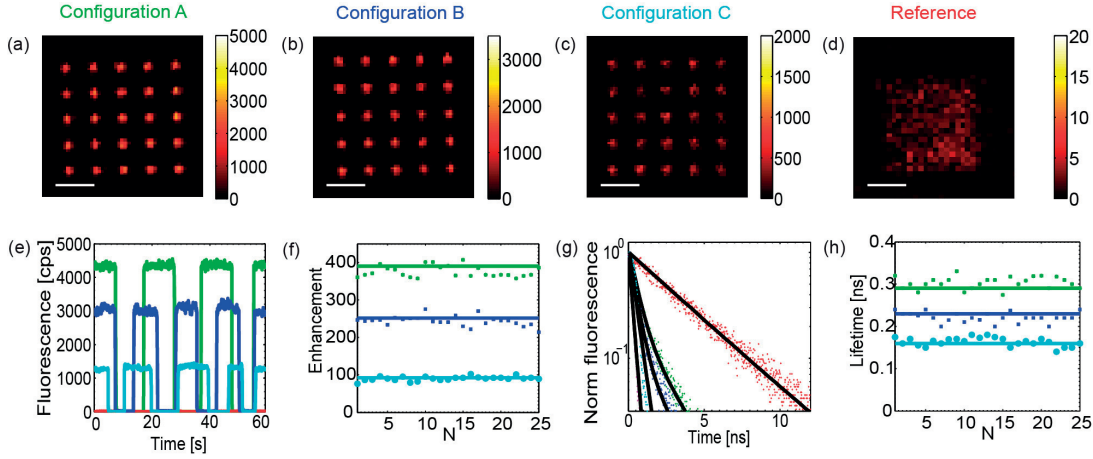


Figure 5.6: Fluorescence images and decay histograms. Fluorescence images for a 5×5 antennas array for (a) for configuration A, $L_2 = 68$ nm; (b) for configuration B, $L_2 = 75$ nm, and (c) for configuration C, $L_2 = 82$ nm. (d) Fluorescence image of a reference sample with the ATTO647 molecule patterned in a square area with dimensions $10 \mu\text{m} \times 10 \mu\text{m}$. (e) Fluorescence signal traces over time (60 s) for the three configurations and the reference. (f) Fluorescence enhancement for the three configurations measured over the 25 antennas in the array (N represent the 4-NRSAs number in the array). (g) Fluorescence decay of the reference (red curve), configuration A (green curve), configuration B (blue curve) and configuration C (cyan curve); as well as instrument response function (purple curve). (h) Fluorescence lifetime for the three configurations. Scale bars in (a)-(d) are $4 \mu\text{m}$.

survive the complex nanofabrication processes associated with area-selective surface functionalization and liftoff (Steps 5 and 6 in Fig. 5.4), the fluorescence signals are randomly chopped (by cutting the laser off) and measured over 60s, Fig. 5.6(e). The recovery of the fluorescence signals demonstrates that the molecules are still alive after the surface functionalization and the liftoff processes.

Different fluorescence enhancements are observed in Figs. 5.6(a)-(c) for the three configurations, with the brightest spots for configuration A. A quantitative comparison of the fluorescence signals for the three configurations is shown in Fig. 5.6(e), where the configuration A exhibits the strongest fluorescence signal (green curve). The averaged fluorescence enhancement obtained from the 25 antennas in configuration A is 395 ± 24 , which is 1.6 times, respectively 4 times, larger than configurations B (252.8 ± 12.2), respectively C (97.3 ± 7.8). Figure 5.6(f) shows the comparison of averaged fluorescence enhancement for the three configurations. One can see that both configurations, the plasmonic resonance adapted to the excitation (A) and the emission (B) exhibit higher fluorescence enhancement than configuration C. Figure 5.6(g) shows the fluorescence decay where the solid dot curves are the measurements and the black curves are exponential fits. The decay is much faster when the molecules are functionalized in the 4-NRSA (configuration A, green dots in Fig. 5.6(g)) compared with the control molecules (red dots in Fig. 5.6(g)). In the case of fluorescence decay, configuration C (cyan curve) is the fastest, as indicated by the shortest lifetime 0.16 ns

(0.29 ns for configuration A and 0.23 ns for configuration B). Interestingly, the highest fluorescence enhancement (configuration A) does not necessarily correspond to the fastest decay, as the fluorescence decay is faster in configuration B although it yields a lower fluorescence enhancement. This can be understood by the fact that configuration A produces a higher excitation of the molecule than configuration B because the plasmon resonance is tuned at the excitation of the molecule. When the plasmonic resonance is tuned to the emission of the molecule, the emission enhancement should be higher and one expects the emission enhancement for configuration B to be higher than that of configuration A. However, the total fluorescence enhancement depends both on the excitation and emission enhancements. Thus which of the two (excitation or emission on resonance) would dominate the total fluorescence enhancement will be investigated in the next section.

A clear fact is that the total fluorescence enhancement for both excitation and emission on resonances (configurations A and B) exhibit higher enhancement than configuration C which is the off-resonance case. An interesting result is that the modified lifetime of configuration C is the shortest. This means that the total decay rates (radiative and non-radiative) are the fastest among these three configurations. The smallest total fluorescence enhancement for configuration C can be understood from two perspectives. On the one hand, the excitation enhancement is small as the plasmonic resonance is tuned far away from the excitation of the molecule. On the other hand, although the total decay rates are the highest (see the decay in Fig. 5.6(g)), the quenching is high so the measured fluorescence enhancement in the far-field is low. This means that the fluorescence emission from the molecule is strongly absorbed by the plasmonic nanostructure and less power is emitted into the far-field. This will be confirmed in the next section using numerical calculations for the fluorescence enhancement and the lifetime modification.

5.3.2 Numerical data

Using the formula Eqs. (4.2) and (4.3) from the previous, the modified lifetime and enhanced quantum yield are derived as:

$$\tau = \frac{1}{k_{int}^0 + k_r + k_q} = \frac{\tau_0}{1 - \eta_0 + \eta_0(F_r + F_q)} \quad (5.1)$$

and

$$\eta = \frac{k_r}{k_{int}^0 + k_r + k_q} = \frac{\eta_0 F_r}{(1 - \eta_0) + \eta_0(F_r + F_q)}, \quad (5.2)$$

where $F_r = \frac{P_{rad}}{P_{dip}}$ is the radiative enhancement factor, $F_q = \frac{P_{abs}}{P_{dip}}$ is enhanced quenching factor, P_{rad} is the radiative power, P_{abs} is the Ohmic loss, $P_{dip} = \omega^4 \frac{|\vec{p}|^2}{12\pi\epsilon_0 c^3}$ is the power emitted by a classical dipole in vacuum [283], ω is the angular frequency, \vec{p} is the dipole moment, ϵ_0 is the vacuum permittivity and c is the speed of light in free space. The details for the method to

calculate the radiative power and the loss are described in [252].

In the experiment, we have estimated that about 42 ± 10 molecules are functionalized inside the nanogap area. In the simulations, a molecule is considered as a classical dipole along the x-axis positioned successively at the 49 coordinates indicated in Fig. 5.7(a). Due to the symmetry along x and y-axes, only 16 points located in the first quadrant need to be computed. The fluorescence enhancement and the modification of the lifetime are averaged over these 16 points and then compared to the experimental results. Since these coordinates spread homogeneously in the hotspot area, the average of k_r and k_q will provide a good estimate for molecules placed randomly in the gap. The k_r and k_q are further divided by 3 when calculating the radiative and quenching enhancement factors, which is a good approximation take into account the random orientation of the molecules [252]. As an example, a dipole is positioned at the origin (0, 0, 0) of the coordinate system and oriented along the x-axis, the calculated excitation enhancement, enhanced quantum yield, fluorescence enhancement and modified lifetime are shown in Fig. 5.7 for the configuration A ($\lambda = 640$ nm). Figure 5.6(b) shows that the excitation enhancement factor is maximum (109.57) at $\lambda = 640$ nm. The quantum yield is enhanced to 0.73 from the initial value of 0.2. Using Eqs. (4.1) and (5.2), the fluorescence enhancement is found to be 402. The lifetime is decreased from 2.4 ns to 0.28 ns according to Eq. (5.1). The fluorescence of the molecule is highly enhanced and the lifetime is significantly shortened. The calculated fluorescence enhancement, modified lifetime, enhanced quantum yield, enhanced radiative and quenching factors at the 16 different locations are provided in the appendix (Table C.1-3) for the three different configurations.

5.3.3 Comparison the results between experiment and calculation

To better understand how the excitation and emission enhancement factors can influence the overall fluorescence enhancement, I compare the excitation enhancement factor and the quantum yield for the three configurations in Table 5.1.

		F_{ext}	η	FE	τ (ns)
Reference			0.2		2.3
Configuration A	EXP			397	0.298
	CAL	128.4	0.7	449.4	0.253
Configuration B	EXP			252.8	0.232
	CAL	81.5	0.74	309.7	0.176
Configuration C	EXP			97.3	0.168
	CAL	40.3	0.72	151	0.133

Table 5.1: Comparison of the experimental (EXP) and calculated (CAL) excitation enhancement (F_{ext}), quantum yield (η), fluorescence enhancement (FE) and lifetime τ for the three configurations.

The numerically calculated fluorescence enhancements also show that the largest value (443.42) is achieved in the case of configuration A. The shortest lifetime also occurs for con-

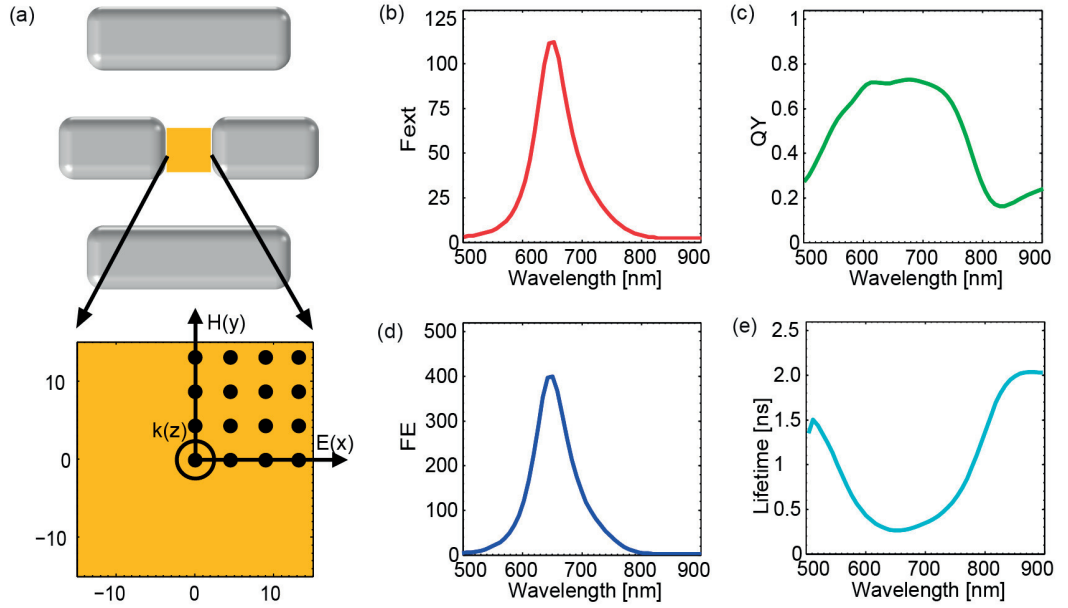


Figure 5.7: Numerical modeling of a dipole emitter in the gap of a 4-NRSA. (a) Schematics of the positions (black dots) where the dipole is successively placed in the gap of the 4-NRSA. Calculated values for (b) the excitation enhancement factor, (c) the quantum yield, (d) the fluorescence enhancement, and (e) the modified fluorescence lifetime.

figuration C. These numerically calculated largest fluorescence enhancement and shortest lifetime agree with the experimental results. The excitation enhancement is highest (126.25) when the plasmon resonance is tuned to the absorption peak (configuration A), compared to the other two configurations (B: 91.26 and C: 47.58). When the plasmon resonance is tuned to favor the radiative enhancement (configuration B), the highest quantum yield (0.74) is obtained, which means the highest radiative enhancement. However, the fluorescence enhancement for configuration A is higher than for configuration B. We can thus conclude that the excitation enhancement dominates the total fluorescence enhancement. Also, the radiative enhancement does not show a significant difference between the different configurations. Thus the quantum yield enhancement does not vary dramatically over a broad range, see Fig. 5.7(c). Therefore high excitation enhancement is one way to achieve a large fluorescence enhancement. Another way is to use low intrinsic quantum yield emitters [279] or to quench the intrinsic quantum yield on purpose as shown in the literature [278]; resulting in a very significant quantum yield enhancement in the vicinity of plasmonic nanostructures. In this work the plasmonic resonance can be tuned to preferably enhance either excitation or emission of the molecule and high total fluorescence enhancement can be obtained in both cases. As expected, the fluorescence enhancement is lower when the plasmon resonance is tuned far away from the excitation and emission of the molecule. By comparing configurations B and C, I found that a faster decay (shortest lifetime) does not necessarily mean a higher

radiative enhancement. In this case, the decay can use non-radiative channels associated with the Ohmic losses of the plasmonic nanostructure, which results in higher quenching and eventually produces a lower quantum yield (see Table 5.1 columns 4). The quantum yield is higher for configuration B (0.74) than for configuration C (0.72) because in that latter case the non-radiative decay caused by Ohmic losses is higher.

5.4 Summary

In conclusion, using numerical calculations, I have designed Fano-resonant 4-NRSAs that have been spectrally tuned to produce nearly homogeneous plasmonic hot spots at specific wavelengths. Experimentally, by exploiting selective chemical functionalization and two-step EBL, it was possible to fabricate these structures and immobilize molecules in the extremely small nanogap area where the plasmonic hot spot lies. I have studied fluorescence enhancement and lifetime modification for these molecules by tuning the Fano plasmonic resonances on the excitation or on the emission of the molecules. The results show that total fluorescence enhancement is largest when the Fano resonance is either on the excitation or the emission of the molecules, compared to the off-resonance reference case where the Fano resonance is far away from them. Furthermore, the excitation enhancement is the strongest and dominates the total fluorescence when the Fano plasmonic resonance is tuned on the excitation of the molecule. On the other hand, the quantum yield enhancement does not dominate the total fluorescence enhancement, even when the Fano resonance is preferably tuned on the emission of the molecule. This is because the quantum yield enhancement does not exhibit dramatic differences for the various configurations studied here. In summary, the modification of fluorescence lifetime can be significant due to the high enhancement of both radiative and non-radiative decays. The non-radiative decay enhancement due to Ohmic losses shortens the lifetime and decreases the quantum yield enhancement at the same time. The technology presented here for selectively deploying quantum emitters on nanometric plasmonic hot spots has interesting potentials for nano-engineering nanophotonic circuits that combine quantum emitters with plasmonic nanostructures.

6 Conclusion and Outlook

To briefly summarize this thesis, it has aimed at providing some advanced nanofabrication techniques for plasmonics, a vivid field of research that utilizes the strong near-field enhancement produced by nanostructures made of noble metals (particularly Au and Ag). Motivated by fabricating nanoscale plasmonic devices with tiny active areas (hot spots in the $100 \times 100 \text{ nm}^2$ range), I have investigated various systems, in particular designing structures made of low-loss Ag that offers significant advantages over gold in the visible spectrum, as well as toward lower wavelengths.

Nanophotonics is a complex field of research, where surprising optical effects can occur. It is therefore necessary to utilize advanced modeling techniques to design nanostructures that will produce the required effects and to gain understanding in their functioning principle. For this thesis, I was mainly interested in the strong field enhancement, the tunability of the plasmon resonances - including unusual resonances such as Fano resonances - and on the interaction between plasmonic nanostructures and fluorescent molecules. The SIE proved a very well suited tool to address these issues and the rounded mesh used for the simulations enabled a good agreement between the calculated optical properties and the experimentally measured ones.

Probably the most important (and time-consuming) parts of this work are the developments of original nanofabrication techniques to realize plasmonic nanostructures with well controlled features down to about 10 nm. Contrary to what is usually done in plasmonics, I have focused on Ag as plasmonic metal, since it has significantly lower losses than Au, the metal of choice for plasmonics. This choice came with a rather high price tag, since Ag is difficult to use for fabrication and it deteriorates extremely rapidly. For example, because of its short-term chemical stability, Ag cannot survive relatively low temperatures, e.g. the 5 min. baking on a hot plate required to cure photoresist for EBL. Understanding the Ag deterioration mechanisms and finding a cure for them was the focus of Chap. 3, where we first proved experimentally that oxidation and sulfidation were not directly responsible for the deterioration of Ag antennas. Instead, we found that water, viz. high relative humidity, was the essential reason for Ag deterioration. Adsorbed water on the surface of a Ag nanoantenna, promoting Ag ions migration,

seems to be the key process leading to Ag deterioration. Thus, a dehydration process using an Ar gas flow to remove water molecules from the fabricated antennas transformed Ag from this unstable amorphous state to a stable polycrystalline state and the plasmonic nanostructures treated that way remained stable up to 14 weeks. The surface roughness of Ag film was also improved by applying this dehydration process. The thermal stability was also improved and it was possible to utilize more complicated processes to fabricate Ag antennas and films.

Throughout this thesis, I have used different nanofabrication techniques to define structures with dimensions in the sub-100 nm range. The key techniques were EBL combined with liftoff using a positive resist or IBE etching using a negative resist, as well as FIB. The dimensions of the EBL fabricated nanostructures could be controlled accurately by adjusting the exposition dose on their edge with the Layout BEAMER conversion software. Gap antennas with gap dimensions as small as 15 nm were fabricated for different applications, including biosensing (Au dipole antenna), plasmonic chirality (T-shape antenna made of Ag) and nonlinear optics (heptamers made in Al). Relatively large antenna arrays have also been fabricated using point exposure with a large current. Metasurfaces made of Au, Ag, and Al have been fabricated to study the second harmonic generation, phase engineering, and revisiting the classical Newton rings with plasmonics. Negative metallic structures that represent the Babinet counterpart to positive structures have been FIB milled in metals; small gaps were obtained even in soft metals such as Ag, by using a hard mask layer (SiO_2 or Al_2O_3).

Often, nanofabrication is essentially planar, with nanostructures fabricated as a single layer on a substrate. Building normal to the surface is much more challenging and requires tricks, including multiple EBL steps. In that context, I have observed that sandwich cavity structures made by liftoff showed imperfect rounded edges; to overcome this, an IBE process was developed for fabricating perfect metal-dielectric-metal structures. For example, Ag- Al_2O_3 -Ag tandem antennas were fabricated using this process and applied for the generation of red, green and blue colors. Alignment accuracy was also strongly improved by adding one level of alignment markers for EBL, enabling an alignment accuracy close to the EBL resolution. This three-level alignment procedure was used to fabricate 4-NRSAs that were used in fluorescence enhancement study.

These different nanostructures have been used for experimental studies on the interaction between plasmonic nanostructures and quantum emitters, starting with Chap. 4. Negative metallic nanohole antennas and sandwich cavity antennas were investigated in that chapter. The fluorescence enhancement was found to be dependent on the thickness of the negative antenna. This is because the near-field enhancement is larger when the thickness of the negative antenna increases. Also, the fluorescence emission directionality is better for thick metallic nanoholes. Both the near-field enhancement and the emission directionality contribute to the overall fluorescence enhancement and these results could be useful to design sensors that rely on fluorescence. The sandwich cavity antennas have been fabricated with EBL combined surface chemical functionalization methods to confine molecules in the middle of the cavity whose diameter was around 100 nm. Unfortunately, the measured fluorescence enhancement

was rather low; this is likely to be caused by the non-homogeneous near-field enhancement in the cavity and the quenching of the molecules which are very close to the metal.

In Chapter 5, a highly tunable Fano-resonant plasmonic system was designed and used to study the interaction between fluorescent molecules and plasmonic systems. The molecules were confined during the nanofabrication step in a $30 \times 30 \text{ nm}^2$ gap, where the near-field enhancement is strongest. Through tuning of the Fano resonance, it was possible to investigate different energetic configurations, where the Fano dip was spectrally aligned with the absorption or the emission wavelength of the molecule. In those experiments, we have observed that the overall fluorescence enhancement is stronger when the Fano resonance dip is on the excitation or the emission of the molecule, rather than when it is far away from them. Furthermore, the excitation enhancement was the largest and dominated the overall fluorescence enhancement when the Fano dip was tuned on the excitation of the molecule. On the other hand, the quantum yield enhancement does not appear to dominate the total fluorescence enhancement and does not vary much for the different configurations. This indicates that the modification of fluorescence lifetime can be significant, thanks to the high enhancement of both radiative and non-radiative decays.

In summary, the work presented here indicates that progress in plasmonics requires the combination of many different ingredients. Versatile and accurate numerical tools are essential to guide the design of plasmonic nanostructures that exhibit interesting physical effects. However, to realize these structures, one needs to invest very significant efforts in the development of technologies that can produce nanostructures with controlled dimensions down to about 10 nm. These developments are quite slow and necessitate mastering a broad variety of clean-room techniques; indeed, this thesis has shown that one single nanofabrication technique is not sufficient to produce all types of interesting structures and one always need to choose the most appropriate one, or to combine different techniques to fabricate one specific sample. The methodology to pattern molecules in an very small $30 \times 30 \text{ nm}^2$ area certainly paves the way for the development of optical circuits at the nanoscale, that could be used to investigate quantum emitters interacting with a well controlled environment, including but not limited to plasmonic materials. Chapters 4 and 5 have only scratched the surface of these topics and there remains much more to be investigated. Probably a very interesting future area here would be to understand in greater detail how the local interaction between fluorescent molecules and plasmonic nanostructures can influence their radiation pattern. The dehydration process proposed in Chap. 3 should make Ag a more useful material for plasmonics. I do hope that experiments using structures fabricated with that process will take place in the future; I can well envision that nonlinear plasmonics could benefit from Ag nanostructures. Another very interesting field of research enabled by the dehydration process is the study of heterogeneous plasmonic nanostructures that combine Ag with other metals. To conclude, this thesis has demonstrated some original nanofabrication techniques and pointed out a few interesting directions where they could be used.

A Abbreviations

Abbreviation	Full name
AFM	Atomic force microscopy
ATR	Attenuation total reflection
EBL	Electron beam lithography
FIB	Focused ion beam
IBE	Ion beam etching
IRF	Instrument response function
SEM	Scanning electron microscope
SIE	Surface integral equation
SPAD	Single photon avalanche photodiode
TCSPC	Time-correlated single-photon counting
XPS	X-ray photoelectron spectroscopy

Table A.1: Table of frequently used short name instrumental words in the thesis.

Abbreviation	Full name
CAN	Ceric ammonium nitrate
DI	Deionized
HSQ	Hydrogen silsesquioxane
IPA	Isopropanol
KOH	Potassium hydroxide
MIKA	Methyl isobutyl ketone
PCA	Perchloric acid
PVA	Polyvinyl alcohol
PMMA	Poly methyl methacrylate
TMAH	Tetramethylammonium hydroxide
ZEP	Styrene methyl Acrylate

Table A.2: Table of frequently used short name of chemically related words in the thesis.

Appendix A. Abbreviations

Abbreviation	Full name
4-NRSA	4-nanorod silver antenna
4-NHSNA	4-nanohole silver negative antenna
DFSS	Dark-field scattering spectroscopy
FE	Fluorescence enhancement
IR	Infrared
LDOS	Local density of optical state
LSPR	Localized surface plasmon resonance
PTVH	Peak-to-valley height
QY	Quantum yield
QEPS	Quantum emitter-plasmonic systems
RH	Relative humidity
RMS	Root mean square
SCS	scattering cross-section
SPP	Surface plasmon polariton
SERS	Surface enhanced Raman scattering
THz	Tera-hertz
VIS	Visible
UV	Ultraviolet

Table A.3: Table of frequently used short name of physics related terms in the thesis.

B Tracking the dehydrated Ag antenna for 14 weeks

The complete information on the evolution of the morphology and optical response for 4-nanorod silver antennas up to 14 weeks is shown in Fig. B.1. The 4-NRSAs maintain a good morphology over this long period, Fig. B.1(a), Fig. B.1(b), Fig. B.1(c), Fig. B.1(d), Fig. B.1(i), Fig. B.1(j), Fig. B.1(k) Fig. B.1(l). Furthermore, the evolution over time of the Fano resonance dip for the dark-field scattering spectrum is shown in Fig. B.1(q); where the error bar is 6.5nm.

Appendix B. Tracking the dehydrated Ag antenna for 14 weeks

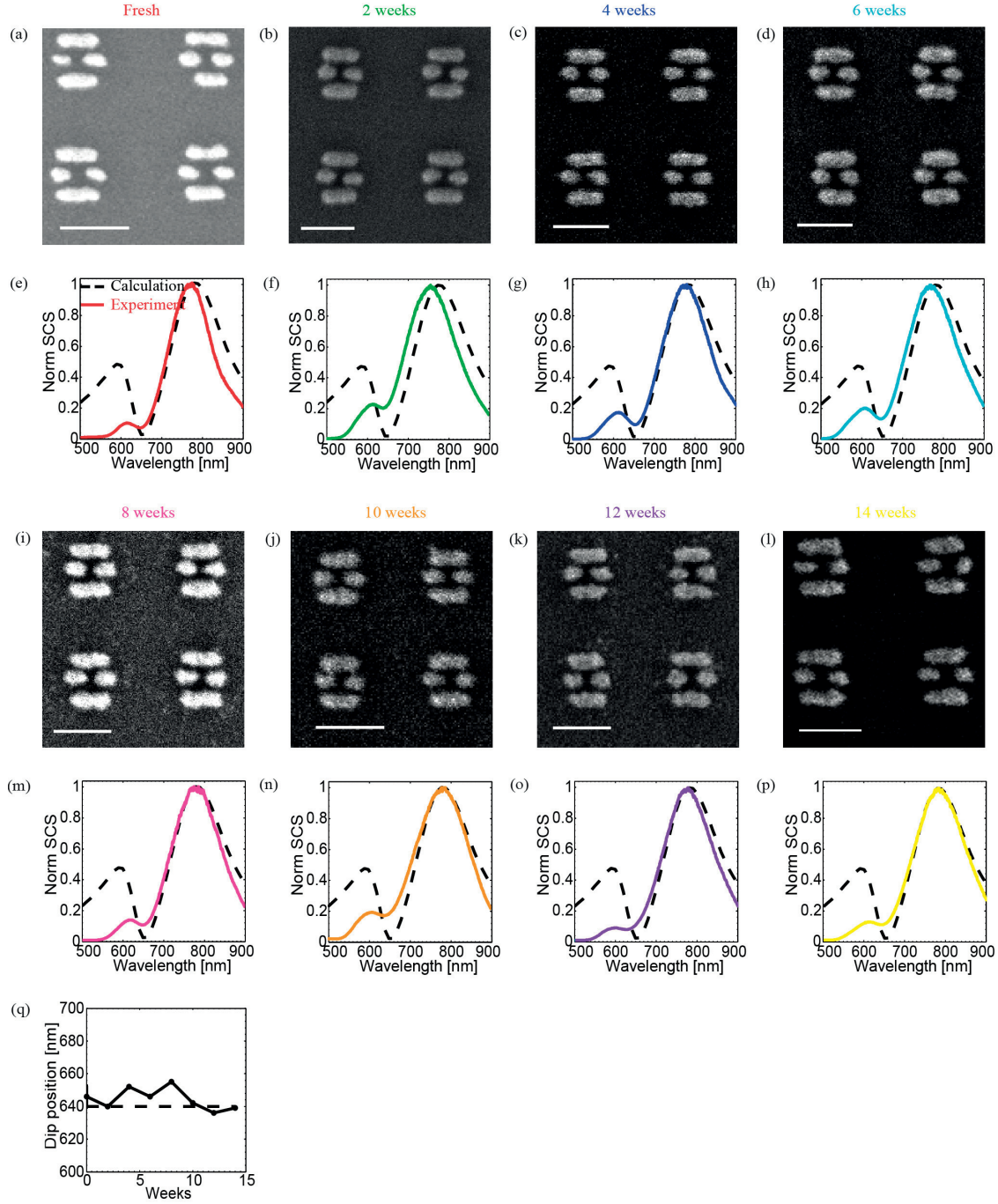


Figure B.1: Temporal tracking of morphology and optical properties of the 4-NRSA over a long period of time (14 weeks). SEM images of (a) the freshly fabricated 4-NRSA, the dehydrated 4-NRSA stored under ambient conditions after (b) 2 weeks, (c) 4 weeks and (d) 6 weeks. (e - h) DFSS corresponding to (a - d). SEM images of the dehydrated 4-NRSA stored under ambient conditions after (i) 8 weeks, (j) 10 weeks, (k) 12 weeks and (l) 14 weeks. (m - p) DFSS corresponding to (i - l). The dashed black curve corresponds to the scattering spectrum of the 4-NRSA calculated with SIE. (q) Evolution of the Fano dip spectral position over 14 weeks. The scale bars in (a - d) and (i - l) are 200 nm.

C Numerical modeling of the fluorescence enhancement averaged over the 16 points

Average the fluorescence enhancement and lifetime modification. A dipole is placed on a quart of a square area at 16 different points, which are (0, 0, 0), (30/7, 0, 0), (60/7, 0, 0), (90/7, 0, 0), (0, 30/7, 0), (30/7, 30/7, 0), (60/7, 30/7, 0), (90/7, 30/7, 0), (0, 60/7, 0), (30/7, 60/7, 0), (60/7, 60/7, 0), (90/7, 60/7, 0), (0, 90/7, 0), (30/7, 90/7, 0), (60/7, 90/7, 0) and (90/7, 90/7, 0) as shown in Fig. C.1. The fluorescence enhancement and modification of the lifetime are averaged over these 16 points to compare with experimental results. The origin (0, 0, 0) position in the coordinate is taken at the half height of the antenna as the 40 nm height gap is filled with 20 nm (thickness) SiO₂ experimentally, which makes the molecule sitting in the middle (vertical direction) of the gap. All the calculated excitation enhancement factors (F_{ext}), the radiative enhancement factors (F_{rad}), the quenching enhancement factors (F_q), the modified QY (η), the FE and the modified lifetime (τ) are listed in Table C1-3 for 16 positions of all the three configuration (A, B, and C).

Appendix C. Numerical modeling of the fluorescence enhancement averaged over the 16 points

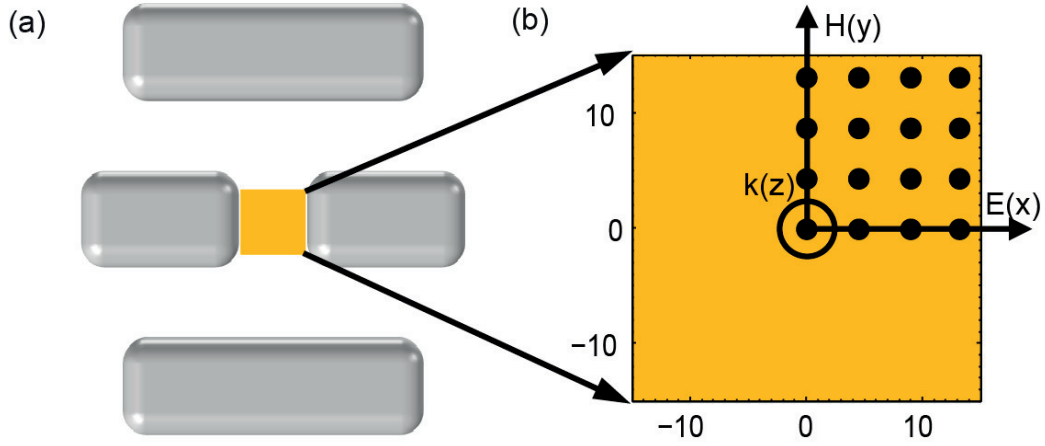


Figure C.1: Schematic showing the 16 different positions in the gap of the 4-NRSA. (a) $30 \times 30 \text{ nm}^2$ gap of the 4-NRSA marked with yellow square. (b) 16 different positions where the dipole is placed represent by the black dots in the first quart of the $30 \times 30 \text{ nm}^2$ gap of the 4-NRSA.

Configuration A	F_{ext}	F_r	F_q	η	FE	τ (ns)
Reference				0.2		2.3
(0, 0, 0)	109.57	30.619	7.108	0.7338	402.01	0.2875
(30/7, 0, 0)	116.39	32.513	7.674	0.7358	428.19	0.2715
(60/7, 0, 0)	136.48	38.149	9.764	0.7348	501.46	0.2311
(90/7, 0, 0)	161.78	45.875	18.308	0.6728	544.25	0.176
(0, 30/7, 0)	106.57	29.787	6.967	0.7308	389.47	0.2944
(30/7, 30/7, 0)	113.85	31.806	10.077	0.7329	417.21	0.2761
(60/7, 30/7, 0)	136.54	38.205	23.845	0.7304	498.89	0.2295
(90/7, 30/7, 0)	173.44	49.084	6.419	0.638	553.31	0.1559
(0, 60/7, 0)	96.575	26.991	7.078	0.7214	348.39	0.320
(30/7, 60/7, 0)	104.25	29.048	9.846	0.7293	377.33	0.299
(60/7, 60/7, 0)	130.87	36.293	24.33	0.7238	473.64	0.2393
(90/7, 60/7, 0)	192.81	53.745	24.33	0.6547	631.23	0.1462
(0, 90/7, 0)	79.985	22.339	5.428	0.7032	281.23	0.3777
(30/7, 90/7, 0)	86.593	23.939	5.975	0.7058	305.61	0.3538
(60/7, 90/7, 0)	110.22	29.597	8.158	0.7088	390.64	0.2873
(90/7, 90/7, 0)	164.12	41.666	16.289	0.6725	551.87	0.1936

Table C.1: Average 16 points for the calculation of fluorescence enhancement and the modified lifetime for the configuration A.

Configuration B	F_{ext}	F_r	F_q	η	FE	τ (ns)
Reference				0.2		2.3
(0, 0, 0)	79.604	52.398	12.995	0.7459	300.54	0.1729
(30/7, 0, 0)	84.442	55.57	13.91	0.7474	319.3	0.1633
(60/7, 0, 0)	98.674	64.988	17.043	0.7468	372.69	0.1394
(90/7, 0, 0)	116.55	77.821	27.387	0.6988	415.26	0.1098
(0, 30/7, 0)	77.396	50.948	12.701	0.7435	291.44	0.1773
(30/7,30/7, 0)	82.553	54.317	13.697	0.745	311.33	0.1666
(60/7,30/7, 0)	8.609	64.976	17.378	0.7434	370.98	0.1389
(90/7,30/7, 0)	124.64	83.025	33.991	0.6691	427.56	0.0991
(0,60/7, 0)	70.254	46.229	11.659	0.7363	262.39	0.1939
(30/7,60/7, 0)	75.674	49.638	12.696	0.738	283.14	0.1809
(60/7,60/7, 0)	94.456	61.625	16.798	0.7377	353.11	0.1455
(90/7,60/7, 0)	137.96	90.428	35.145	0.6822	481.42	0.0926
(0,90/7, 0)	58.476	38.439	9.8467	0.7224	214.95	0.2295
(30/7,90/7, 0)	63.131	41.07	10.689	0.7242	232.5	0.2152
(60/7,90/7, 0)	79.781	50.382	13.92	0.7258	294.25	0.1756
(90/7,90/7, 0)	117.99	70.413	24.676	0.6956	419.21	0.1211

Table C.2: Average 16 points for the calculation of fluorescence enhancement and the modified lifetime for the configuration B.

Configuration C	F_{ext}	F_r	F_q	η	FE	τ (ns)
Reference				0.2		2.3
(0, 0, 0)	41.657	61.042	18.03	0.7348	153.05	0.1444
(30/7, 0, 0)	44.169	64.739	19.171	0.7364	162.64	0.1365
(60/7, 0, 0)	51.638	75.825	22.923	0.738	190.56	0.1167
(90/7, 0, 0)	61.313	91.382	31.866	0.7181	220.16	0.0943
(0, 30/7, 0)	40.505	59.349	17.572	0.7334	148.53	0.1482
(30/7,30/7, 0)	43.145	63.214	18.805	0.7348	158.53	0.1395
(60/7,30/7, 0)	51.512	75.734	23.202	0.7357	189.5	0.1165
(90/7,30/7, 0)	65.734	98.631	38.218	0.7	230.15	0.0851
(0,60/7, 0)	36.819	53.891	16.057	0.7287	134.16	0.1622
(30/7,60/7, 0)	39.53	57.693	17.303	0.7303	144.35	0.1519
(60/7,60/7, 0)	49.058	71.307	22.029	0.732	179.57	0.1232
(90/7,60/7, 0)	71.869	105.49	39.319	0.7089	254.73	0.0806
(0,90/7, 0)	30.803	44.978	13.519	0.7196	110.84	0.192
(30/7,90/7, 0)	33.069	47.815	14.476	0.7212	119.26	0.181
(60/7,90/7, 0)	41.2	57.9	18.059	0.7241	149.17	0.15
(90/7,90/7, 0)	59.277	78.604	27.725	0.7124	211.16	0.1087

Table C.3: Average 16 points for the calculation of fluorescence enhancement and the modified lifetime for the configuration C.

Bibliography

- [1] M. Daniel and D. Astruc, “Gold nanoparticles: Assembly, supramolecular chemistry, quantum-size-related properties, and applications toward biology, catalysis, and nanotechnology,” *Chem. Rev.* **104**, 293–346 (2004).
- [2] S. Eustis and M. A. El-Sayed, “Why gold nanoparticles are more precious than pretty gold: Noble metal surface plasmon resonance and its enhancement of the radiative and nonradiative properties of nanocrystals of different shapes,” *Chem. Soc. Rev.* **35**, 209–217 (2006).
- [3] F. E. Wagner, S. Haslbeck, L. Stievano, S. Calogero, Q. A. Pankhurst, and K. P. Martinek, “Before striking gold in gold-ruby glass,” *Nature* **407**, 691–692 (2000).
- [4] N. Wood, *Chinese Glazes: Their Origins, Chemistry, and Recreation* (University of Pennsylvania Press, 1999).
- [5] A. Caiger-Smith, *Luster Pottery. Technique, Tradition and Innovation in Islam and the Western World* (Faber & Faber, London, UK., 1985).
- [6] <http://www.mpikg.mpg.de/886767/MetalNanoparticles.pdf>.
- [7] R. Vajtai, *Springer handbook of nanomaterials*. (Springer, Berlin, Germany., 2013).
- [8] M. Faraday, “The bakerian lecture: Experimental relations of gold (and other metals) to light,” *Philos. Trans. R. Soc. London* **147**, 145–181 (1857).
- [9] G. Mie., “Beitrage zur optik truber medien, speziell kolloidaler metallosungen.” *Ann. Phys.* **25**, 377–445 (1908).
- [10] R. Ritchie., “Plasma losses by fast electrons in thin films.” *Phys. Rev.* **106**, 874–881 (1957).
- [11] F. J. Garcia-Vidal, J. Sanchez-Dehesa, A. Dechelette, E. Bustarret, T. Lopez-Rios, T. Fournier, and B. Pannetier, “Localized surface plasmons in lamellar metallic gratings,” *J. Lightwave Technol.* **17**, 2191–2195 (1999).
- [12] A. V. Zayats and I. I. Smolyaninov, “Near-field photonics: surface plasmon polaritons and localized surface plasmons,” *J. Opt. A: Pure Appl. Opt.* **5**, S16 (2003).

Bibliography

- [13] L. J. Sherry, S.-H. Chang, G. C. Schatz, R. P. Van Duyne, B. J. Wiley, and Y. Xia, "Localized surface plasmon resonance spectroscopy of single silver nanocubes," *Nano Lett.* **5**, 2034–2038 (2005).
- [14] H. Raether., *Surface Plasmons on Smooth and Rough Surfaces and on Gratings*. (Springer, 1988).
- [15] W.L.Barnes, A.Dereux, and T. W. Ebbesen., "Surface plasmon subwavelength optics," *Nature* **391**, 667–669 (1998).
- [16] R. W. Wood, "On a remarkable case of uneven distribution of light in a diffraction grating spectrum," *Proc. Phys. Soc. London* **18**, 269 (1902).
- [17] R. W. Wood, "Anomalous diffraction gratings," *Phys. Rev.* **48**, 928–936 (1935).
- [18] A. Otto, "Excitation of nonradiative surface plasma waves in silver by the method of frustrated total reflection," *Z. Phys. A: Hadrons Nucl.* **216**, 398–410 (1968).
- [19] E. Kretschmann and H. Raether., "Radiative decay of nonradiative surface plasmon excited by light." *Z. Naturforsch.* **23A**, 2135–2136 (1957).
- [20] L. Rayleigh, "On the dynamical theory of gratings," *Proc. R. Soc. London, Ser. A* **79**, 399–416 (1907).
- [21] U. Fano, "Some theoretical considerations on anomalous diffraction gratings," *Phys. Rev.* **50**, 573–573 (1936).
- [22] R. X. Bian, R. C. Dunn, X. S. Xie, and P. T. Leung, "Single molecule emission characteristics in near-field microscopy," *Phys. Rev. Lett.* **75**, 4772–4775 (1995).
- [23] W. Zhang, H. Fischer, T. Schmid, R. Zenobi, and O. J. F. Martin, "Mode-selective surface-enhanced raman spectroscopy using nanofabricated plasmonic dipole antennas," *J. Phys. Chem. C* **113**, 14672–14675 (2009).
- [24] K. Anika, Y. Zongfu, F. Shanhui, Y. Avlasevich, M. Klaus, and W. E. Moerner., "Large single-molecule fluorescence enhancements produced by a bowtie nanoantenna," *Nat. Photonics* **3**, 654–657 (2009).
- [25] H. Eghlidi, K. G. Lee, X.-W. Chen, S. Gotzinger, and V. Sandoghdar, "Resolution and enhancement in nanoantenna-based fluorescence microscopy," *Nano Lett.* **9**, 4007–4011 (2009).
- [26] R. Bardhan, N. K. Grady, J. R. Cole, A. Joshi, and N. J. Halas, "Fluorescence enhancement by au nanostructures: Nanoshells and nanorods," *ACS Nano* **3**, 744–752 (2009).
- [27] G. P. Acuna, F. M. Moller, P. Holzmeister, S. Beater, B. Lalkens, and P. Tinnefeld, "Fluorescence enhancement at docking sites of dna-directed self-assembled nanoantennas," *Science* **338**, 506–510 (2012).

-
- [28] P. Deep, M. Mathieu, B.-M. Satish, Z. Thomas, R. Herve, H. Niek, G.-P. Maria, and W. Jerome, "A plasmonic antenna-in-box platform for enhanced single-molecule analysis at micromolar concentrations," *Nat. Nanotechnol.* **8**, 512–516 (2013).
- [29] C. D. Kinz-Thompson, M. Palma, D. K. Pulkunat, D. Chenet, J. Hone, S. J. Wind, and R. L. Gonzalez, "Robustly passivated, gold nanoaperture arrays for single-molecule fluorescence microscopy," *ACS Nano* **7**, 8158–8166 (2013).
- [30] S. Khatua, P. M. R. Paulo, H. Yuan, A. Gupta, P. Zijlstra, and M. Orrit, "Resonant plasmonic enhancement of single-molecule fluorescence by individual gold nanorods," *ACS Nano* **8**, 4440–4449 (2014).
- [31] L. Su, H. Yuan, G. Lu, S. Rocha, M. Orrit, J. Hofkens, and H. Uji-i, "Super-resolution localization and defocused fluorescence microscopy on resonantly coupled single-molecule, single-nanorod hybrids," *ACS Nano* **10**, 2455–2466 (2016).
- [32] D. J. Bergman and M. I. Stockman, "Surface plasmon amplification by stimulated emission of radiation: Quantum generation of coherent surface plasmons in nanosystems," *Phys. Rev. Lett.* **90**, 027402 (2003).
- [33] M. A. Noginov, G. Zhu, A. M. Belgrave, R. Bakker, V. M. Shalae, E. E. Narimanov, S. Stout, E. Herz, T. Suteewong, and U. Wiesner, "Demonstration of a spaser-based nanolaser," *Nature* **460**, 1110–1112 (2009).
- [34] J. Y. Suh, C. H. Kim, W. Zhou, M. D. Huntington, D. T. Co, M. R. Wasielewski, and T. W. Odom, "Plasmonic bowtie nanolaser arrays," *Nano Lett.* **12**, 5769–5774 (2012).
- [35] P. Kolchin, N. Pholchai, M. H. Mikkelsen, J. Oh, S. Ota, M. S. Islam, X. Yin, and X. Zhang, "High purcell factor due to coupling of a single emitter to a dielectric slot waveguide," *Nano Lett.* **15**, 464–468 (2015).
- [36] V. J. Sorger, N. Pholchai, E. Cubukcu, R. F. Oulton, P. Kolchin, C. Borschel, M. Gnauck, C. Ronning, and X. Zhang, "Strongly enhanced molecular fluorescence inside a nanoscale waveguide gap," *Nano Lett.* **11**, 4907–4911 (2011).
- [37] P. Viste, J. Plain, R. Jaffiol, A. Vial, P. M. Adam, and P. Royer, "Enhancement and quenching regimes in metal semiconductor hybrid optical nanosources," *ACS Nano* **4**, 759–764 (2010).
- [38] A. G. Curto, G. Volpe, T. H. Taminiau, M. P. Kreuzer, R. Quidant, and N. F. van Hulst, "Unidirectional emission of a quantum dot coupled to a nanoantenna," *Science* **329**, 930–933 (2010).
- [39] Y.-J. Lu, J. Kim, H.-Y. Chen, C. Wu, N. Dabidian, C. E. Sanders, C.-Y. Wang, M.-Y. Lu, B.-H. Li, X. Qiu, W.-H. Chang, L.-J. Chen, G. Shvets, C.-K. Shih, and S. Gwo, "Plasmonic nanolaser using epitaxially grown silver film," *Science* **337**, 450–453 (2012).

Bibliography

- [40] T. B. Hoang, G. M. Akselrod, and M. H. Mikkelsen, "Ultrafast room-temperature single photon emission from quantum dots coupled to plasmonic nanocavities," *Nano Lett.* **16**, 270–275 (2016).
- [41] J. de Torres, P. Ferrand, G. Colas des Francs, and J. Wenger, "Coupling emitters and silver nanowires to achieve long-range plasmon-mediated fluorescence energy transfer," *ACS Nano* **10**, 3968–3976 (2016).
- [42] A. Lauchner, A. E. Schlather, A. Manjavacas, Y. Cui, M. J. McClain, G. J. Stec, F. J. Garcia de Abajo, P. Nordlander, and N. J. Halas, "Molecular plasmonics," *Nano Lett.* **15**, 6208–6214 (2015).
- [43] C. Belacel, B. Habert, F. Bigourdan, F. Marquier, J.-P. Hugonin, S. Michaelis de Vasconcellos, X. Lafosse, L. Coolen, C. Schwob, C. Javaux, B. Dubertret, J.-J. Greffet, P. Senellart, and A. Maitre, "Controlling spontaneous emission with plasmonic optical patch antennas," *Nano Lett.* **13**, 1516–1521 (2013).
- [44] C. Ayala-Orozco, J. G. Liu, M. W. Knight, Y. Wang, J. K. Day, P. Nordlander, and N. J. Halas, "Fluorescence enhancement of molecules inside a gold nanomatrix," *Nano Lett.* **14**, 2926–2933 (2014).
- [45] A. Paul, Y.-R. Zhen, Y. Wang, W.-S. Chang, Y. Xia, P. Nordlander, and S. Link, "Dye-assisted gain of strongly confined surface plasmon polaritons in silver nanowires," *Nano Lett.* **14**, 3628–3633 (2014).
- [46] M. Fleischmann, P. Hendra, and A. McQuillan, "Raman spectra of pyridine adsorbed at a silver electrode," *Chem. Phys. Lett.* **26**, 163 – 166 (1974).
- [47] S. Nie and S. R. Emory, "Probing single molecules and single nanoparticles by surface-enhanced raman scattering," *Science* **275**, 1102–1106 (1997).
- [48] N. Liu, M. Hentschel, T. Weiss, A. P. Alivisatos, and H. Giessen, "Three-dimensional plasmon rulers," *Science* **332**, 1407–1410 (2011).
- [49] J. Ye, F. Wen, H. Sobhani, J. B. Lassiter, P. Van Dorpe, P. Nordlander, and N. J. Halas, "Plasmonic nanoclusters: Near field properties of the fano resonance interrogated with sers," *Nano Lett.* **12**, 1660–1667 (2012).
- [50] B. Gallinet, T. Siegfried, H. Sigg, P. Nordlander, and O. J. F. Martin, "Plasmonic radiance: Probing structure at the Ångström scale with visible light," *Nano Lett.* **13**, 497–503 (2013).
- [51] K. Thyagarajan, J. Butet, and O. J. F. Martin, "Augmenting second harmonic generation using fano resonances in plasmonic systems," *Nano Lett.* **13**, 1847–1851 (2013).
- [52] J. Butet and O. J. F. Martin, "Fano resonances in the nonlinear optical response of coupled plasmonic nanostructures," *Opt. Express* **22**, 29693–29707 (2014).

-
- [53] J. Butet and O. J. F. Martin, "Refractive index sensing with fano resonant plasmonic nanostructures: a symmetry based nonlinear approach," *Nanoscale* **6**, 15262–15270 (2014).
- [54] B. Metzger, T. Schumacher, M. Hentschel, M. Lippitz, and H. Giessen, "Third harmonic mechanism in complex plasmonic fano structures," *ACS Photonics* **1**, 471–476 (2014).
- [55] Y. Yang, W. Wang, A. Boulesbaa, I. I. Kravchenko, D. P. Briggs, A. Poretzky, D. Geohegan, and J. Valentine, "Nonlinear fano-resonant dielectric metasurfaces," *Nano Lett.* **15**, 7388–7393 (2015).
- [56] M. R. Shcherbakov, P. P. Vabishchevich, A. S. Shorokhov, K. E. Chong, D.-Y. Choi, I. Staude, A. E. Miroshnichenko, D. N. Neshev, A. A. Fedyanin, and Y. S. Kivshar, "Ultrafast all-optical switching with magnetic resonances in nonlinear dielectric nanostructures," *Nano Lett.* **15**, 6985–6990 (2015).
- [57] N. S. King, L. Liu, X. Yang, B. Cerjan, H. O. Everitt, P. Nordlander, and N. J. Halas, "Fano resonant aluminum nanoclusters for plasmonic colorimetric sensing," *ACS Nano* **9**, 10628–10636 (2015).
- [58] R. Singh, W. Cao, I. Al-Naib, L. Cong, W. Withayachumnankul, and W. Zhang, "Ultrasensitive terahertz sensing with high-q fano resonances in metasurfaces," *Appl. Phys. Lett.* **105**, 171101 (2014).
- [59] P. West, S. Ishii, G. Naik, N. Emani, V. Shalaev, and A. Boltasseva, "Searching for better plasmonic materials," *Laser Photonics Rev.* **4**, 795–808 (2010).
- [60] M. W. Knight, L. Liu, Y. Wang, L. Brown, S. Mukherjee, N. S. King, H. O. Everitt, P. Nordlander, and N. J. Halas, "Aluminum plasmonic nanoantennas," *Nano Lett.* **12**, 6000–6004 (2012).
- [61] A. N. Grigorenko, M. Polini, and K. S. Novoselov, "Graphene plasmonics," *Nat. Photonics* **6**, 749–758 (2012).
- [62] T. Low and P. Avouris, "Graphene plasmonics for terahertz to mid-infrared applications," *ACS Nano* **8**, 1086–1101 (2014).
- [63] F. J. Garcia de Abajo, "Graphene plasmonics: Challenges and opportunities," *ACS Photonics* **1**, 135–152 (2014).
- [64] S. Maier., *Plasmonics: Fundamentals and Applications* (Springer, 2007).
- [65] M. Agio and A. Alu., *Optical Antennas* (Cambridge University Press., 2013).
- [66] P. Muhlschlegel, H.-J. Eisler, O. J. F. Martin, B. Hecht, and D. W. Pohl, "Resonant optical antennas," *Science* **308**, 1607–1609 (2005).
- [67] N. Lukas and H. . Niek, "Antenna for light," *Nature* **5**, 83–90 (2011).

Bibliography

- [68] L. J. Sherry, R. Jin, C. A. Mirkin, G. C. Schatz, and R. P. Van Duyne, “Localized surface plasmon resonance spectroscopy of single silver triangular nanoprisms,” *Nano Lett.* **6**, 2060–2065 (2006).
- [69] J. N. Anker, W. P. Hall, O. Lyandres, N. C. Shah, J. Zhao, and R. P. V. Duyne., “Biosensing with plasmonic nanosensors,” *Nat. Mater.* **7**, 442–453 (1998).
- [70] B. Sepulveda, P. C. Angelome, L. M. Lechuga, and L. M. Liz-Marzan, “Lspr-based nanobiosensors,” *Nano Today* **4**, 244 – 251 (2009).
- [71] T. W. Ebbesen, H. J. Lezec, H. F. Ghaemi, T. Thio, and P. A. Wolff, “Extraordinary optical transmission through sub-wavelength hole arrays,” *Nature* **391**, 667–669 (1998).
- [72] M. J. Levene, J. Korlach, S. W. Turner, M. Foquet, H. G. Craighead, and W. W. Webb, “Zero-mode waveguides for single-molecule analysis at high concentrations,” *Science* **299**, 682–686 (2003).
- [73] H. Rigneault, J. Capoulade, J. Dintinger, J. Wenger, N. Bonod, E. Popov, T. W. Ebbesen, and P.-F. Lenne, “Enhancement of single-molecule fluorescence detection in subwavelength apertures,” *Phys. Rev. Lett.* **95**, 117401 (2005).
- [74] J. Wenger, D. Gerard, J. Dintinger, O. Mahboub, N. Bonod, E. Popov, T. W. Ebbesen, and H. Rigneault, “Emission and excitation contributions to enhanced single molecule fluorescence by gold nanometric apertures,” *Opt. Express* **16**, 3008–3020 (2008).
- [75] R. Gordon, A. Brolo, D. Sinton, and K. Kavanagh, “Resonant optical transmission through hole-arrays in metal films: physics and applications,” *Laser Photonics Rev.* **4** (2010).
- [76] F. van Beijnum, P. J. van Veldhoven, E. J. Geluk, M. J. A. de Dood, G. W. Hooft, and M. P. van Exter, “Surface plasmon lasing observed in metal hole arrays,” *Phys. Rev. Lett.* **110**, 206802 (2013).
- [77] C. Escobedo, “On-chip nanohole array based sensing: a review,” *Lab Chip* **13**, 2445–2463 (2013).
- [78] S. Kerman, C. Chen, Y. Li, W. Van Roy, L. Lagae, and P. Van Dorpe, “Raman fingerprinting of single dielectric nanoparticles in plasmonic nanopores,” *Nanoscale* **7**, 18612–18618 (2015).
- [79] A. J. Shields., “Semiconductor quantum light sources,” *Nat. Photonics* **1**, 215–233 (2007).
- [80] R. K. Kramer, N. Pholchai, V. J. Sorger, T. J. Yim, R. Oulton, and X. Zhang, “Positioning of quantum dots on metallic nanostructures,” *Nanotechnology* **21**, 145307 (2010).
- [81] A. M. Kern and O. J. F. Martin, “Surface integral formulation for 3d simulations of plasmonic and high permittivity nanostructures,” *J. Opt. Soc. Am. A* **26**, 732–740 (2009).

-
- [82] B. Gallinet and O. J. Martin, "Scattering on plasmonic nanostructures arrays modeled with a surface integral formulation," *Photonics and Nanostructures - Fundamentals and Applications* **8**, 278 – 284 (2010).
- [83] T. V. Raziman, W. R. C. Somerville, O. J. F. Martin, and E. C. L. Ru, "Accuracy of surface integral equation matrix elements in plasmonic calculations," *J. Opt. Soc. Am. B* **32**, 485–492 (2015).
- [84] T. V. Raziman and O. J. F. Martin, "Polarisation charges and scattering behaviour of realistically rounded plasmonic nanostructures," *Opt. Express* **21**, 21500–21507 (2013).
- [85] P. B. Johnson and R. W. Christy, "Optical constants of transition metals," *Phys. Rev. B* **9**, 5056–5070 (1972).
- [86] H. Fischer and O. J. F. Martin, "Engineering the optical response of plasmonic nanoantennas," *Opt. Express* **16**, 9144–9154 (2008).
- [87] B. Gallinet, A. M. Kern, and O. J. F. Martin, "Accurate and versatile modeling of electromagnetic scattering on periodic nanostructures with a surface integral approach," *J. Opt. Soc. Am. A* **27**, 2261–2271 (2010).
- [88] T. H. P. Chang, "Proximity effect in electron beam lithography," *J. Vac. Sci. Technol.* **12**, 1271–1275 (1975).
- [89] W. Chen and H. Ahmed, "Fabrication of 5-7 nm wide etched lines in silicon using 100 keV electron beam lithography and polymethylmethacrylate resist," *Appl. Phys. Lett.* **62**, 1499–1501 (1993).
- [90] C. Vieu, F. Carcenac, A. Pepin, Y. Chen, M. Mejias, A. Lebib, L. Manin-Ferlazzo, L. Couraud, and H. Launois, "Electron beam lithography: resolution limits and applications," *Appl. Surf. Sci.* **164**, 111 – 117 (2000).
- [91] K. Liu, P. Avouris, J. Bucchignano, R. Martel, S. Sun, and J. Michl, "Simple fabrication scheme for sub-10 nm electrode gaps using electron-beam lithography," *Appl. Phys. Lett.* **80**, 865–867 (2002).
- [92] J. Melngailis, "Focused ion beam technology and applications," *J. Vac. Sci. Technol., B: Microelectron. Process. Phenom.* **5**, 469–495 (1987).
- [93] S. Matsui, T. Kaito, J. ichi Fujita, M. Komuro, K. Kanda, and Y. Haruyama, "Three-dimensional nanostructure fabrication by focused-ion-beam chemical vapor deposition," *J. Vac. Sci. Technol., B: Microelectron. Nanometer Struct.–Process., Meas., Phenom.* **18**, 3181–3184 (2000).
- [94] S. Reyntjens and R. Puers, "A review of focused ion beam applications in microsystem technology," *J. Micromech. Microeng.* **11**, 287 (2001).

Bibliography

- [95] M. Altissimo, "E-beam lithography for micro-/nanofabrication," *Biomicrofluidics* **4**, 026503 (2010).
- [96] S. Y. Chou, P. R. Krauss, and P. J. Renstrom, "Nanoimprint lithography," *J. Vac. Sci. Technol., B: Microelectron. Nanometer Struct.–Process., Meas., Phenom.* **14**, 4129–4133 (1996).
- [97] M. D. Austin, W. Zhang, H. Ge, D. Wasserman, S. A. Lyon, and S. Y. Chou, "6 nm half-pitch lines and 0.04 μm 2 static random access memory patterns by nanoimprint lithography," *Nanotechnology* **16**, 1058 (2005).
- [98] M. E. Stewart, C. R. Anderton, L. B. Thompson, J. Maria, S. K. Gray, J. A. Rogers, and R. G. Nuzzo, "Nanostructured plasmonic sensors," *Chem. Rev.* **108**, 494–521 (2008).
- [99] S. Fodor, J. Read, M. Pirrung, L. Stryer, A. Lu, and D. Solas, "Light-directed, spatially addressable parallel chemical synthesis," *Science* **251**, 767–773 (1991).
- [100] M. B. Cortie and A. M. McDonagh, "Synthesis and optical properties of hybrid and alloy plasmonic nanoparticles," *Chem. Rev.* **111**, 3713–3735 (2011).
- [101] M. R. Jones, K. D. Osberg, R. J. Macfarlane, M. R. Langille, and C. A. Mirkin, "Templated techniques for the synthesis and assembly of plasmonic nanostructures," *Chem. Rev.* **111**, 3736–3827 (2011).
- [102] M. Rycenga, C. M. Cobley, J. Zeng, W. Li, C. H. Moran, Q. Zhang, D. Qin, and Y. Xia, "Controlling the synthesis and assembly of silver nanostructures for plasmonic applications," *Chem. Rev.* **111**, 3669–3712 (2011).
- [103] U. C. Fischer and H. P. Zingsheim, "Submicroscopic pattern replication with visible light," *J. Vac. Sci. Technol.* **19**, 881–885 (1981).
- [104] C. L. Haynes and R. P. Van Duyne, "Nanosphere lithography: A versatile nanofabrication tool for studies of size-dependent nanoparticle optics," *J. Phys. Chem. B* **105**, 5599–5611 (2001).
- [105] P. Hanarp, D. S. Sutherland, J. Gold, and B. Kasemo, "Control of nanoparticle film structure for colloidal lithography," *Colloids Surf., A* **214**, 23 – 36 (2003).
- [106] M. Hatzakis, "Electron resists for microcircuit and mask production," *J. Electrochem. Soc.* **116**, 1033–1037 (1969).
- [107] <http://cmi.epfl.ch> .
- [108] H. F. Yang, L. Fan, A. Z. Jin, Q. Luo, C. Z. Gu, and Z. Cui, "Low-energy electron-beam lithography of ZEP-520 positive resist," in "2006 1st IEEE International Conference on Nano/Micro Engineered and Molecular Systems," (IEEE, 2006), pp. 391–394.

-
- [109] W. Henschel, Y. M. Georgiev, and H. Kurz, "Study of a high contrast process for hydrogen silsesquioxane as a negative tone electron beam resist," *J. Vac. Sci. Technol., B: Microelectron. Nanometer Struct.–Process., Meas., Phenom.* **21**, 2018–2025 (2003).
- [110] M. Gschrey, R. Schmidt, A. Kaganskiy, S. Rodt, and S. Reitzenstein, "Study of high-resolution electron-beam resists for applications in low-temperature lithography," *J. Vac. Sci. Technol., B: Nanotechnol. Microelectron.: Mater., Process., Meas., Phenom.* **32** (2014).
- [111] J. Ingino, G. Owen, C. N. Berglund, R. Browning, and R. F. W. Pease, "Workpiece charging in electron beam lithography," *J. Vac. Sci. Technol., B: Microelectron. Nanometer Struct.–Process., Meas., Phenom.* **12**, 1367–1371 (1994).
- [112] W. Liu, J. Ingino, and R. F. Pease, "Resist charging in electron beam lithography," *J. Vac. Sci. Technol., B: Microelectron. Nanometer Struct.–Process., Meas., Phenom.* **13**, 1979–1983 (1995).
- [113] J. Zhang, M. Fouad, M. Yavuz, and B. Cui, "Charging effect reduction in electron beam lithography with na beam current," *Microelectron. Eng.* **88**, 2196–2199 (2011).
- [114] <http://www.microchem.com/products/pmma.htm> .
- [115] H.-C. Liou and J. Pretzer, "Effect of curing temperature on the mechanical properties of hydrogen silsesquioxane thin films," *Thin Solid Films* **335**, 186 – 191 (1998).
- [116] H. Namatsu, Y. Takahashi, K. Yamazaki, T. Yamaguchi, M. Nagase, and K. Kurihara, "Three-dimensional siloxane resist for the formation of nanopatterns with minimum linewidth fluctuations," *J. Vac. Sci. Technol., B: Microelectron. Nanometer Struct.–Process., Meas., Phenom.* **16**, 69–76 (1998).
- [117] A. E. Grigorescu and C. W. Hagen, "Resists for sub-20-nm electron beam lithography with a focus on hsq: state of the art," *Nanotechnology* **20**, 292001 (2009).
- [118] J.-S. Wi, T.-Y. Lee, K.-B. Jin, D. H. Hong, K. H. Shin, and K.-B. Kim, "Electron-beam lithography of co/pd multilayer with hydrogen silsesquioxane and amorphous si intermediate layer," *J. Vac. Sci. Technol., B: Microelectron. Nanometer Struct.–Process., Meas., Phenom.* **24**, 2616–2620 (2006).
- [119] N. W. Parker, A. D. Brodie, and J. H. McCoy, "High-throughput ngl electron-beam direct-write lithography system," (2000).
- [120] K. Yamazaki, K. Kurihara, T. Yamaguchi, H. Namatsu, and M. Nagase, "Novel proximity effect including pattern-dependent resist development in electron beam nanolithography," *Jpn. J. Appl. Phys.* **36**, 7552 (1997).
- [121] R. Renoud, C. Attard, J.-P. Ganachaud, S. Bartholome, and A. Dubus, "Influence on the secondary electron yield of the space charge induced in an insulating target by an electron beam," *J. Phys.: Condens. Matter* **10**, 5821 (1998).

Bibliography

- [122] V. Ivin, M. Silakov, D. Kozlov, K. Nordquist, B. Lu, and D. Resnick, "The inclusion of secondary electrons and bremsstrahlung x-rays in an electron beam resist model," *Microelectron. Eng.* **61–62**, 343 – 349 (2002).
- [123] Z. Benes, C. Deverich, C. Huang, and M. Lawliss, "Resist heating effect on e-beam mask writing at 75 kv and 60 a/cm²," (2003).
- [124] D. Sullivan, Y. Okawa, K. Sugawara, Z. Benes, and J. Kotani, "Chemical flare long-range proximity effects in photomask manufacturing with chemically amplified resists," (2006).
- [125] T. Siegfried, M. Kind, A. Terfort, O. J. F. Martin, M. Zharnikov, N. Ballav, and H. Sigg, "Reusable plasmonic substrates fabricated by interference lithography: a platform for systematic sensing studies," *J. Raman Spectrosc.* **44**, 170–175 (2013).
- [126] C. A. Goss, D. H. Charych, and M. Majda, "Application of (3-mercaptopropyl)trimethoxysilane as a molecular adhesive in the fabrication of vapor-deposited gold electrodes on glass substrates," *Anal. Chem.* **63**, 85–88 (1991).
- [127] D. P. Fromm, A. Sundaramurthy, P. J. Schuck, G. Kino, and W. E. Moerner, "Gap-dependent optical coupling of single "bowtie" nanoantennas resonant in the visible," *Nano Lett.* **4**, 957–961 (2004).
- [128] M. Abdelsalam, P. N. Bartlett, A. E. Russell, J. J. Baumberg, E. J. Calvo, N. G. Tognalli, and A. Fainstein, "Quantitative electrochemical sers of flavin at a structured silver surface," *Langmuir* **24**, 7018–7023 (2008).
- [129] B. Cui, L. Clime, K. Li, and T. Veres, "Fabrication of large area nanoprism arrays and their application for surface enhanced raman spectroscopy," *Nanotechnology* **19**, 145302 (2008).
- [130] A. K. Mahapatro, A. Scott, A. Manning, and D. B. Janes, "Gold surface with sub-nm roughness realized by evaporation on a molecular adhesion monolayer," *Appl. Phys. Lett.* **88** (2006).
- [131] X. Jiao, J. Goeckeritz, S. Blair, and M. Oldham, "Localization of near-field resonances in bowtie antennae: Influence of adhesion layers," *Plasmonics* **4**, 37–50 (2009).
- [132] S. Blair, H. Aouani, E. Devaux, T. Ebbesen, F. Mahdavi, H. Rigneault, and J. Wenger, "Influence of Adhesion Layers on the Performance of Plasmonic Antennae," in "Fourth international conference on surface plasmon photonics SPP4," (Amsterdam, Netherlands, 2009).
- [133] H. Aouani, J. Wenger, D. Gerard, H. Rigneault, E. Devaux, T. W. Ebbesen, F. Mahdavi, T. Xu, and S. Blair, "Crucial role of the adhesion layer on the plasmonic fluorescence enhancement," *ACS Nano* **3**, 2043–2048 (2009).

-
- [134] B. Abasahl, C. Santschi, and O. J. F. Martin, "Design and fabrication of plasmonic nanoantennas to control light at the nanoscale," Thesis (2014).
- [135] K. Thyagarajan, C. Santschi, P. Langlet, and O. J. F. Martin, "Highly improved fabrication of ag and al nanostructures for uv and nonlinear plasmonics," *Adv. Opt. Mater.* **4**, 871–876 (2016).
- [136] J. G. Goodberlet, J. T. Hastings, and H. I. Smith, "Performance of the raith 150 electron-beam lithography system," *J. Vac. Sci. Technol., B: Microelectron. Nanometer Struct.–Process., Meas., Phenom.* **19**, 2499–2503 (2001).
- [137] Y. Wang, C. A. Riedel, R. Chen, M. D. B. Charlton, P. Ayliffe, C. H. de Groot, M. Abb, and O. L. Muskens, "Quantification of misalignment in e-beam lithography due to height map error on optically non-uniform substrates for plasmonic nanoantennas," in "2015 IEEE 15th International Conference on Nanotechnology (IEEE-NANO)," (2015), pp. 1398–1401.
- [138] <http://apps.mnc.umn.edu/> .
- [139] S. Schietinger, M. Barth, T. Aichele, and O. Benson, "Plasmon-enhanced single photon emission from a nanoassembled metal diamond hybrid structure at room temperature," *Nano Lett.* **9**, 1694–1698 (2009).
- [140] W. Zhang, L. Huang, C. Santschi, and O. J. F. Martin, "Trapping and sensing 10 nm metal nanoparticles using plasmonic dipole antennas," *Nano Lett.* **10**, 1006–1011 (2010).
- [141] D. Punj, R. Regmi, A. Devilez, R. Plauchu, S. B. Moparthy, B. Stout, N. Bonod, H. Rigneault, and J. Wenger, "Self-assembled nanoparticle dimer antennas for plasmonic-enhanced single-molecule fluorescence detection at micromolar concentrations," *ACS Photonics* **2**, 1099–1107 (2015).
- [142] A. Portela, T.-a. Yano, C. Santschi, O. J. F. Martin, H. Tabata, and M. Hara, "Highly sensitive sers analysis of the cyclic arg–gly–asp peptide ligands of cells using nanogap antennas," *J. Biophotonics* (2016).
- [143] C. Yan, X. Wang, T. V. Raziman, and O. Martin, "Twisting fluorescence through extrinsic chiral antennas," *Nano Lett.* Under Review (2017).
- [144] C. Yan, T. V. Raziman, X. Wang, and O. Martin, "Distinguishing multipolar modes in plasmonic system," In Preparation for *ACS Photonics* (2017).
- [145] D. Valentine, B. Jeremy, and O. J. F. Martin, "Second harmonic generation with plasmonic heptamer antenna," Master Thesis EPFL (2016).
- [146] D. R. Smith, J. B. Pendry, and M. C. K. Wiltshire, "Metamaterials and negative refractive index," *Science* **305**, 788–792 (2004).

Bibliography

- [147] N. Liu, T. Weiss, M. Mesch, L. Langguth, U. Eigenthaler, M. Hirscher, C. Sonnichsen, and H. Giessen, "Planar metamaterial analogue of electromagnetically induced transparency for plasmonic sensing," *Nano Lett.* **10**, 1103–1107 (2010).
- [148] A. Boltasseva and H. A. Atwater, "Low-loss plasmonic metamaterials," *Science* **331**, 290–291 (2011).
- [149] F. Aieta, P. Genevet, M. A. Kats, N. Yu, R. Blanchard, Z. Gaburro, and F. Capasso, "Aberration-free ultrathin flat lenses and axicons at telecom wavelengths based on plasmonic metasurfaces," *Nano Lett.* **12**, 4932–4936 (2012).
- [150] X. Yin, Z. Ye, J. Rho, Y. Wang, and X. Zhang, "Photonic spin hall effect at metasurfaces," *Science* **339**, 1405–1407 (2013).
- [151] Y. Nanfang and C. . Federico, "Flat optics with designer metasurfaces," *Nat. Mater.* **13**, 139–150 (2013).
- [152] A. V. Kildishev, A. Boltasseva, and V. M. Shalaev, "Planar photonics with metasurfaces," *Science* **339** (2013).
- [153] D. Lin, P. Fan, E. Hasman, and M. L. Brongersma, "Dielectric gradient metasurface optical elements," *Science* **345**, 298–302 (2014).
- [154] Y. Zheng, J. Bian, X. Wang, J. Liu, P. Feng, H. Ge, O. J. Martin, and W. Zhang., "Revisiting newton rings with a plasmonic optical flat for high-accuracy surface inspection," *Light: Sci. Appl.* **13**, 139–150 (2016).
- [155] K.-Y. Yang, X. Wang, C. Yan, B. Jeremy, and O. Martin, "Gradient metasurface for second harmonic generation," In Preparation for *Nano Lett.* (2017).
- [156] D. Luc, C. Yan, X. Wang, T. Colomb, and O. Martin, "Direct characterization of optical metadevices with digital holographic microscopy," In Preparation for *ACS Photonics* (2017).
- [157] O. Enea, B. Zaytouni, and J. Moser, "Morphological and photoelectrochemical properties of porous, superimposed au/tio₂ layers," *J. Appl. Electrochem.* **28**, 36–40 (1998).
- [158] S. Ramadurgam, T.-G. Lin, and C. Yang, "Aluminum plasmonics for enhanced visible light absorption and high efficiency water splitting in core–multishell nanowire photoelectrodes with ultrathin hematite shells," *Nano Lett.* **14**, 4517–4522 (2014).
- [159] H. Qi, W. Chenxi, H. Hao, L. Wan, D. Deyang, H. Di, Q. Teng, and C. . Paul, K, "Aluminum plasmonic photocatalysis," *Sci. Rep.* **5**.
- [160] T. Pakizeh, M. S. Abrishamian, N. Granpayeh, A. Dmitriev, and M. Kall, "Magnetic-field enhancement in gold nanosandwiches," *Opt. Express* **14**, 8240–8246 (2006).

-
- [161] Y. Ekinici, A. Christ, M. Agio, O. J. F. Martin, H. H. Solak, and J. F. Löffler, “Electric and magnetic resonances in arrays of coupled gold nanoparticle in-tandem pairs,” *Opt. Express* **16**, 13287–13295 (2008).
- [162] Q. Li and G. P. Wang, “Tunable photonic metamaterials in the near infrared frequencies,” *Opt. Express* **18**, 14123–14128 (2010).
- [163] T. Pakizeh, “Unidirectional radiation of a magnetic dipole coupled to an ultracompact nanoantenna at visible wavelengths,” *J. Opt. Soc. Am. B* **29**, 2446–2452 (2012).
- [164] L. F. A. D. L. Tong, T. Pakizeh, “Highly directional bottom-up 3d nanoantenna for visible light,” *Sci. Rep.* **3** (2013).
- [165] G. M. Akselrod, C. Argyropoulos, T. B. Hoang, C. Ciraci, C. Fang, J. Huang, D. R. Smith, and M. H. Mikkelsen., “Probing the mechanisms of large purcell enhancement in plasmonic nanoantennas,” *Nat. Photonics* **8**, 835–840 (2014).
- [166] J. Li, D. Stein, C. McMullan, D. Branton, M. J. Aziz, and J. A. Golovchenko., “Ion-beam sculpting at nanometre length scales,” *Nature* **412**, 166–169 (2001).
- [167] N. Patterson, D. P. Adams, V. C. Hodges, M. J. Vasile, J. R. Michael, and P. G. Kotula, “Controlled fabrication of nanopores using a direct focused ion beam approach with back face particle detection,” *Nanotechnology* **19**, 235304 (2008).
- [168] R. L. Seliger, J. W. Ward, V. Wang, and R. L. Kubena, “A high-intensity scanning ion probe with submicrometer spot size,” *Appl. Phys. Lett.* **34**, 310–312 (1979).
- [169] Y. Liu and S. Blair, “Fluorescence enhancement from an array of subwavelength metal apertures,” *Opt. Lett.* **28**, 507–509 (2003).
- [170] M. Airola, Y. Liu, and S. Blair, “Second-harmonic generation from an array of sub-wavelength metal apertures,” *J. Opt. A: Pure Appl. Opt* **7**, S118 (2005).
- [171] T. Xu, X. Jiao, G. P. Zhang, and S. Blair, “Second-harmonic emission from sub-wavelength apertures: Effects of aperture symmetry and lattice arrangement,” *Opt. Express* **15**, 13894–13906 (2007).
- [172] T. Xu, X. Jiao, and S. Blair, “Third-harmonic generation from arrays of sub-wavelength metal apertures,” *Opt. Express* **17**, 23582–23588 (2009).
- [173] V. Flauraud, T. S. van Zanten, M. Mivelle, C. Manzo, M. F. Garcia Parajo, and J. Brugger, “Large-scale arrays of bowtie nanoaperture antennas for nanoscale dynamics in living cell membranes,” *Nano Lett.* **15**, 4176–4182 (2015).
- [174] W. Zhang, H. Fischer, T. Schmid, R. Zenobi, and O. J. F. Martin, “Mode-selective surface-enhanced raman spectroscopy using nanofabricated plasmonic dipole antennas,” *J. Phys. Chem. C* **113**, 14672–14675 (2009).

Bibliography

- [175] C. Sonnichsen, S. Geier, N. E. Hecker, G. von Plessen, J. Feldmann, H. Ditlbacher, B. Lamprecht, J. R. Krenn, F. R. Aussenegg, V. Z.-H. Chan, J. P. Spatz, and M. Möller, “Spectroscopy of single metallic nanoparticles using total internal reflection microscopy,” *Appl. Phys. Lett.* **77**, 2949–2951 (2000).
- [176] X. L. Wang, C. Santschi, and O. J. F. Martin., “Strong improvement of chemical and thermal stability of ag nanoantennas and films,” *Small* (2017).
- [177] V. E. Ferry, J. N. Munday, and H. A. Atwater, “Design considerations for plasmonic photovoltaics,” *Adv. Mater.* **22**, 4794–4808 (2010).
- [178] J. H. Park, P. Ambwani, M. Manno, N. C. Lindquist, P. Nagpal, S.-H. Oh, C. Leighton, and D. J. Norris, “Single-crystalline silver films for plasmonics,” *Adv. Mater.* **24**, 3988–3992 (2012).
- [179] M. R. Gartia, A. Hsiao, A. Pokhriyal, S. Seo, G. Kulsharova, B. T. Cunningham, T. C. Bond, and G. L. Liu, “Colorimetric plasmon resonance imaging using nano lycurgus cup arrays,” *Adv. Opt. Mater.* **1**, 68–76 (2013).
- [180] J. C. Reed, H. Zhu, A. Y. Zhu, C. Li, and E. Cubukcu, “Graphene-enabled silver nanoantenna sensors,” *Nano Lett.* **12**, 4090–4094 (2012).
- [181] I. J. H. McCrindle, J. Grant, T. D. Drysdale, and D. R. S. Cumming, “Multi-spectral materials: Hybridisation of optical plasmonic filters and a terahertz metamaterial absorber,” *Adv. Opt. Mater.* **2**, 149–153 (2014).
- [182] B. Y. Zheng, Y. Wang, P. Nordlander, and N. J. Halas, “Color-selective and cmos-compatible photodetection based on aluminum plasmonics,” *Adv. Mater.* **26**, 6318–6323 (2014).
- [183] Y. Wu, M. Gong, M.-C. Lin, C. Yuan, M. Angell, L. Huang, D.-Y. Wang, X. Zhang, J. Yang, B.-J. Hwang, and H. Dai, “3d graphitic foams derived from chloroaluminate anion intercalation for ultrafast aluminum-ion battery,” *Adv. Mater.* **28**, 9218–9222 (2016).
- [184] L. Zhou, C. Zhang, M. J. McClain, A. Manjavacas, C. M. Krauter, S. Tian, F. Berg, H. O. Everitt, E. A. Carter, P. Nordlander, and N. J. Halas, “Aluminum nanocrystals as a plasmonic photocatalyst for hydrogen dissociation,” *Nano Lett.* **16**, 1478–1484 (2016).
- [185] W. A. Murray and W. L. Barnes, “Plasmonic materials,” *Adv. Mater.* **19**, 3771–3782 (2007).
- [186] Y. Jin, “Engineering plasmonic gold nanostructures and metamaterials for biosensing and nanomedicine,” *Adv. Mater.* **24**, 5153–5165 (2012).
- [187] M. W. Knight, N. S. King, L. Liu, H. O. Everitt, P. Nordlander, and N. J. Halas, “Aluminum for plasmonics,” *ACS Nano* **8**, 834–840 (2014).
- [188] H. E. Bennett, R. L. Peck, D. K. Burge, and J. M. Bennett, “Formation and growth of tarnish on evaporated silver films,” *J. Appl. Phys.* **40**, 3351–3360 (1969).

-
- [189] J. M. Bennett, J. L. Stanford, and E. J. Ashley, "Optical constants of silver sulfide tarnish films," *J. Opt. Soc. Am.* **60**, 224–232 (1970).
- [190] J. L. Stanford, "Determination of surface-film thickness from shift of optically excited surface plasma resonance," *J. Opt. Soc. Am.* **60**, 49–53 (1970).
- [191] B. T. Reagor and J. D. Sinclair, "Tarnishing of silver by sulfur vapor: Film characteristics and humidity effects," *J. Electrochem. Soc.* **128**, 701–705 (1981).
- [192] J. Franey, G. Kammlott, and T. Graedel, "The corrosion of silver by atmospheric sulfurous gases," *Corros. Sci.* **25**, 133 – 143 (1985).
- [193] T. Graedel, J. Franey, G. Gualtieri, G. Kammlott, and D. Malm, "On the mechanism of silver and copper sulfidation by atmospheric H_2S and OCS ," *Corros. Sci.* **25**, 1163 – 1180 (1985).
- [194] J. L. Elechiguerra, L. Larios-Lopez, C. Liu, D. Garcia-Gutierrez, A. Camacho-Bragado, and M. J. Yacaman, "Corrosion at the nanoscale: The case of silver nanowires and nanoparticles," *Chem. Mater.* **17**, 6042–6052 (2005).
- [195] M. D. McMahon, R. Lopez, H. M. Meyer, L. C. Feldman, and R. F. Haglund, "Rapid tarnishing of silver nanoparticles in ambient laboratory air," *Appl. Phys. B* **80**, 915–921 (2005).
- [196] W. Cao and H. E. Elsayed-Ali, "Stability of Ag nanoparticles fabricated by electron beam lithography," *Mater. Lett.* **63**, 2263 – 2266 (2009).
- [197] W. M. Moore and P. J. Codella, "Oxidation of silver films by atomic oxygen," *J. Phys. Chem.* **92**, 4421–4426 (1988).
- [198] H. Qi, D. Alexson, O. Glembocki, and S. M. Prokes, "Plasmonic coupling on dielectric nanowire core–metal sheath composites," *Nanotechnology* **21**, 085705 (2010).
- [199] Y. Han, R. Lupitsky, T.-M. Chou, C. M. Stafford, H. Du, and S. Sukhishvili, "Effect of oxidation on surface-enhanced Raman scattering activity of silver nanoparticles: A quantitative correlation," *Anal. Chem.* **83**, 5873–5880 (2011).
- [200] T. W. H. Oates, M. Losurdo, S. Noda, and K. Hinrichs, "The effect of atmospheric tarnishing on the optical and structural properties of silver nanoparticles," *J. Phys. D: Appl. Phys.* **46**, 145308 (2013).
- [201] T. E. Graedel, "Corrosion mechanisms for silver exposed to the atmosphere," *J. Electrochem. Soc.* **139**, 1963–1970 (1992).
- [202] R. D. Glover, J. M. Miller, and J. E. Hutchison, "Generation of metal nanoparticles from silver and copper objects: Nanoparticle dynamics on surfaces and potential sources of nanoparticles in the environment," *ACS Nano* **5**, 8950–8957 (2011).

Bibliography

- [203] P. Smith and H. Gurev, "Silicon dioxide as a high temperature stabilizer for silver films," *Thin Solid Films* **45**, 159–168 (1977).
- [204] D. Adams and T. Alford, "Encapsulated silver for integrated circuit metallization," *Mater. Sci. Eng., R* **40**, 207–250 (2003).
- [205] M. Hillenkamp, G. D. Domenicantonio, O. Eugster, and C. Felix, "Instability of ag nanoparticles in SiO_2 at ambient conditions," *Nanotechnology* **18**, 015702 (2007).
- [206] S. Sharma and J. Spitz, "Hillock formation, hole growth and agglomeration in thin silver films," *Thin Solid Films* **65**, 339 – 350 (1980).
- [207] H. C. Kim, T. L. Alford, and D. R. Allee, "Thickness dependence on the thermal stability of silver thin films," *Appl. Phys. Lett.* **81**, 4287–4289 (2002).
- [208] T. Alford, L. Chen, and K. S. Gadre, "Stability of silver thin films on various underlying layers at elevated temperatures," *Thin Solid Films* **429**, 248 – 254 (2003).
- [209] K. Thurmer, E. D. Williams, and J. E. Reutt-Robey, "Dewetting dynamics of ultrathin silver films on $\text{Si}(111)$," *Phys. Rev. B* **68**, 155423 (2003).
- [210] C. E. Sanders, D. Verreault, G. S. Frankel, and H. C. Allen, "The role of sulfur in the atmospheric corrosion of silver," *J. Electrochem. Soc.* **162**, C630–C637 (2015).
- [211] C. H. Chou, C. L. Lin, Y. C. Chuang, H. Y. Bor, and C. Y. Liu, "High thermally stable Ni/Ag(al) alloy contacts on p-gan," *Appl. Phys. Lett.* **90**, 022103 (2007).
- [212] D. Gu, C. Zhang, Y.-K. Wu, and L. J. Guo, "Ultrasmooth and thermally stable silver-based thin films with subnanometer roughness by aluminum doping," *ACS Nano* **8**, 10343–10351 (2014).
- [213] L. VJ, N. P. Kobayashi, M. S. Islam, W. Wu, P. Chaturvedi, N. X. Fang, S. Y. Wang, and R. S. Williams, "Ultrasmooth silver thin films deposited with a germanium nucleation layer," *Nano Lett.* **9**, 178–182 (2009).
- [214] W. Chen, K. P. Chen, M. D. Thoreson, A. V. Kildishev, and V. M. Shalaev, "Ultrathin, ultrasmooth, and low-loss silver films via wetting and annealing," *Appl. Phys. Lett.* **97**, 211107 (2010).
- [215] H. Liu, B. Wang, E. S. P. Leong, P. Yang, Y. Zong, G. Si, J. Teng, and S. A. Maier, "Enhanced surface plasmon resonance on a smooth silver film with a seed growth layer," *ACS Nano* **4**, 3139–3146 (2010).
- [216] P. Nagpal, N. C. Lindquist, S.-H. Oh, and D. J. Norris, "Ultrasmooth patterned metals for plasmonics and metamaterials," *Science* **325**, 594–597 (2009).
- [217] N. C. Lindquist, T. W. Johnson, D. J. Norris, and S.-H. Oh, "Monolithic integration of continuously tunable plasmonic nanostructures," *Nano Lett.* **11**, 3526–3530 (2011).

-
- [218] N. Vogel, J. Zieleniecki, and I. Koper, "As flat as it gets: ultrasmooth surfaces from template-stripping procedures," *Nanoscale* **4**, 3820–3832 (2012).
- [219] K. M. McPeak, S. V. Jayanti, S. J. P. Kress, S. Meyer, S. Iotti, A. Rossinelli, and D. J. Norris, "Plasmonic films can easily be better: Rules and recipes," *ACS Photonics* **2**, 326–333 (2015).
- [220] A. Lovera, B. Gallinet, P. Nordlander, and O. J. Martin, "Mechanisms of fano resonances in coupled plasmonic systems," *ACS Nano* **7**, 4527–4536 (2013).
- [221] S. N. Seinfeld, John H. Pandis, *Atmospheric chemistry and physics from air pollution to climate change : problem solution manual* (Wiley, New York, 1998).
- [222] Z.-m. Xiu, Q.-b. Zhang, H. L. Puppala, V. L. Colvin, and P. J. J. Alvarez, "Negligible particle-specific antibacterial activity of silver nanoparticles," *Nano Lett.* **12**, 4271–4275 (2012).
- [223] V. J. Keast, T. A. Myles, N. Shahcheraghi, and M. B. Cortie, "Corrosion processes of triangular silver nanoparticles compared to bulk silver," *J. Nanopart. Res.* **18**, 45 (2016).
- [224] D. B. Asay and S. H. Kim, "Evolution of the adsorbed water layer structure on silicon oxide at room temperature," *J. Phys. Chem. B* **109**, 16760–16763 (2005).
- [225] J. Liu and R. H. Hurt, "Ion release kinetics and particle persistence in aqueous nano-silver colloids," *Environ. Sci. Technol.* **44**, 2169–2175 (2010).
- [226] D. R. Lide, *CRC Handbook of chemistry and physics: 2000-2001 : a ready-reference book of chemical and physical data* (2000).
- [227] C. Sanders, C. Zhang, G. Kellogg, and C. Shih, "Role of thermal processes in dewetting of epitaxial ag(111) film on si(111)," *Surf. Sci.* **630**, 168–173 (2014).
- [228] E. Prodan, C. Radloff, N. J. Halas, and P. Nordlander, "A hybridization model for the plasmon response of complex nanostructures," *Science* **302**, 419–422 (2003).
- [229] G. C. des Francs, A. Bouhelier, E. Finot, J. C. Weeber, A. Dereux, C. Girard, and E. Dujardin, "Fluorescence relaxation in the near-field of a mesoscopic metallic particle: distance dependence and role of plasmon modes," *Opt. Express* **16**, 17654–17666 (2008).
- [230] G. Baffou, C. Girard, E. Dujardin, G. Colas des Francs, and O. J. F. Martin, "Molecular quenching and relaxation in a plasmonic tunable system," *Phys. Rev. B* **77**, 121101 (2008).
- [231] J. Barthes, G. Colas des Francs, A. Bouhelier, J.-C. Weeber, and A. Dereux, "Purcell factor for a point-like dipolar emitter coupled to a two-dimensional plasmonic waveguide," *Phys. Rev. B* **84**, 073403 (2011).
- [232] S. Derom, A. Berthelot, A. Pillonnet, O. Benamara, A. M. Jurdyc, C. Girard, and G. C. des Francs, "Metal enhanced fluorescence in rare earth doped plasmonic core-shell nanoparticles," *Nanotechnology* **24**, 495704 (2013).

Bibliography

- [233] D. G. Myszka, "Kinetic analysis of macromolecular interactions using surface plasmon resonance biosensors," *Curr. Opin. Biotechnol.* **8**, 50 – 57 (1997).
- [234] J. Homola, "Present and future of surface plasmon resonance biosensors," *Anal. Bioanal. Chem.* **377**, 528–539 (2003).
- [235] K. Aslan, J. R. Lakowicz, and C. D. Geddes, "Plasmon light scattering in biology and medicine: new sensing approaches, visions and perspectives," *Curr. Opin. Chem. Biol.* **9**, 538 – 544 (2005).
- [236] O. Stranik, H. McEvoy, C. McDonagh, and B. MacCraith, "Plasmonic enhancement of fluorescence for sensor applications," *Sens. Actuators, B* **107**, 148 – 153 (2005).
- [237] J. R. Lakowicz, "Plasmonics in biology and plasmon-controlled fluorescence," *Plasmonics* **1**, 5–33 (2006).
- [238] Y. Chen, K. Munechika, and D. S. Ginger, "Dependence of fluorescence intensity on the spectral overlap between fluorophores and plasmon resonant single silver nanoparticles," *Nano Lett.* **7**, 690–696 (2007).
- [239] J. R. Lakowicz, K. Ray, M. Chowdhury, H. Szmazinski, Y. Fu, J. Zhang, and K. Nowaczyk, "Plasmon-controlled fluorescence: a new paradigm in fluorescence spectroscopy," *Analyst* **133**, 1308–1346 (2008).
- [240] A. M. Michaels, M. Nirmal, and L. E. Brus, "Surface enhanced raman spectroscopy of individual rhodamine 6g molecules on large ag nanocrystals," *J. Am. Chem. Soc.* **121**, 9932–9939 (1999).
- [241] P. L. Stiles, J. A. Dieringer, N. C. Shah, , and R. P. V. Duyne., "Surface-enhanced raman spectroscopy," *Annu. Rev. Anal. Chem.* **1**, 601–626 (2008).
- [242] E. Le Ru and P. Etchegoin. (Elsevier Press., 2008).
- [243] M. D. Sonntag, J. M. Klingsporn, A. B. Zrimsek, B. Sharma, L. K. Ruvuna, and R. P. Van Duyne, "Molecular plasmonics for nanoscale spectroscopy," *Chem. Soc. Rev.* **43**, 1230–1247 (2014).
- [244] R. Lakowicz, M. H. Chowdhury, K. Ray, J. Zhang, Y. Fu, R. Badugu, and C. D. Geddes, "Plasmon-controlled fluorescence a new detection technology," (2006).
- [245] A. K. Sarychev and G. Tartakovsky, "Magnetic plasmonic metamaterials in actively pumped host medium and plasmonic nanolaser," *Phys. Rev. B* **75**, 085436 (2007).
- [246] R. Esteban, T. V. Teperik, and J. J. Greffet, "Optical patch antennas for single photon emission using surface plasmon resonances," *Phys. Rev. Lett.* **104**, 026802 (2010).
- [247] C. Jennifer, B. J. M. Hausmann, T. M. Babinec, I. Bulu, M. Khan, P. Maletinsky, A. Yacoby, and M. Loncar, "Enhanced single-photon emission from a diamond–silver aperture," *Nature* **249**, 738–743 (2011).

-
- [248] J. Aleksander., "Efficiency of anti-stokes fluorescence in dyes," *Nature* **131**, 839–840 (1933).
- [249] P. Anger, P. Bharadwaj, and L. Novotny, "Enhancement and quenching of single-molecule fluorescence," *Phys. Rev. Lett.* **96**, 113002 (2006).
- [250] S. Kuhn, U. Haakanson, L. Rogobete, and V. Sandoghdar, "Enhancement of single-molecule fluorescence using a gold nanoparticle as an optical nanoantenna," *Phys. Rev. Lett.* **97**, 017402 (2006).
- [251] K. VISSCHER, G. J. BRAKENHOFF, and T. D. VISSER, "Fluorescence saturation in confocal microscopy," *J. Microsc.* **175**, 162–165 (1994).
- [252] A. M. Kern, A. J. Meixner, and O. J. F. Martin, "Molecule-dependent plasmonic enhancement of fluorescence and raman scattering near realistic nanostructures," *ACS Nano* **6**, 9828–9836 (2012).
- [253] J. R. Lakowicz, "Radiative decay engineering: Biophysical and biomedical applications," *Anal. Biochem.* **298**, 1 – 24 (2001).
- [254] P. A. M. Dirac, "The quantum theory of the emission and absorption of radiation," *Proc. R. Soc. London, Ser. A* **114**, 243–265 (1927).
- [255] G. S. Agarwal, "Vacuum field rabi splittings in microwave absorption by rydberg atoms in a cavity," *Phys. Rev. Lett.* **53**, 1732–1734 (1984).
- [256] <https://www.atto-tec.com> .
- [257] S. Sumit, C. Raghvendra, Pratap, S. Abhay, A. Saurabh, and S. . Shobha, "Plasmonic micro lens for extraordinary transmission of broadband light," *Sci. Rep.* **10**, 05586 (2013).
- [258] J. Enderlein and T. Ruckstuhl, "The efficiency of surface-plasmon coupled emission for sensitive fluorescence detection," *Opt. Express* **13**, 8855–8865 (2005).
- [259] H. Shen, G. Lu, Y. He, Y. Cheng, and Q. Gong, "Unidirectional enhanced spontaneous emission with metallo-dielectric optical antenna," *Opt. Commun.* (2015).
- [260] D. K. Gramotnev and S. I. Bozhevolnyi., "Plasmonics beyond the diffraction limit," *Nature* **4**, 83–91 (2010).
- [261] E. M. Purcell, H. C. Torrey, and R. V. Pound, "Resonance absorption by nuclear magnetic moments in a solid," *Phys. Rev.* **69**, 37–38 (1946).
- [262] K. Drexhage, "Influence of a dielectric interface on fluorescence decay time," *J. Lumin.* **1**, 693 – 701 (1970).
- [263] W. L. Barnes, "Fluorescence near interfaces: The role of photonic mode density," *J. Mod. Opt.* **45**, 661–699 (1998).

Bibliography

- [264] C. D. Geddes and J. R. Lakowicz, "Editorial: Metal-enhanced fluorescence," *J. Fluoresc.* **12**, 121–129 (2002).
- [265] J. R. Lakowicz, Y. Shen, S. D'Auria, J. Malicka, J. Fang, Z. Gryczynski, and I. Gryczynski, "Radiative decay engineering," *Anal. Biochem.* **301**, 261 – 277 (2002).
- [266] K. Aslan, I. Gryczynski, J. Malicka, E. Matveeva, J. R. Lakowicz, and C. D. Geddes, "Metal-enhanced fluorescence: an emerging tool in biotechnology," *Curr. Opin. Biotechnol.* **16**, 55 – 62 (2005). Analytical biotechnology.
- [267] J. R. Lakowicz, "Radiative decay engineering 5: metal-enhanced fluorescence and plasmon emission," *Anal. Biochem.* **337**, 171 – 194 (2005).
- [268] F. Mahdavi and S. Blair, "Nanoaperture fluorescence enhancement in the ultraviolet," *Plasmonics* **5**, 169–174 (2010).
- [269] E. Dulkeith, A. C. Morteani, T. Niedereichholz, T. A. Klar, J. Feldmann, S. A. Levi, F. C. J. M. van Veggel, D. N. Reinhoudt, M. Moller, and D. I. Gittins, "Fluorescence quenching of dye molecules near gold nanoparticles: Radiative and nonradiative effects," *Phys. Rev. Lett.* **89**, 203002 (2002).
- [270] H. Mertens, A. F. Koenderink, and A. Polman, "Plasmon-enhanced luminescence near noble-metal nanospheres: Comparison of exact theory and an improved gersten and nitzan model," *Phys. Rev. B* **76**, 115123 (2007).
- [271] O. L. Muskens, V. Giannini, J. A. Sánchez-Gil, and J. G. Rivas, "Optical scattering resonances of single and coupled dimer plasmonic nanoantennas," *Opt. Express* **15**, 17736–17746 (2007).
- [272] L. Rogobete, F. Kaminski, M. Agio, and V. Sandoghdar, "Design of plasmonic nanoantennae for enhancing spontaneous emission," *Opt. Lett.* **32**, 1623–1625 (2007).
- [273] J. Wolters, G. Kewes, A. W. Schell, N. Nüsse, M. Schoengen, B. Löchel, T. Hanke, R. Bratschitsch, A. Leitenstorfer, T. Aichele, and O. Benson, "Coupling of single nitrogen-vacancy defect centers in diamond nanocrystals to optical antennas and photonic crystal cavities," *Phys. Status Solidi B* **249**, 918–924 (2012).
- [274] S. Derom, R. Vincent, A. Bouhelier, and G. C. des Francs, "Resonance quality, radiative/ohmic losses and modal volume of mie plasmons," *EPL* **98**, 47008 (2012).
- [275] B. Peng, Q. Zhang, X. Liu, Y. Ji, H. V. Demir, C. H. A. Huan, T. C. Sum, and Q. Xiong, "Fluorophore doped core multishell spherical plasmonic nanocavities: Resonant energy transfer toward a loss compensation," *ACS Nano* **6**, 6250–6259 (2012).
- [276] R. Carminati, J.-J. Greffet, C. Henkel, and J. Vigoureux, "Radiative and non-radiative decay of a single molecule close to a metallic nanoparticle," *Opt. Commun.* **261**, 368 – 375 (2006).

-
- [277] R. Faggiani, J. Yang, and P. Lalanne, “Quenching, plasmonic, and radiative decays in nanogap emitting devices,” *ACS Photonics* **2**, 1739–1744 (2015).
- [278] A. Puchkova, C. Vietz, E. Pibiri, B. Wunsch, M. Sanz Paz, G. P. Acuna, and P. Tinnefeld, “Dna origami nanoantennas with over 5000-fold fluorescence enhancement and single molecule detection at 25 μm ,” *Nano Lett.* **15**, 8354–8359 (2015).
- [279] H. Yuan, S. Khatua, P. Zijlstra, M. Yorulmaz, and M. Orrit, “Thousand-fold enhancement of single-molecule fluorescence near a single gold nanorod,” *Angew. Chem., Int. Ed.* **52**, 1217–1221 (2013).
- [280] T. Schumacher, M. Brandstetter, D. Wolf, K. Kratzer, M. Hentschel, H. Giessen, and M. Lippitz, “The optimal antenna for nonlinear spectroscopy of weakly and strongly scattering nanoobjects,” *Appl. Phys. B* **122**, 91 (2016).
- [281] J. A. Fan, C. Wu, K. Bao, J. Bao, R. Bardhan, N. J. Halas, V. N. Manoharan, P. Nordlander, G. Shvets, and F. Capasso, “Self assembled plasmonic nanoparticle clusters,” *Science* **328**, 1135–1138 (2010).
- [282] A. E. Miroshnichenko, S. Flach, and Y. S. Kivshar, “Fano resonances in nanoscale structures,” *Rev. Mod. Phys.* **82**, 2257–2298 (2010).
- [283] J. D. Jackson, *Classical Electrodynamics* (Wiley, 1998).

Xiaolong WANG

Date of birth: May 8, 1983 (Anhui), Single

Nationality: Chinese

Address: Ch. des Vignes-D'Argent 1 Lausanne, 1004 Switzerland

Phone: +41 21 69 31192, +41 787079789

Skype: wangrains

Email: xiaolong.wang@epfl.ch

Linkedin: <https://ch.linkedin.com/in/xiaolongwangb8b8347a>



EDUCATION:

- **2013 – Present:** École Polytechnique Fédérale de Lausanne (EPFL), Nanophotonics and Metrology Laboratory (NAM), **Ph.D** Nanophotonics, Lausanne, Switzerland.
- **2010 –2013:** Friedrich-Schiller-University Jena, **M.Sc.**, Optics and Photonics Jena, Germany **GPA: 1.9 (of 5)**
- **2009 –2010:** Institute d'Optique Graduate School Paris, **M.Sc.**, Photonics, Paris, France **GPA: 14 (of 20)**
- **2007 –2009:** South China University of Technology, **M.Sc., Materials**, Guangzhou, China **GPA: 3.4 (of 4)**
- **2003 –2007:** Anhui University, **B.Sc.**, Optical Communication, Anhui, China **GPA: 3.6 (of 4)**

HONORS & AWARDS:

- **2010-2012:** Scholarship, Abbe School of Photonics, Friedrich-Schiller-University Jena.
- **2007-2009:** The first-place scholarship, two times, South China University of Technology.
- **2003-2007:** The second-place scholarship, six times, Anhui University.

LIST OF PUBLICATIONS:

Published

1. Yun Zheng, Juxiu Liu, **Xiaolong Wang**, Peng Feng, Jie Bian, Haixiong Ge, Olivier J. F. Martin & Weihua Zhang, Revisiting Newton's Ring with Metasurfaces for High Accuracy Surface Inspection, Light Science & Application doi: 10.1038/lsa.2016.156.

Under review

2. **X. L. Wang**, C. Santschi, O. J. F. Martin, Strong Improvement of Chemical and Thermal Stability of Ag Nanoantennas and Films, submitted for *Small*.
3. C. Yan, **X. L. Wang**, T. V. Raziman, O. J. F. Martin, Maximizing the Extrinsic Chirality for Circular-Polarized Emission from Molecules, submitted for *Nano Letters*.
4. H. Wang, **X. L. Wang**, C. Yan, H. Zhao, J. Zhang, C. Santschi, O. J. F. Martin, Full Color Generation Using Silver Tandem Nanodisks, submitted for *ACS NANO*.

In preparation

5. **X. L. Wang**, C. Yan, T. V. Raziman, S. Dutta-Gupta, B. Abasahl, C. Santschi, O. J. F. Martin, Engineering Fluorescence with Highly Tunable Fano Resonant Plasmonic Systems, in preparation for *Nano Letters*.
6. C. Yan, T. V. Raziman, **X. L. Wang**, O. J. F. Martin, Distinguishing Multipolar Modes in Plasmonic System, in preparation for *ACS Photonics*.
7. K. Y. Yang, J. Butet, **X. L. Wang**, C. Yan, O. J. F. Martin, Gradient Metasurface for Second Harmonic Generation, in preparation for *ACS NANO*.
8. L. Driencout, C. Yan, **X. L. Wang**, T. Colomb, O. J. F. Martin, Direct Characterization of Optical Metadevices with Digital Holographic Microscopy, in preparation for *Light Science & Application*.

ORAL PRESENTATIONS:

1. **Xiaolong Wang** and Olivier J. F. Martin, Engineering Fluorescence Lifetime with Fano-like Plasmonic system, *SPIE*, San Francisco, America, February 1-6 2014.
2. **Xiaolong Wang** and Olivier J. F. Martin, Engineering Fluorescence Lifetime with Fano-like Plasmonic system, *SPIE*, San Diego, America, August 9-13 2015.
3. **Xiaolong Wang**, C. Santschi, and Olivier J. F. Martin, Strong Improvement of Long-term Chemical and Thermal Stability of Ag Nanoantennas and Films, *Nanometa 2017*, Seefeld in Tirol, Austria, January 4-7 2017.

POSTER PRESENTATIONS:

1. **Xiaolong Wang** and Olivier J. F. Martin, Advanced Fano-resonant Plasmonic Nanostructures for Fluorescence Enhancement, 20th International Workshop on “Single Molecule Spectroscopy and Ultrasensitive Analysis in the Life Sciences” September 2-5, 2014 in Berlin, Germany.
2. **Xiaolong Wang** and Olivier J. F. Martin, Directional emission of fluorescence via strongly coupled multi-resonant antennas, *GRC Plasmonics*, Newry, USA, July 6-11 2014.
3. **Xiaolong Wang**, C. Santschi, and Olivier J. F. Martin, Strong Improvement of Chemical and Thermal Stability of Ag Nanoantennas and Films, *GRC Plasmonics*, Newry, USA, July 9-15 2016.
4. C. Yan, **Xiaolong Wang**, and Olivier J. F. Martin, T-shape Antenna for Planar Plasmonic Chiral Response, *GRC Plasmonics*, Newry, USA, July 9-15 2016.

LANGUAGE:

English: Spoken and written **German:** Spoken **French:** Limited **Chinese:** Native

EXTRACURRICULAR ACTIVITIES:

- Basketball, Football, History,